Spectroscopic and Lasing Characterization of Electroluminescent Organic Materials

Dissertation
Zur Erlangung des Doktorgrades
der Naturwissenschaften
(Dr. rer. nat.)

der Naturwissenschaftlichen Fakultät II - Physik
der Universität Regensburg

vorgelegt von

Ashu Kumar Bansal

aus Gangoh, India

Regensburg 2008

Promotionsgesuch eingereicht am: 15.01.2008
Tag der mündlichen Prüfung: 14.03.2008

Diese Arbeit wurde angeleitet von: Prof. Dr. Alfons Penzkofer

Prüfungsausschuss:
Vorsitzender: Prof. Dr. Matthias Brack
1. Gutachter: Prof. Dr. Alfons Penzkofer
2. Gutachter: Prof. Dr. Christian Schüller
weiterer Prüfer: Prof. Dr. Josef Jweck

Contents

1. Introduction

The electronic and optical properties of electroluminescent organic materials have attracted tremendous academic and industrial research interests over the past decades due to the appealing advantages that these materials offer for electronic devices such as organic light emitting diodes (OLEDs) [Tan87], organic field effect transistors (OFETs) [Bur88], organic solar cells (OSCs) [Hal95], photodiodes [Yu98] and organic lasers [Mal05]. The devices using organic materials are attractive because they can take advantage of organic materials such as potentially low cost, capability of thin-film, large-area and flexible device fabrication. These devices can be processed by a multitude of different methods, the most important of which are vapor deposition and solution-based processes, such as spin-coating and different printing techniques [Kaf05]. The deposition of thin films can be carried out at room temperature, and the production costs are considerably lower than those of corresponding inorganic optoelectronic devices. Organic photo-conducting materials have already established wide markets in copying machines and laser printers. OLEDs have found practical applications in small displays such as mobile phones, digital cameras, and car audios. They are expected to expand their markets to flat panel television and room lighting in the near future [Kaf05].

Despite the huge advance in the development of organic photonic and electronic devices, one important device is still missing in the market, the electrically pumped organic laser diode. Since the first demonstration in 1996 of photo-pumped lasing from semiconducting polymers [Tes96], much effort has been devoted to the development of organic diode lasers [McG00, Tes99]. However, because of the presence of strong charge-induced absorption and electrode induced absorption, efforts to make electrically pumped diode lasers from organic and polymeric films have not been successful. Semiconductor diode laser pumped organic thin film lasers have been

realized recently [Dua05, Dua08]. The search for new lasing materials which are soluble in organic solvents and can be prepared in the form of thin films is of great interest.

Motivated by the rapid growth of organic industry, the development of laser diodes has become the focus of many investigations. To avoid complications that are associated with current injection, charge transport and electrode incorporation, it is always beneficial to study stimulated emission and gain, starting with excitation by optical pumping. As a matter of fact, stimulated emission was first observed in a polymer solution [Mos92], and later also in diluted or undiluted solid films [Yan95]. The first attempt to achieve lasing action from a high gain organic semiconductor material was carried out using a microcavity resonator [Tes96]. Since then a large number of research groups are involved in the spectroscopic characterization and determination of laser action in luminescent organic molecules. Laser action (including wave-guided travelling-wave laser action) was achieved for various poly-phenylenevinylenes (PPV) [Hid97], poly-phenylene-ethynylenes (PPE) [Hol97], poly-para-phenylenes (PPP) [Lem00], poly-arylene-vinylenes (PAV) [Hol01], triphenylamine (TPA) based polymers [Pen01], and triphenylamine dimer (TPD) based conjugated and non conjugated polymers [Hol02, Phi03].

Generally no laser action is achieved for neat films of organic laser dyes since molecular aggregation occurs and the fluorescence efficiency is strongly reduced by self quenching [Pen86]. Several spiro-dyes have high solid-state fluorescence efficiency and show optically pumped neat thin-film amplified spontaneous emission [Sal02]. The widely used electroluminescent triphenylamine dimer TPD molecules turned out to work as efficient violet-wavelength thin-film lasers [Hol00, Phi03]. Neat-film laser action was also achieved with a thianthrene-substituted distyrylbenzene dye (thianthrene-DSB) [Hol04]. Single-mode tunable laser emission was

achieved with an electroluminescent oligothiophene (quinquethiophene-S,S-dioxide T5oA) [Zav01].

1.1 Motivation and outline

The primary objective of the work presented in this dissertation is the photo-physical and lasing characterization of some low molar mass electroluminescent organic materials and a newly synthesized luminescent polymer. The studied low molar mass organic dye molecules consist of one, two or three identical units. They are extensively used as hole transport materials in organic light emitting devices [Kaf05]. They have well defined glass transition temperatures and readily form uniform amorphous thin films. The studied polymer was synthesised for electroluminescent purposes [Fra01] but has not been characterized for its laser performance before this work.

Not all luminescent organic molecules are laser active [Hol01a, Hol01b]. They may be applicable to light emitting devices but may not be able to be used as lasing materials. Generally laser active organic dyes loose their laser active properties when they are used as neat thin films, due to fluorescence self-quenching [Dua90]. The electroluminescent molecules applied in organic light emitting diodes (OLEDs) retain their good luminescence properties in neat films. We will determine the laser ability of the investigated molecules in diluted solution and in neat films. The investigated molecules are characterized by optical and spectroscopic methods and then their lasing behaviour is studied.

Liquid solutions of the electroluminescent materials in dye-laser cell will be operated in transverse pumped low-Q lasing for effective stimulated cross-section determination. Wave-guided travelling wave lasing (amplification of spontaneous emission, mirror-less lasing, laser generator operation) is used to find out whether a specific thin-film sample is laser active or not.

One-dimensional DFB laser studies are carried out to get narrow-band, frequency tuneable, small divergent organic lasers which may find application in integrated optics and telecommunication.

Chapter 2 consists of a brief description of fundamental properties of organic materials. In section 2.1, delocalization of π electrons in organic molecules will be discussed. Section 2.2 provides the optical and electronic properties of organic materials. In section 2.3 some fundamentals of nonlinear spectroscopic properties of organic materials like saturable absorption and inverse saturable absorption are given. The criteria that should be fulfilled by organic materials to show laser action are given in section 2.4.

The chapter 3 covers the experimental techniques that have been used in this work. The structural formulae of the investigated organic materials used in this thesis are given in the section 3.1. The preparation of films on substrates for optical and spectroscopic characterization and laser action are explained in section 3.2. The determination of optical constants (refractive index and absorption coefficient) and the thickness of thin films by spectrally resolved reflectance and transmittance measurements are described in section 3.3.

In section 3.4 absorption cross-section spectra of organic solutions of known concentration and of thin films are calculated from transmission measurement results.

Details about the fluorescence quantum distribution measurements are given in section 3.5. The fluorescence quantum yields are determined by comparing with the emission spectrum of a reference dye of known quantum yield. The degree of fluorescence polarization is determined by orientation dependent fluorescence measurements.

In section 3.6 a detailed description of fluorescence lifetime measurements is given. The samples are excited with single picosecond laser pulses of a mode-locked ruby laser system (pulse duration 35ps, wavelength 347.15nm) or a mode-locked Titanium Sapphire laser system

(pulse duration 3ps, wavelength 400nm). For fluorescence lifetimes longer than 300 ps a micro-channel-plate detector system is used for recording. For lifetimes less than 300 to 500 ps, a single-sweep streak camera is used for detection.

The excited state absorption behavior of the investigated organic materials is studied by the intensity dependent transmission measurements in section 3.7.

Section 3.8 describes low-Q laser measurements. A transverse pumped uncoated rectangular dye laser cell is used as laser resonator. The spectral laser output as a function of the pump laser energy density is analysed to extract the excited state absorption of the studied organic materials in the fluorescence spectral region.

The wave guided traveling wave lasing arrangement of neat thin films is described in section 3.9. The samples are excited with picosecond laser pulses. The laser action is realized by spectral narrowing and a sharp increase of the emission signal above a certain threshold.

The distributed feedback laser experiment is explained in section 3.10. The organic materials are spin coated on substrates with corrugated gratings. The surface laser emission from the gratings is detected and analysed.

The results of optical, spectroscopic and lasing action measurements of all studied electroluminescent organic molecules are represented and discussed in chapter 4. The chapter is divided in to four sections. In sections 4.1 to 4.3, the results of the low molar mass electroluminescent molecules are discussed. Section 4.4 gives the results of the studied polymer [Fra01].

Chapter 5 summarizes the thesis with a discussion of the results obtained and provides direction for further research.

2. Fundamental principles

2.1 Organic materials with conjugated π-electron system

The absorption of organic materials in the visible region is based on the presence of delocalized π- electrons in unsaturated hydrocarbon molecules. One of the most prominent representatives of this class is the benzene ring depicted in Fig. 2.1. Each carbon atom provides four valence electrons, three of which form σ-bonds with neighbouring carbon or hydrogen atoms. The remaining 6 valence electrons of the 6 carbon atoms occupy p_z orbitals, which are aligned perpendicular to the plane of the σ-bonds. The p_z electrons from two neighbouring

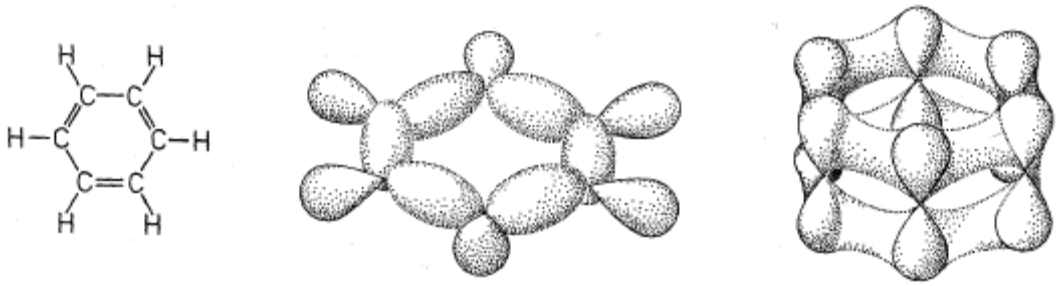

(a) (b) (c)

Fig. 2.1: C_6H_6 (benzene): (a) chemical structure formula, (b) spatial distribution of the σ-orbitals which are responsible for the steric configuration, (c) spatial distribution of the π-orbitals forming a delocalized π-system [Hak04].

carbons form a π-bond. In this 'conjugated' π system, π-electrons can no longer be attributed to one specific C-C bond; instead, their wavefunction is delocalized over the entire conjugated ring.

Every electroluminescent organic material contains a more or less extended π-electron system. These delocalized π-electrons are responsible for the absorption behaviour and the semiconducting properties. Fig. 2.2 shows the chemical structure of two common electroluminescent materials. The hole transport material 3-methyl TPD (N,N'-di-phenyl-bis-(3-methylphenyl)-biphenyl-4,4'-diamine) is a single molecule with extension of the conjugated system over the molecule. The conjugated polymer PPV (poly(para-phenylene-vinylene)) consist

of many identical, conjugated repeat units. The π-electrons may be delocalized over several repeat units.

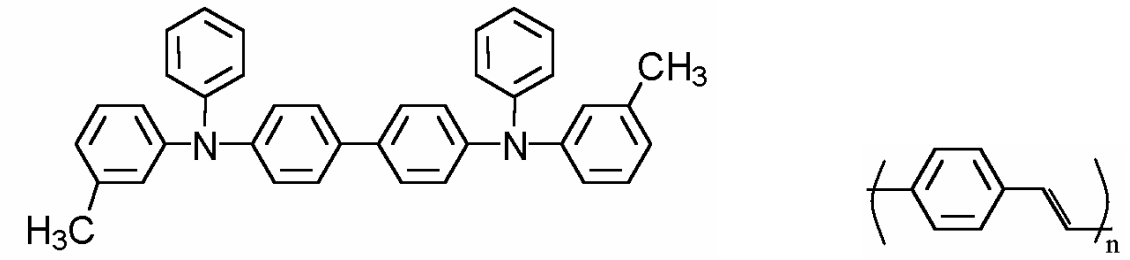

(a) (b)

Fig. 2.2: Chemical structure formulae of organic materials (a) hole transport material 3-methyl TPD [Hol00], (b) poly (p-phenylenevinylene) (PPV) [Lem00] .

2.2 Electronic transitions in organic materials

Whenever an electronic transition occurs in a molecule the nuclei are subjected to a change in Coulombic force as a result of the redistribution of electronic charge that accompanies the transition. As a consequence, electronic transitions are strongly coupled to the vibrational modes

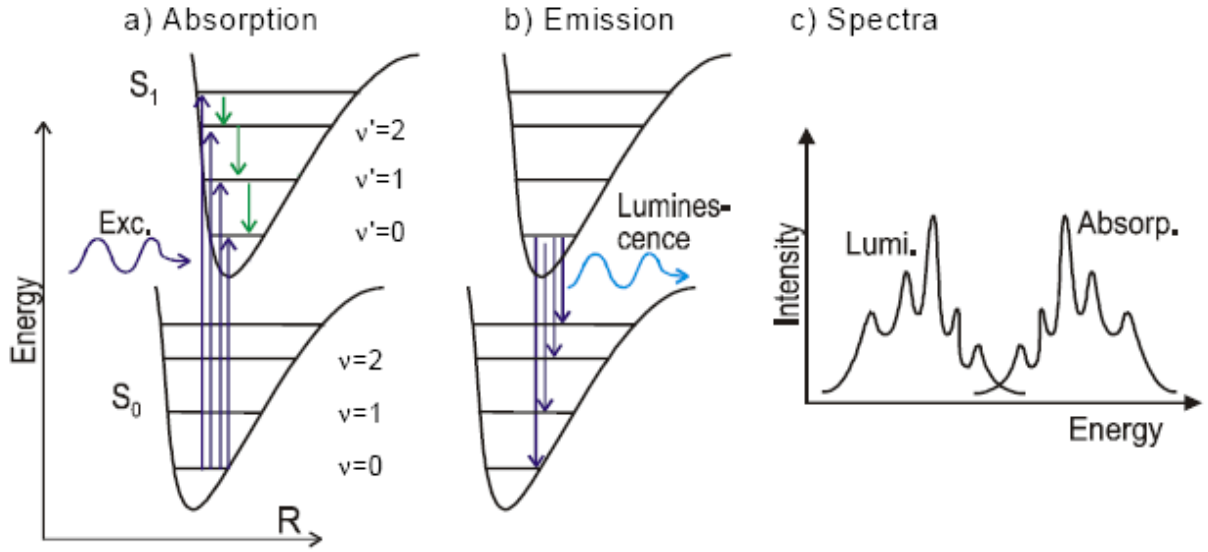

Fig. 2.3: Molecular potential energy as a function of the atomic distance. Vibronic eigenstates are denoted by ν and ν'. The arrows indicate vibronic transitions associated with (a) absorption and (b) emission of a photon. The corresponding absorption and luminescence spectra are shown in (c) [HAK04].

of the molecule. In the absorption (fluorescence) spectrum these vibronic transitions cause characteristic side-bands above (below) the purely electronic transition. Fig. 2.3 (a) sketches the molecular potential energy as a function of a generalized nuclear coordinate R for the ground state S_0 and the electronically excited singlet state S_1. The respective vibronic states are denoted by ν and ν'. Since the energy associated with a vibronic excitation is usually much higher than the thermal energy at room temperature, a molecule in thermal equilibrium occupies dominantly the state S_0, ν=0. Absorption of a photon of suitable energy causes a transition $S_0,\nu \rightarrow S_n,\nu'$. It is followed by radiative and radiationless transitions (radiative transitions are included in Fig. 2.3 (b)). The most important transitions are summarized in Fig. 2.4. Following an excitation into a vibronically excited state S_1 a molecule quickly relaxes to the vibronic ground-state ν'=0 by internal conversion. In a radiative transition the molecule returns to S_0,ν accompanied by spontaneous emission (fluorescence) of a photon.

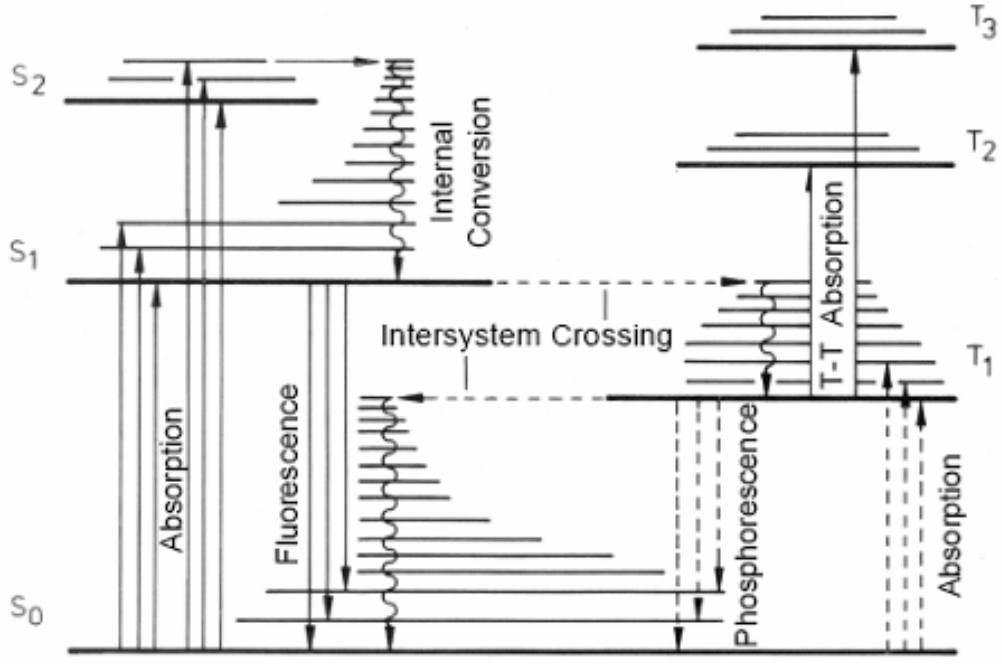

Fig. 2.4: Jablonski diagram of a molecule with singlet and triplet levels. Every electronic state is drawn with a number of associated vibronic states. Internal conversion and intersystem crossing are radiationless transitions.

The resulting absorption and fluorescence spectra are sketched in Fig. 2.3 (c). In liquid and solid-state often the vibronic structure can not be resolved due to inhomogeneous broadening of the transitions and the overlay of many vibrational modes. The Stokes-shift between the absorption and emission maxima of the purely electronic transition is caused by intra-molecular structural relaxation and intermolecular energetic dissipation as well as solute-solvent reorganization (solvent effect) [Val02].

2.3 Nonlinear spectroscopic properties

2.3.1 Saturable absorption

The bleaching of absorbing media by intense light is a general phenomenon [Her67]. It means that at high intensities the transmission behaviour of organic molecules differs from the small signal transmission. To explain the intensity dependent transmission behaviour of organic materials a three level model may be adopted as shown in Fig. 2.5.

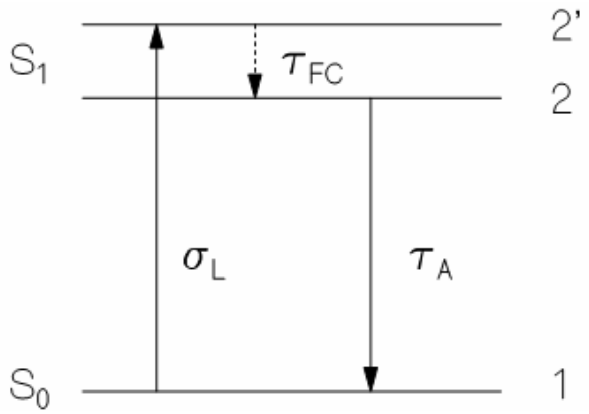

Fig. 2.5: Three-level system for understanding the behaviour of saturable absorption in the case of first excited singlet state excitation. S_0, singlet ground state; S_1, first excited singlet state with Franck-Condon level 2' and thermally relaxed level 2; σ_L absorption cross section; τ_{FC}, Franck-Condon relaxation time; τ_A, ground state absorption recovery time.

A transition from S_0 - S_1 ($1 \rightarrow 2'$) excites the molecules from ground state to a higher lying state in the S_1 band. If the Franck-Condon relaxation time τ_{FC} within the S_1 band is short in

comparison to the fluorescence lifetime, the excited molecules will relax quickly to the thermally relaxed level 2 of S_1- state during the excited-state lifetime. At high excitation intensities all molecules will accumulate in level 2. In this way the number of molecules in the ground state decreases and the transmission increases correspondingly.

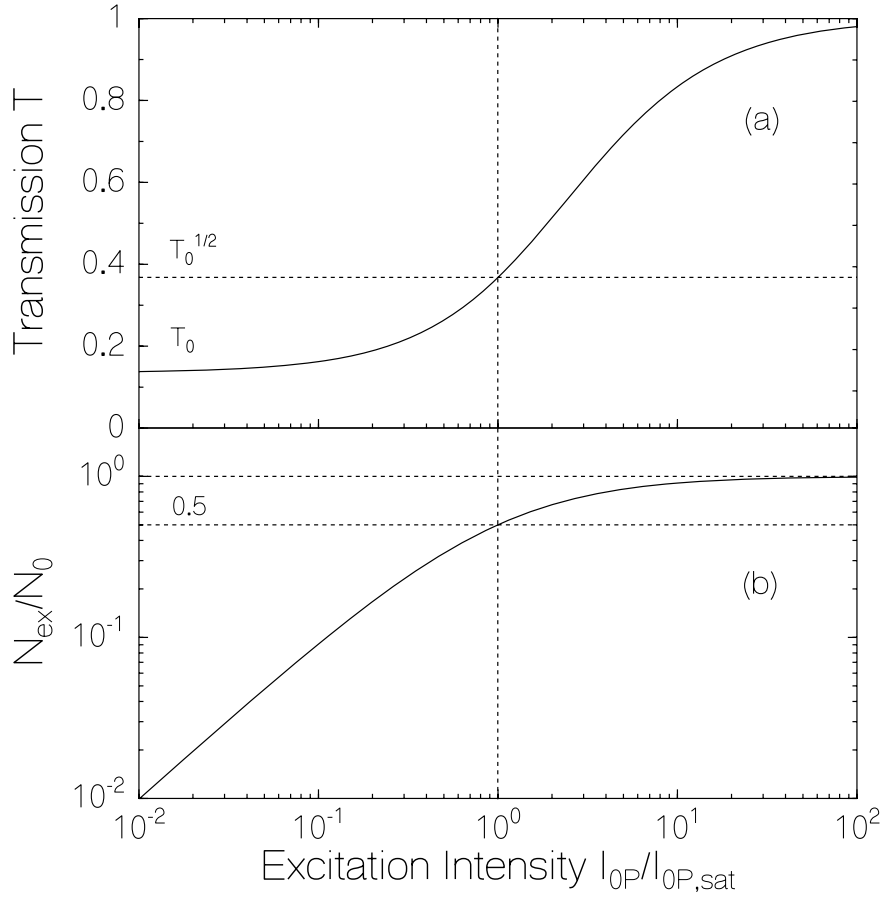

Fig. 2.6: (a) Intensity-dependent transmission behaviour of saturable absorber. (b) Intensity dependent population accumulation in S_1-state. N_{ex}, the number of molecules in S_1-state. N_0, the total number of molecules. $I_{0P,sat}$, saturation intensity. T_0, small signal transmission.

The accumulation of the molecules in the S_1-level and correspondingly the increase in transmission is shown above in Fig. 2.6. According to the 3-level model used, the transmission at higher intensities approaches T = 1, because there is no further excited levels assumed to be present in the applied 3-level model.

The intensity at which half of the total molecules are excited to the higher state i.e. (N_{ex}/N_0 = 0.5), is called saturation intensity, I_{sat}. Accordingly the transmittance rises to $T_{sat} = \sqrt{T_0}$.

For a fast saturable absorber (the excitation pulse duration Δt_P is longer than the relaxation time τ_A and τ_A is longer then τ_{FC}), the saturation intensity is given by [Her67]

$$I_{sat,f} = \frac{h\nu_P}{\sigma_P \tau_A} \tag{2.1}$$

where τ_A is the absorption recovery time (it is equal to fluorescence lifetime τ_F), h is the Planck's constant, ν_P is the excitation frequency, and σ_P is the absorption cross section.

For a slow saturable absorber the excitation pulse duration Δt_P is shorter than the relaxation time τ_A. In this case the saturation intensity is given by [Pen88]

. $$I_{sat,s} = \frac{h\nu_p}{\sigma_P \Delta t_P} \tag{2.2}$$

2.3.2 Reverse saturable absorption

Reverse saturable absorption was first observed by [Giu67]. It was noticed that under intense laser pulse irradiation, some organic dyes did not show bleaching as expected, but became darker at high excitation intensities. This situation occurs if the excited state absorption cross-section for absorption from the S_1-level to higher levels S_n is stronger than the ground state absorption. In this case, the transmission decreases with increasing excitation intensity. To understand this phenomenon, we consider that there exist further higher energy states with sufficient excited-state absorption cross-section. So we consider a multi level diagram as shown in Fig. 2.7. The pump laser excites the chromophore from the S_0 ground-state to a Franck-Condon level 2' in the S_1 band. From there the molecules relax to a thermalized level 2 with the Franck-Condon relaxation

time constant, τ_{FC}. From the S_1 band excited-state absorption, $\sigma_{ex,P}$, excites the molecules to a higher lying singlet band S_n (level 3). The higher excited molecules relax quickly back to the first excited singlet state with a time constant τ_{ex}. The S_1 state back relaxation to the ground-state is taken into account by the ground-state absorption recovery time, τ_A. If $\sigma_{ex,P}$ is greater than σ_P, then the transmission will decrease with rising excitation intensity. This is the case for reverse saturable absorbers.

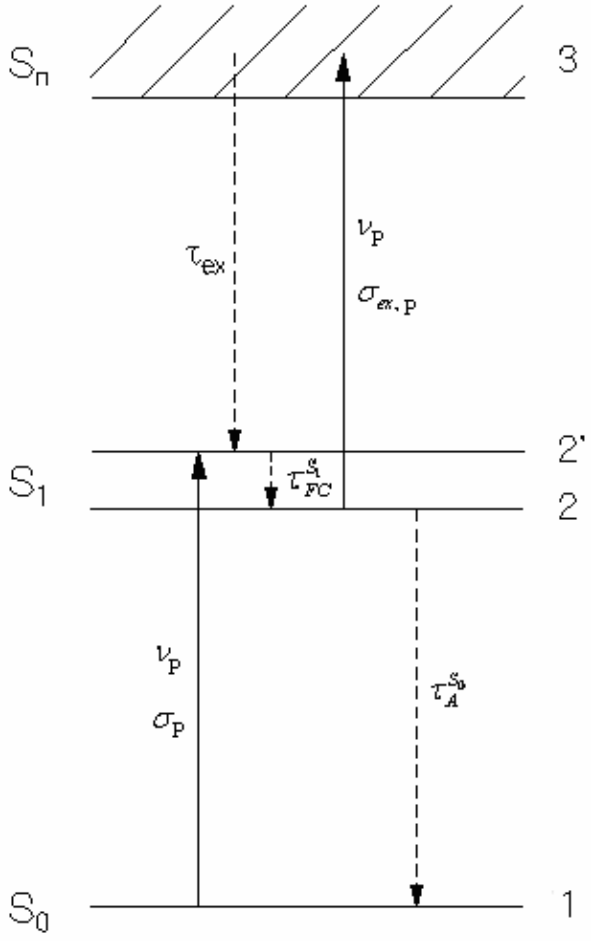

Fig. 2.7: Multi-level system for understanding the behaviour of reverse saturable absorption. S_0: singlet ground state; S_1: first excited singlet state with Franck-Condon level 2' and thermalised level 2; σ_P: ground state absorption cross section; ν_P: pump laser frequency; τ_{FC}: Franck-Condon relaxation time; τ_A: ground state absorption recovery time, τ_{ex}: higher excited state relaxation time and $\sigma_{ex,P}$: excited state absorption cross-section.

2.4 Laser action

The fundamental process of lasing is the interaction of molecules (atoms) with an electromagnetic field, with amplification of the electromagnetic field. The name LASER is the abbreviation of the Light Amplification by Stimulated Emission of Radiation. Laser operation requires that the light amplification factor $A(\lambda) = (\sigma_{em}(\lambda) - \sigma_{ex}(\lambda))N_{ex}l$ should be larger than the light absorption (loss) factor $L(\lambda) = \sigma_a(\lambda)N_a l$. This means that $(\sigma_{em}(\lambda) - \sigma_{ex}(\lambda))N_{ex} > \sigma_a(\lambda)N_a \approx \sigma_a(\lambda)(N_0 - N_{ex})$ is necessary condition for laser action to occur. Here N_{ex} is the population number density of the upper laser level and N_a is the population number density of the lower laser level, N_0 is the total number density of laser active molecules, l is the length of active medium, σ_a, σ_{ex} and σ_{em} are the ground-state absorption cross-section, the excited state absorption cross-section and stimulated emission cross-section respectively.

2.4.1 Stimulated emission

If a photon of appropriate energy interacts with a molecule already in the excited state, that molecule is stimulated to decay and to emit another photon of the same wavelength, polarisation and direction as the original photon. This is illustrated in Fig. 2.8. A photon with energy E_{bA} interacts with a molecule in the excited state S_1, sub level *b*. This interaction stimulates the molecule to decay to the ground state S_0, sub level *A*, with the emission of a photon in phase and with the same energy E_{bA} as the original photon. Only a photon with energy equal to the energy difference of an allowable transition in a molecule will stimulate (induce) emission from an excited molecule.

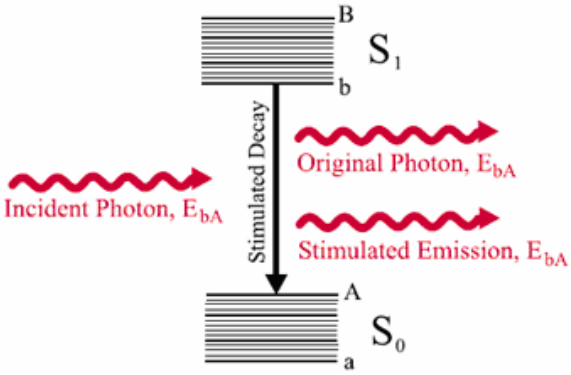

Fig. 2.8: Energy level schematic showing stimulated emission.

2.4.2 Laser amplifier

In a laser amplifier the input light to the active medium is amplified, when the active medium has been population inverted by pumping mechanism. A principle scheme of a laser amplifier is shown is Fig. 2.9. The active medium is population inverted by an excitation source (here indicated by pump with intensity I_P). After inversion an input pulse of intensity I_{in} at wavelength λ_L is amplified to I_{out}. The light amplification is given by

$$I_{out}(\lambda) = I_{in}(\lambda)\exp\left[\left\{\left|\sigma_{em}(\lambda) - \sigma_{ex}(\lambda)\right| N_{ex} - \sigma_a(N_0 - N_{ex})\right\} l\right] \tag{2.3}$$

where σ_{ex} is the excited state absorption cross-section and N_0 is the total number density of molecules.

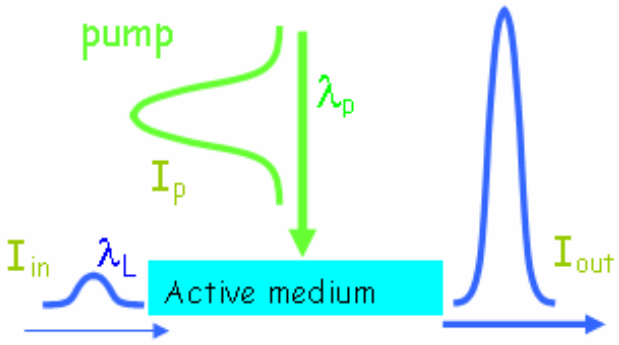

Fig. 2.9: Schematic of a laser amplifier. An input light of wavelength λ_L is amplified in the population inverted active medium. Population inversion is caused by an excitation source (here pump beam).

2.4.3 Amplified spontaneous emission (travelling wave laser, mirror-less laser)

The laser amplifier arrangement of Fig. 2.9, without input light, amplifies the spontaneous emission if the active medium is population inverted by an excitation source. The arrangement is sketched in Fig. 2.10.

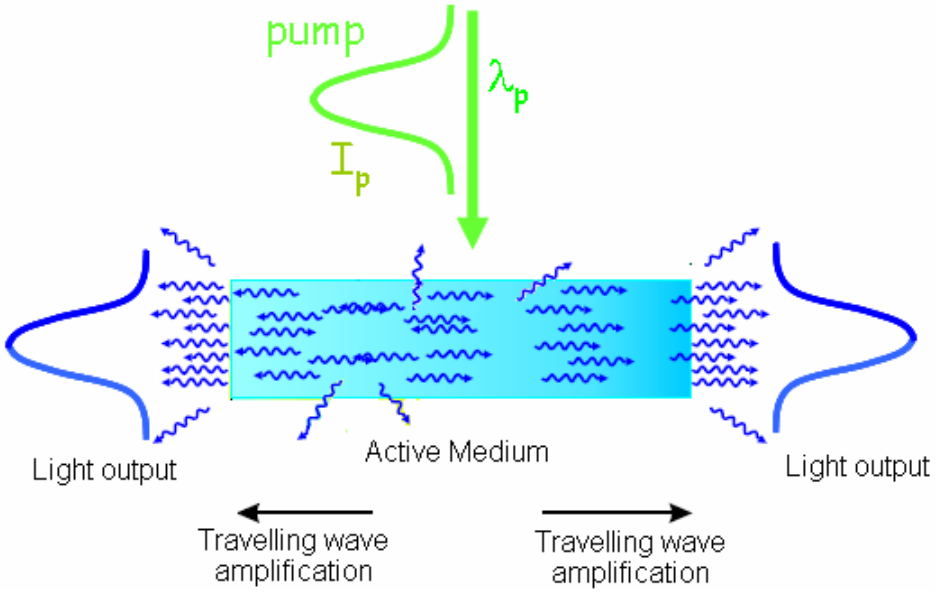

Fig. 2.10: Scheme showing principle of amplified spontaneous emission. The active medium is pumped by a pulse of wavelength λ_P and of intensity I_P to achieve population inversion.

The spontaneous emission is broadband and this broadband is amplified according to the amplification of spontaneous emission and is given by

$$I_{out}(\lambda) = I_{sp}(\lambda)\exp\left[\{(\sigma_{em}(\lambda) - \sigma_{ex}(\lambda))N_{ex} - \sigma_a(\lambda)N_a\}l\right] \tag{2.4}$$

where $I_{sp}(\lambda)$ is the intensity of the spontaneous emission. The amplification of spontaneous emission dominates exponentially in the direction of longest interaction length (l is maximum).

Conjugated polymers and organic dyes typically show strong stimulated emission for the transition from the singlet state S_1,v'=0 to vibronic sublevels of the ground state S_0,v. Due to the fast relaxation out of the vibronic levels, the ground state of the optical transition is usually unpopulated, resulting in a four-level system as shown in Fig. 2.11.

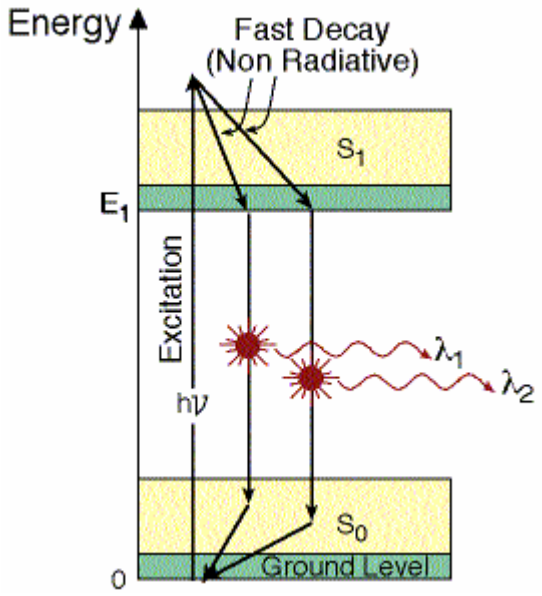

Fig. 2.11: Broadband fluorescence emission, which may be amplified.

In laser active thin films, when the film refractive index is larger than the substrate refractive index and the film is of sufficient thickness, wave-guiding of the spontaneous emitted light within critical angle case takes place [Kog79]. If the population inversion is managed, for example by transverse pumping of the waveguide then wave-guided travelling wave lasing (wave-guided amplification of spontaneous emission) takes place. A typical arrangement is shown in Fig. 2.12.

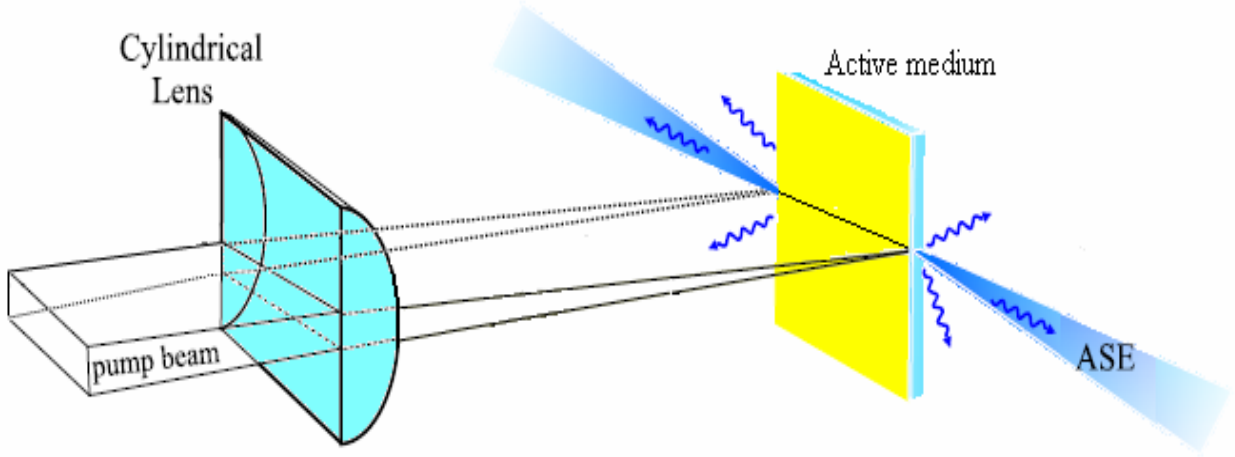

Fig. 2.12: Schematic of amplified spontaneous emission in a thin film waveguide. A cylindrical lens is used to transverse pump a sample thin film.

2.4.4 Laser oscillator

In a laser oscillator the spontaneous emission (and amplified spontaneous emission) is feedback into the active medium by resonator mirrors. The feedback light is amplified in the active medium and the constructive and destructive interference occurs between propagating and reflecting waves (Fabry-Perot interference effect).This leads to specified wavelength selection in laser oscillators. A typical laser oscillator arrangement is shown in Fig. 2.13.

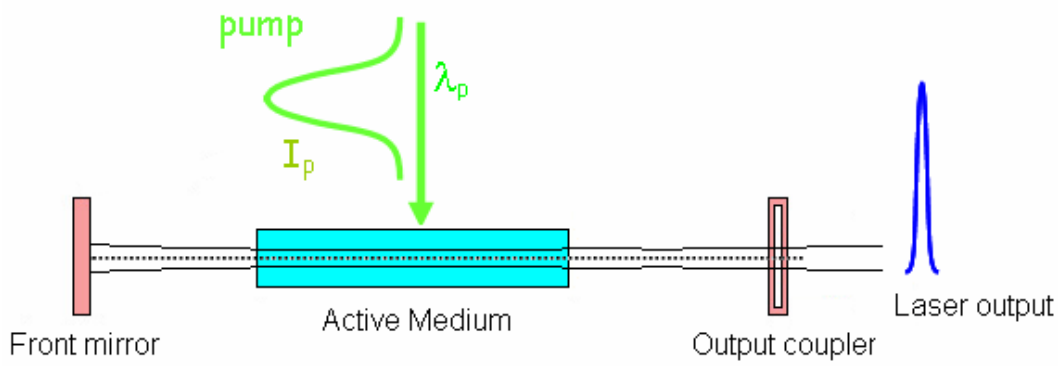

Fig. 2.13: Schematic of a laser resonator.

2.4.5 Low-Q laser oscillator

In a low Q laser oscillator the laser quality factor Q is small (number of round trips before photon escapes the resonator is small). This situation occurs if the output coupler has high transmission (low reflectivity) or back side front mirror (usually 100% reflectivity) and the output mirror have low reflectivity. In our low-Q-laser studies, the low-Q resonator is formed by the uncoated optically polished glass windows of a cell which contains the active laser medium (the molecule solution under study). The solution in the dye laser cell is transversely pumped with the help of a cylindrical lens. A schematic low-Q laser arrangement is shown in Fig. 2.14.

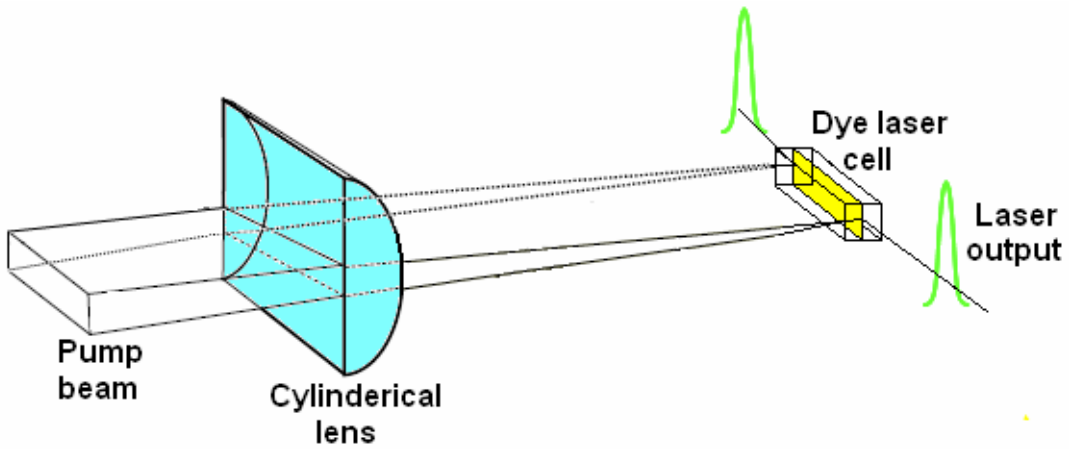

Fig. 2.14: Schematic of a transverse pumped low-Q laser. The dye laser cell is transversely pumped with the help of a cylindrical lens.

2.4.6 Distributed feedback laser

The concept of distributed feedback (DFB) lasers was introduced in the early 1970s by Kogelnik et al., who realized that laser operation can be achieved if a periodic structure is integrated within the gain region [Kog71]. In such types of devices, light is reflected by the periodic modulation of the refractive index or the gain so that light is Bragg reflected. This is the major difference in comparison to a conventional laser device as shown in Fig. 2.13, where the feedback is established by end mirrors. The laser wavelength of a DFB laser is close to the Bragg wavelength, $\lambda_{Bragg} = 2n_{eff}\Lambda$ (n_{eff} is the effective refractive index of the waveguide and Λ is the period of the grating), and the wavelength can be tuned by varying either the effective refractive index, n_{eff} or the period of the grating, Λ. The DFB lasers made with periodic modulation in the refractive index normally lase in two modes [Sha71], one slightly below of λ_{Bragg} and another one slightly above this. Single mode DFB lasers can be made by introducing a phase shift in the

periodic modulation or by modulating gain instead of refractive index. Fig. 2.15 depicts an example of a DFB structure.

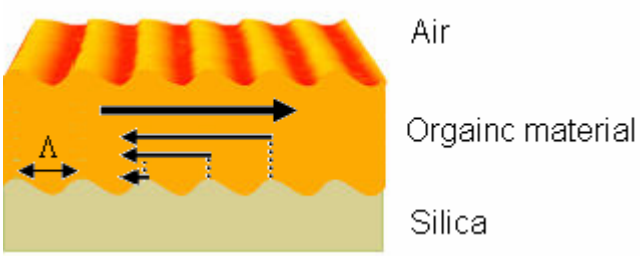

Fig. 2.15: Schematic diagram of an organic material DFB laser with corrugations of period of Λ. Light of wavelength $\lambda = 2n_{eff}\Lambda$ propagating from left to right is scattered from the periodic structure to create a diffracted wave propagating in the counter propagating waveguide [Sam07].

The DFB geometry is very attractive for semiconducting organic lasers for several reasons. As organic material based thin films can be readily made by spin-coating, the film can be pumped transversely and the laser structure allows light to propagate through significant distances in the gain medium. As the feedback is provided by corrugation rather than mirrors so no alignment of the laser is required, and the corrugation can be used to give a well-defined output beam, by diffracting some light out of the face of the film.

3. Experimental techniques

3.1 Investigated electroluminescent organic materials

The work presented in this dissertation consists of two types of electroluminescent organic materials: some low molar mass molecules and a polymer. The low molar mass molecules are dicarboxovinylene-MEH-phenylene : full name (1,4-bis(9-ethyl-3-carbazovinylene-2-methoxy-5-(2'-ethyl-hexyloxy)-phenylene), abbreviated by (2CzV-MEH-B) [Ban08a], triphenylamine dimer: full name (N,N,N',N'-tetraphenylbenzidine), abbreviated by (TPB) [Ban08b], napthalene substituted triphenylamine dimer: full name (N,N'-di-[1-napthaalenyl)-N,N'-diphenyl]-(1,1´-biphenyl)-4,4'-diamine), abbreviated by (β-NPB) [Ban08b], triphenylamine (TPA) [Ban08c], tris-3 methyl-triphenylamine: full name (1,3,5-tri(3-methylphenyl-phenylamino)benzene) abbreviated by (m-MTDAB) [Ban08c]. The studied polymer is poly (2,2'-dipyridine-5,5'-diyl-2,5-dihexyl-1,4-phenylene) abbreviated by (PPBpy) [Ban08d]. The structural formulae and chemical names of the compounds are shown in Fig. 3.1.

All these electroluminescent organic materials were characterized spectroscopically and investigated for neat thin-film laser action. The light emitting oligomer 2CzV-MEH-B (product name: ADS084BE) and the hole transport material m-MTDAB (product name ADS04HTM) were bought from American Dye Source, Inc. Quebec. The hole transport materials TPB and β-NPB were bought from Sensient Imaging Technologies GmbH, Wolfen, Germany. The triphenylamine TPA and the solvents tetrahydrofuran and 1,1,2,2-tetrachloroethane were purchased from Sigma-Aldrich, Taufkirchen, Germany. All the organic materials and solvents were used without further purification. The polymer PPBpy was synthesized in the group of

Professor Klemn, Institut für Organische Chemie und Makromolekulare Chemie, Friedrich-Schiller Universität Jena, Germany.

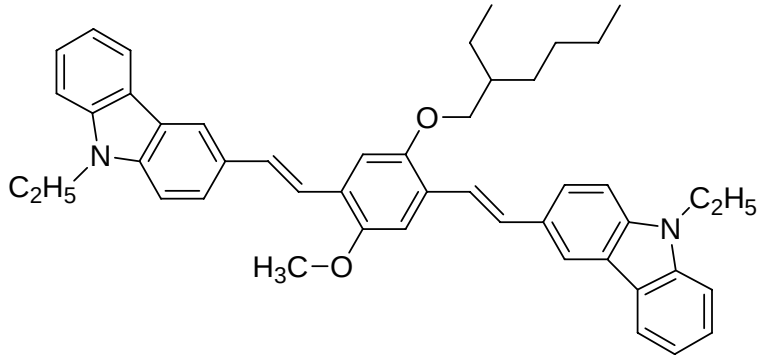

2CzV-MEH-B

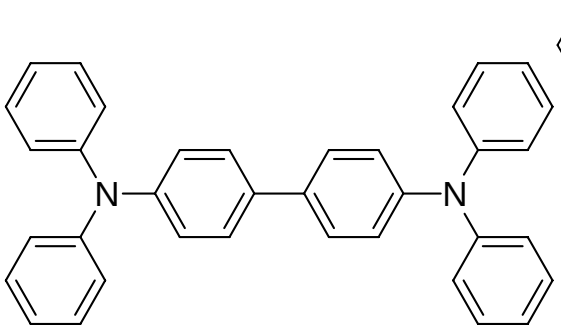

TPB

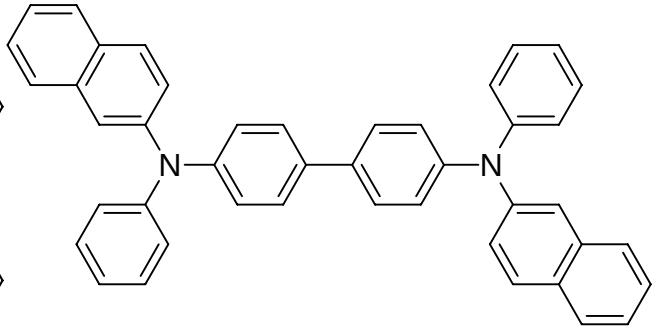

β-NPB

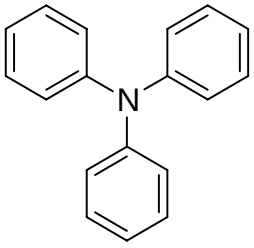

TPA

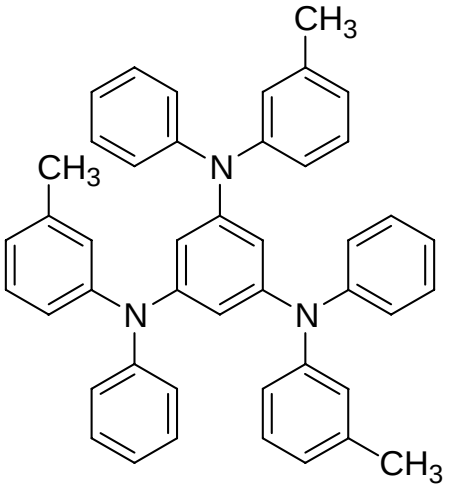

m-MTDAB

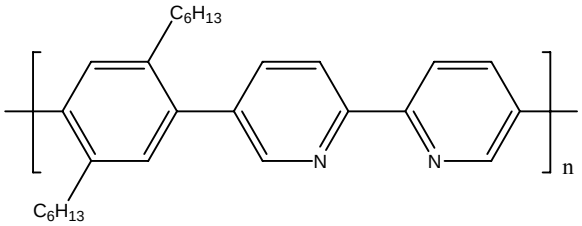

PPBpy

Fig 3.1: Structural formulae of investigated electroluminescent materials. **2CzV-MEH-B**, Full name: 1,4-bis(9-ethyl-3-carbazovinylene-2-methoxy-5-(2'-ethyl-hexyloxy)-phenylene (sum formula: $C_{47}H_{50}N_2O_2$. Molar mass: 674.91 g mol^{-1}). **TPB**: Full name: N,N,N',N'-tetraphenylbenzidine (sum formula: $C_{36}H_{28}N_2$. Molar mass: 488.64 g mol^{-1}). **β-NPB**: Full name: N,N'-di-[1-napthaalenyl)-N,N'-diphenyl]-(1,1´-biphenyl)-4,4'-diamine (sum formula: $C_{44}H_{32}N_2$. Molar mass: 588.76 g mol^{-1}). **TPA**: Full name: Triphenylamine (sum formula: $C_{18}H_{15}N$. Molar mass: 245.32 g mol^{-1}). **m-MTDAB**: Full name: 1,3,5-tris (3-methylphenyl-phenylamino) benzene (sum formula: $C_{45}H_{39}N_3$. Molar mass: 621.83 g mol^{-1}).
PPBpy: Full name: poly(2,2'-dipyridine-5,5'-diyl-2,5-dihexyl-1,4-phenylene) (sum formula: $C_{28}H_{34}N_2$. Molar mass: 398.6 g mol^{-1}).

The organic materials were dissolved in tetrahydrofuran (C_4H_8O) or 1,1,2,2-tetrachloroethane ($C_2H_2Cl_4$). All the measurements were performed at room temperature (ca. 22 °C) under ambient conditions.

3.2 Film preparation

The thin films used in this work were prepared by spin coating on suitable substrates. The spin coating on substrates was done by the instrument shown in Fig 3.2 built in our electronic and mechanical workshops. The schematic shows a plexiglas box with front side open. A sample holder is located on a rotating disk. The sample holder is different for different sample types. The speed of the rotating disk is controlled by D1 and D2 knobs on the controller box. A rotary switch S enables the exchange between the two stages D1 and D2. The first stage reaches a maximum angular speed of approximately 600 rpm (rotations per minute). The second stage enables an

angular speed in the range of about 400-3000 rpm. The whole arrangement was covered for safety purpose and located in the fume hood for evaporating solvent exhaustion.

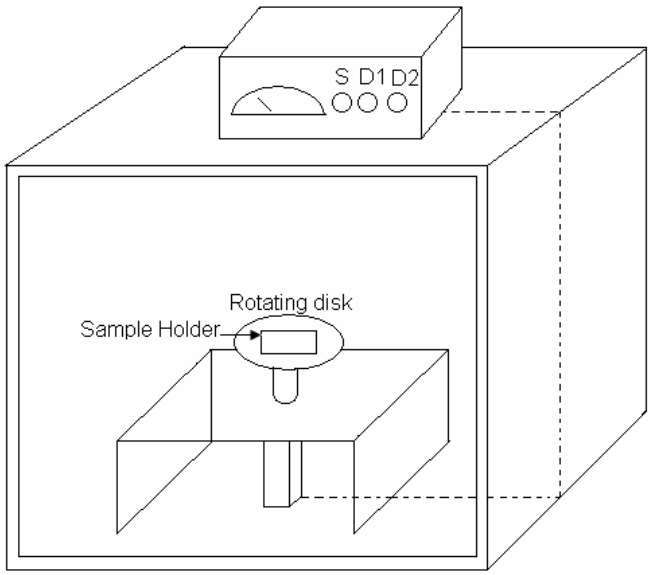

Fig. 3.2: Experimental arrangement for spin coating.

For the travelling-wave laser action experiments microscope slides, (type SUPERIOR Paul Marienfeld GmbH and Co KG, Lauda-Königshofen, Germany) were used as substrates. The dimensions of the substrates used were 38 mm × 26 mm × 1 mm ($l \times b \times h$). For the optical spectroscopic characterizations (absorption, fluorescence and optical constants) of the luminescent organic materials as thin films, the substrate used was synthetic quartz glass, Spectrosil B [The66]. The dimensions of the substrate quartz glasses were 50 mm × 30 mm × 3mm ($l \times b \times h$).

The wet substrates were put on the rotating disk for one minute at rotational speed of 2400 rpm to dry them completely. Subsequently to make a film of desired thickness, the speed was reduced. The thickness of the film is inversely proportional to the number of revolutions and is directly proportional to the square of concentration of the dye in the solvent [Dro98]. Depending on the desired film thickness, the used solvent and the kind of organic material, rotational speeds

between 600 rpm to 1800 rpm were selected. After the rotating disk achieved the desired speed, one or two drops of the dye solution were brought exactly in the middle of the rotating substrate with the help of a Pasteur pipette. One drop of organic material from the Pasteur pipette corresponds to a quantity of roughly 0.015 ml. The rotating disk speed was kept constant for about 1 min. During this time the solvent evaporated at ambient temperature. Subsequently, the spin-coater was switched off and the sample was taken out from the holding template.

The thin films used for laser experiments were generally made from dye solutions of 20mg/ml concentration. For example, to make a film of thickness of approximately 100 nm, a rotational speed of 1200 rpm was used. For the measurement of the optical constants, the fluorescence quantum yield and fluorescence lifetime, film thicknesses of around 50nm to 90nm were needed. In this case a rotational speed about 2000 rpm was used.

After preparation, the films were stored for about 30 minutes at ambient temperature to let the remaining solvent to evaporate and after that they were stored at 4˚C in a refrigerator.

3.3 Optical constants and film thickness measurement

The optical constants, refractive index *n* and absorption coefficient α, were determined by reflection and transmission measurements. The experimental arrangement for the reflection and transmission measurements over a wide wavelength range is shown in Fig. 3.3. The sample (thin film on substrate) was mounted on a mirror holder on a rotation stage. The illumination part, consisting of a light source (tungsten lamp 12V), two apertures B1, B2, a lens L1, and a vertically polarized polarizer P, was mounted on a swivel arm with center of rotation at the sample position. It can be positioned to any angle between 8˚ and 180˚. The position of ϕ=180˚ was used for transmission measurement. For reflection measurement at an angle of incidence, φ_a, the swivel arm was set to $\phi = 2\varphi_a$. The detection part consisted of a spectrometer with a silicon diode array

detection system, an aperture B3 and a lens L2. The quartz lens L2 collected the transmitted or reflected light to the entrance slit of the spectrometer. The reflected and the transmitted light spectra were calibrated to the light spectra obtained when the light source was in the transmission measurement position and the sample had been removed.

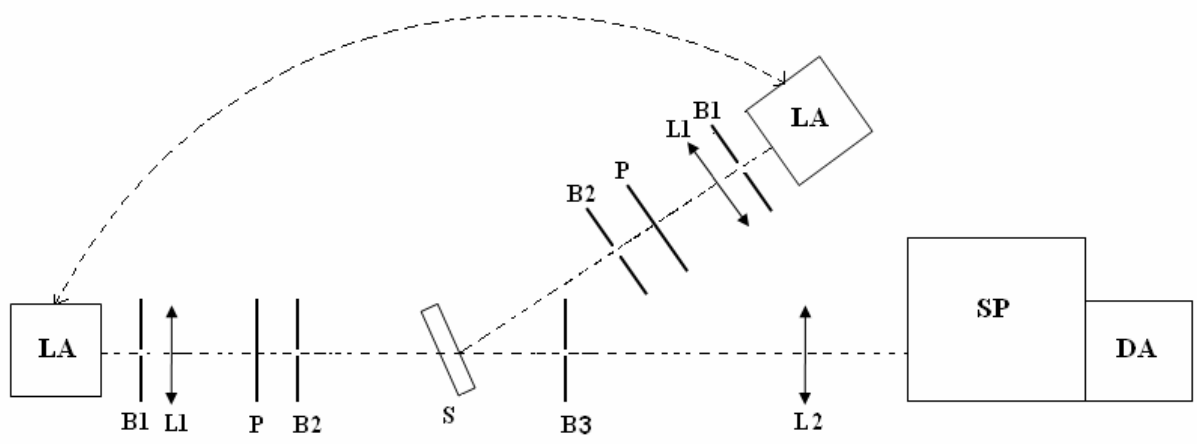

Fig. 3.3. Experimental arrangement for spectral reflectance and transmittance measurement. S, sample; LA, lamp; B1, B2, B3, apertures; P, polarizer; L1, L2, lenses; SP, spectrometer; DA, diode array detection system; movement possibility of swivel arm is indicated by arced arrows.

The refractive index dispersion, $n(\lambda)$, the absorption coefficient spectrum, $\alpha(\lambda)$, and the thin film thickness l are extracted from the reflection and transmission measurements [Bor80]. A detailed description of data extraction from the transmission and reflection measurements is given in [Pen98].

3.4 Absorption measurement

The absorption measurements of organic materials in liquid solutions were carried out using a commercial single beam UV-VIS-IR spectrophotometer (Cary 50 from Varian and Beckman ACTA M IV) by measuring transmission spectra $T(\lambda)$. The absorption coefficient spectra, $\alpha(\lambda)$, are derived from the transmission spectra by using the relation

$$T(\lambda) = \exp[-\alpha(\lambda)\,\ell] \tag{3.1}$$

where *l* is the sample length.

The absorption cross-section spectra, $\sigma_a(\lambda)$, are related to the absorption coefficient spectra, $\alpha(\lambda)$, by the relation, $\sigma_a(\lambda) = \alpha(\lambda)/N_0$, where N_0 is the number density of molecules or repeat units.

The absorption cross-section spectra of the neat films of organic materials were determined by assuming equal absorption cross-section integrals in solutions and in thin films for the S_0-S_1 absorption band by using the relation

$$\sigma_{a,F}(\lambda) = \frac{\alpha(\lambda)}{\int_{S_0-S_1} \alpha(\lambda')\lambda'^{-2}\,\mathrm{d}\lambda'} \int_{S_0-S_1} \sigma_a(\lambda')\lambda'^{-2}\,\mathrm{d}\lambda' \tag{3.3}$$

The assumption is reasonable since the absorption integrals or oscillator strength of allowed transitions depends little on solvent and concentration [Bir70].

The molecule mass density N_0 or ρ of the molecules in thin films was determined by using the relation

$$\sigma_{a,F}(\lambda) = \frac{\alpha(\lambda)}{N_0} = \frac{\alpha(\lambda)M}{\rho N_A} \tag{3.2}$$

where *M* is the molar mass, N_A is the Avogadro number.

3.5 Fluorescence quantum distribution measurement

Fluorescence measurements were carried out using a self assembled fluorimeter in front face collection arrangement. The experimental setup is shown schematically in Fig. 3.4. The setup consists of an excitation part and a detection part. In the excitation part, a 200 Watt high-pressure mercury lamp (from Spindler and Hoyer, Göttingen (now LINOS)) in combination with an interference filter (to select the desired wavelength) and a polarizer P1 is used as excitation source. The vertically polarized excitation light is focused to the sample S by lens L2. In the

detection part the fluorescence emission is collected by lens L3 and focused to the spectrometer SP with lens L4 under conditions of parallel, perpendicular or magic angle polarizer direction (polarizer transmission under an angle of 54.74° to the vertical for magic angle polarization [Dör66]) relative to the polarization direction of the excitation light. The dispersed fluorescence spectrum is collected by a silicon diode array detection multi-channel analyser system (Tracor DARRS system TN-1710, from Tracor Northern).

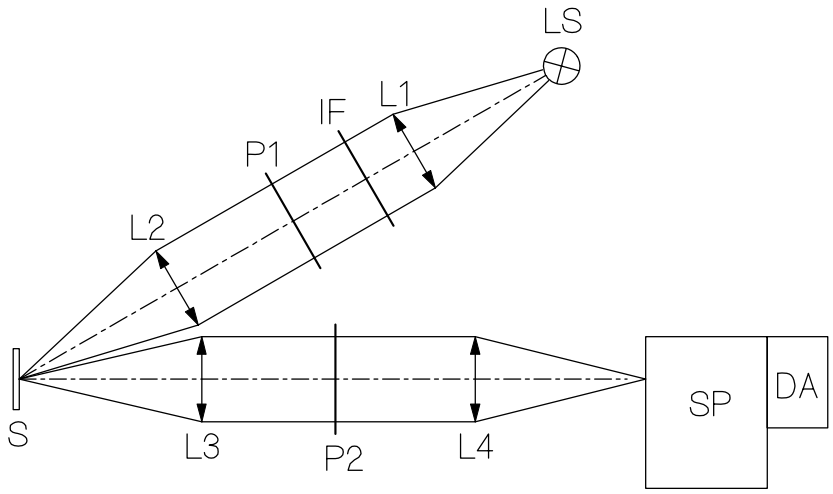

Fig. 3.4: Experimental setup for fluorescence measurements. LS, light source (high pressure mercury lamp); IF, interference filter; L1-L4, lenses; P1, P2, linear dichroitic polarizer sheets; S, sample; SP, spectrometer; DA, diode-array detection system.

The absolute intrinsic fluorescence quantum distribution, $E_F(\lambda)$, which is defined as the ratio of total intrinsic fluorescence photons integrated over the full solid angle to the absorbed excitation photons [Pen87], is given by

$$E_F(\lambda) = \frac{S_i(\lambda)}{S_{abs}} \tag{3.4}$$

where $S_i(\lambda)$ is the number of intrinsic fluorescence photons per unit wavelength and per volume element and S_{abs} is the number of absorbed pump photons in the same volume element.

The fluorescence quantum yield, ϕ_F, which is defined as the total number of intrinsic fluorescence photons to the number of absorbed light photons, is given by

$$\phi_F = \int E_F(\lambda) d\lambda \tag{3.5}$$

In the experiments the fluorescence quantum distribution, $E_F(\lambda)$, and fluorescence quantum yield, ϕ_F, were determined by calibration to reference dyes of known fluorescence quantum yield [Hol99, För51].

For excitation in the blue and violet spectral range the dye Coumarin 314T in ethanol was used as reference (fluorescence quantum yield ϕ_F = 0.87 according to technical data sheet of Kodak). The Fig. 3.5 shows the absorption cross-section spectrum and the fluorescence quantum distribution of the dye coumarin 314T in ethanol. In the case of near UV excitation the dye quinine- sulphate dihydrate in 1N H_2SO_4 was used as reference (ϕ_F = 0.546/ (1+14.5 *C*) where *C* is the dye concentration in mol dm^{-3} [Mel61]). The absorption cross-section spectrum and fluorescence quantum distribution of this dye are shown in Fig. 3.6.

The degree of fluorescence polarization [Dör66], P_F was determined by vertical polarized excitation and detection of the fluorescence signal polarized parallel ($S_{F,\|}$) and perpendicular ($S_{F,\perp}$) to the excitation light and by using the relation

$$P_F(\lambda) = [S_{F,\|}(\lambda) - S_{F,\perp}(\lambda)] / [S_{F,\|}(\lambda) + S_{F,\perp}(\lambda)] \tag{3.6}$$

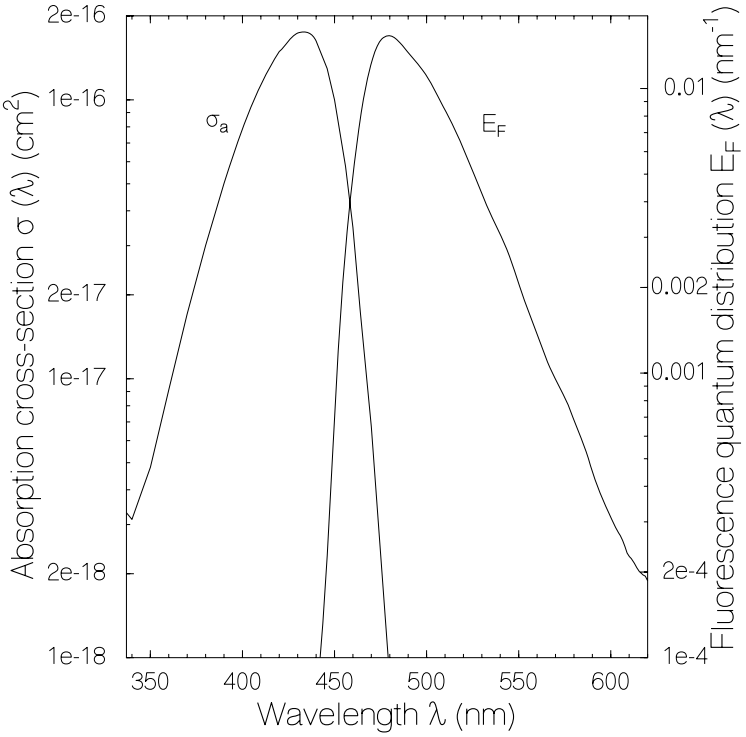

Fig. 3.5: Absorption cross-section spectrum and fluorescence quantum distribution of Coumarin 314T in ethanol.

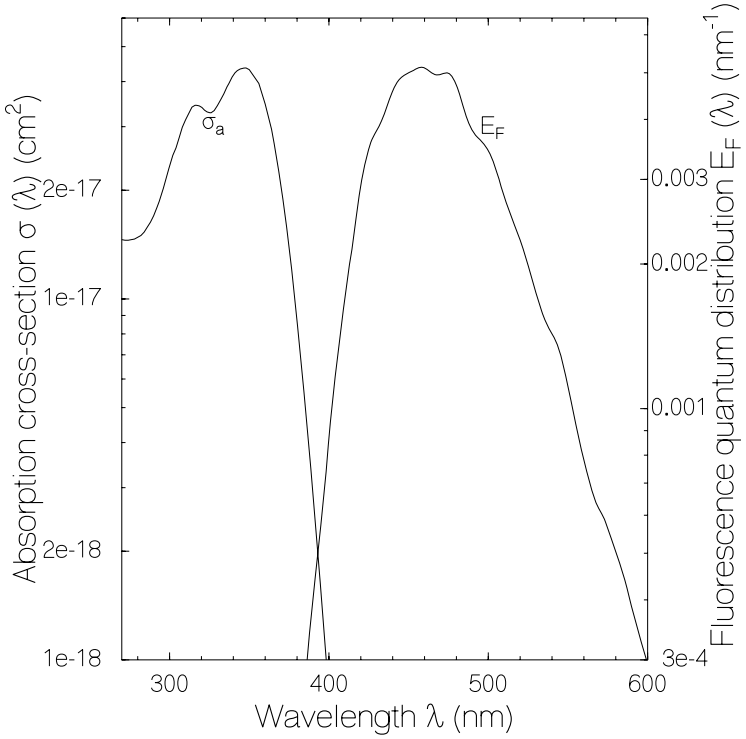

Fig. 3.6: Absorption cross-section spectrum and fluorescence quantum distribution of quinine-sulphate dihydrate in 1N H_2SO_4.

3.6 Fluorescence lifetime measurement

Fluorescence lifetime measurements of samples with lifetimes longer than about 500 ps were carried out using the experimental setup depicted in Fig. 3.7a. The samples were excited by vertical-polarized second harmonic pulses of an active and passive mode-locked ruby laser [Wei93] (pulse duration 35 ps, wavelength 347.15 nm). For detection the fluorescence was gathered by lens L1 and directed to a micro-channel-plate photomultiplier (Hamamatsu, type R1564-U01) by lens L2 under magic angle orientation (polarizer transmission under an angle of 54.7° to the vertical [Dörr66]). The photomultiplier signal was recorded with a high-speed digital oscilloscope (LeCroy, type DSO 9362). In the fluorescence path, an edge filter (EF) was used to cut unwanted excitation light.

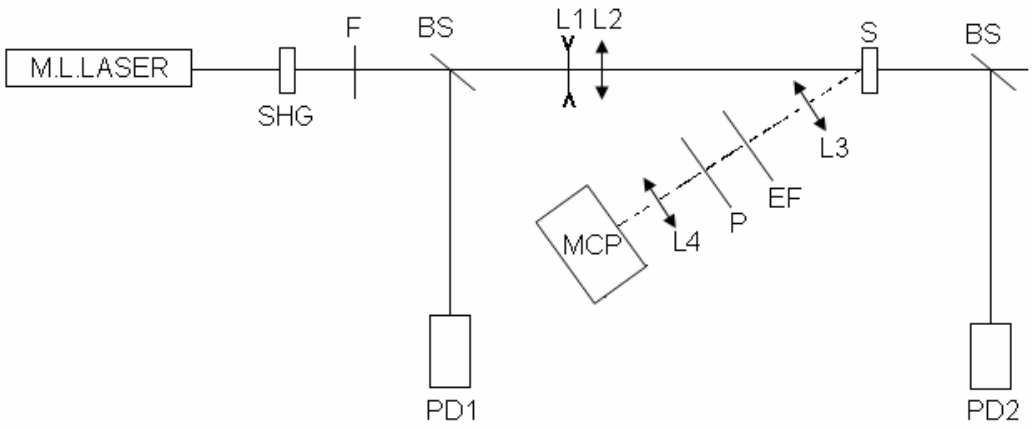

Fig. 3.7a: Experimental setup for fluorescence lifetime measurement. M.L.Laser, active and passive mode-locked ruby laser; SHG, KD*P crystal for second harmonic generation; F , filter to cut the fundamental light; L1,L2, beam expanding telescope; L3,L4, fluorescence collecting lenses; S, sample; EF, long-pass edge filter (λ>370 nm); P, polarizer at magic angle (54.7˚); PD1, PD2, photodetectors; MCP, micro-channel-plate photomultiplier.

For the investigated neat film of 2CzV-MEH-B the fluorescence lifetime came out to be shorter than 500 ps and could not be resolved by the micro-channel plate detector system. In this case temporal fluorescence traces were measured by excitation with second harmonic pulses of a titanium sapphire femtosecond laser (pulse duration 130 fs, wavelength 400 nm, laser system

Hurricane from Spectra-Physics) and fluorescence signal detection with a picosecond single sweep streak-camera (Hamamatsu type C1587 temporal photometer with M1952 high speed repeat unit , time resolution ≤ 2 ps). The experimental arrangement is shown in Fig. 3.7b. The operating principle is described in [Hol00a].

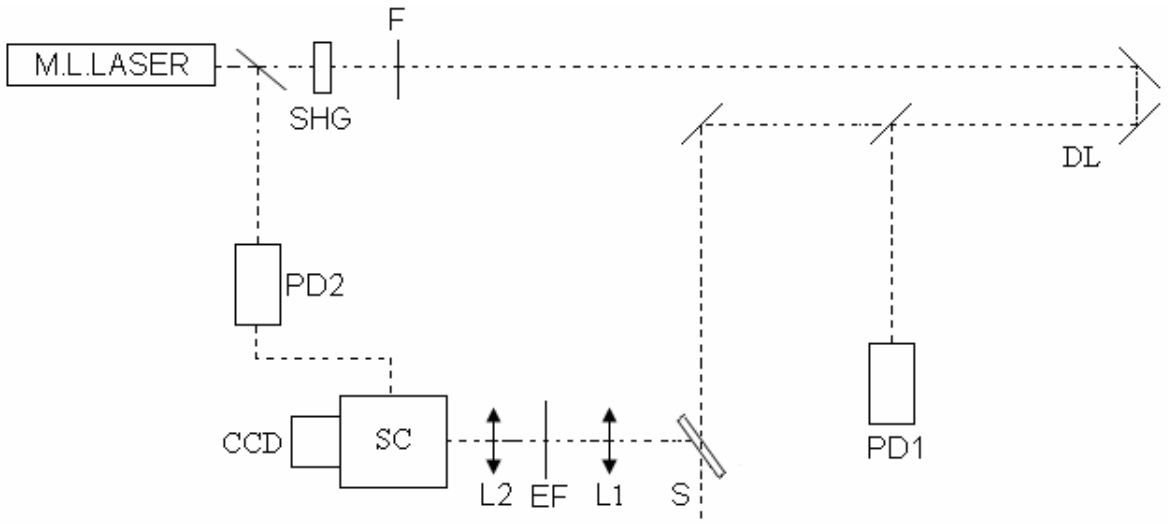

Fig. 3.7b: Experimental setup for time-resolved analysis with streak camera. M.L.Laser, active and passive mode-locked ruby laser; SHG, KD*P crystal for second harmonic generation; F , filter to cut the fundamental light; L1,L2, fluorescence collecting lenses; S, sample; EF, long-pass edge filter (λ>400 nm); PD1, energy calibrated photodetector; SC, streak camera; CCD, intensified two-dimensional CCD camera; PD2, trigger photodiode; DL, optical delay line.

3.7 Saturable absorption measurement

The saturable absorption behaviour of sample solutions in THF or in TCE at room temperature was studied using the experimental setup depicted in Fig. 3.8. Single picosecond light pulses were selected from an active and passive mode-locked ruby laser (pulse duration 35 ps FWHM). The pulses were amplified and the second harmonic was generated in a KD*P crystal. The intensity of the pulses at the sample was varied with filters and a lens L1. The energy transmission through the sample cell was measured with photodetectors PD1 and PD3. The input peak pulse intensity was determined by two photon transmission measurements through a KI crystal (thickness 1cm) with photodetectors PD1 and PD2 [Bla81]. The two-photon transmission

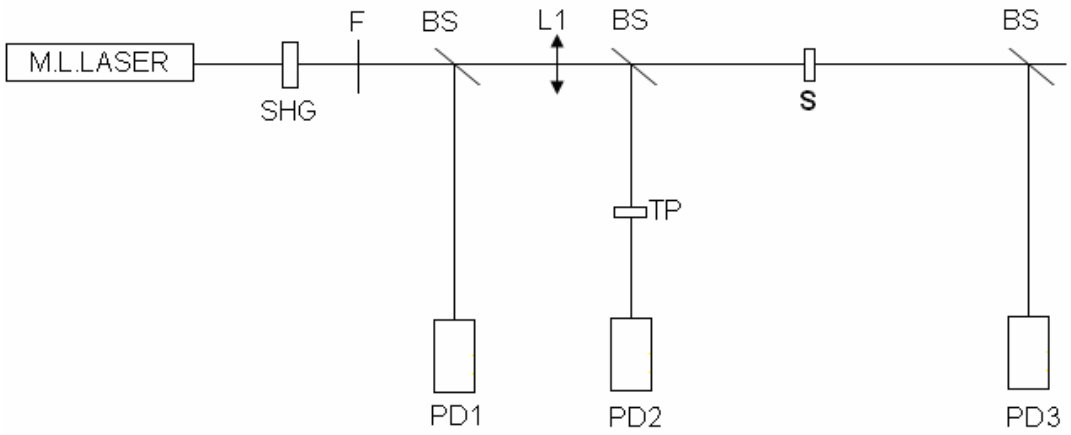

Fig. 3.8: Experimental setup for saturable absorption measurement. M.L.Laser, active and passive mode-locked ruby laser; SHG, KD*P crystal for second harmonic generation; F, Filter; L1 lens; TP: KI crystal for Intensity detection; S, sample; PD1, PD2, and PD3 photodetectors.

of the KI crystal versus input peak intensity I_0 is shown in Fig. 3.9. The excited-state absorption cross-section of the samples at the excitation wavelength is extracted from the dependence of the energy transmission T_E on the input laser peak intensity I_0.

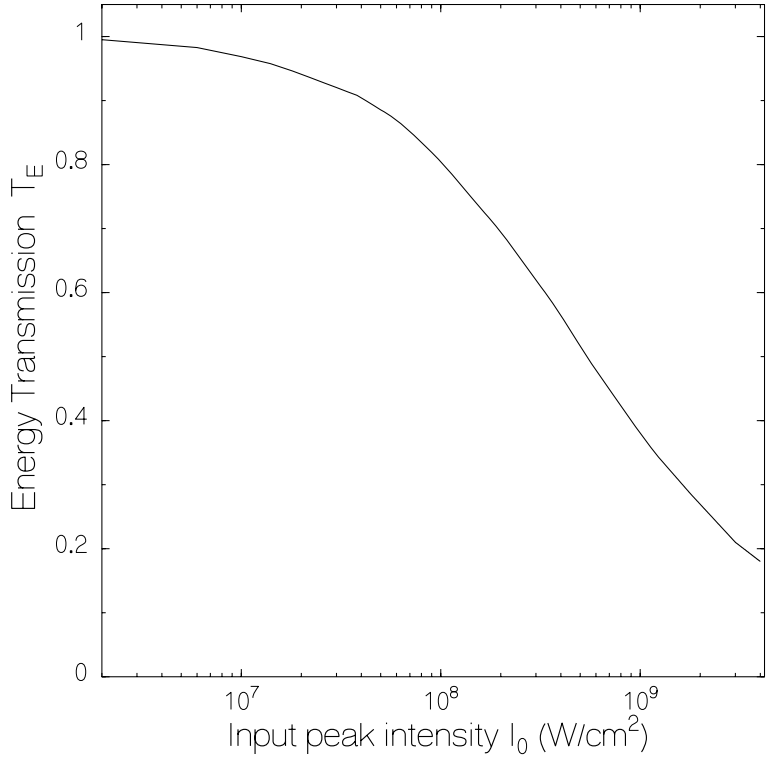

Fig. 3.9: Two photon energy transmission through a KI crystal of length 1 cm [Bla81].

3.8 Low-Q laser studies

The low-Q lasing arrangements of organic materials in a 1 cm × 1 mm quartz dye-laser cell were studied using vertical-polarised second harmonic pulses of a picosecond ruby laser system [Wei93] (wavelength λ_P = 347.15 nm, pulse duration Δt_P = 35 ps, pulse energy up to 1 mJ). The experimental arrangement is shown in Fig. 3.10.

The input pump pulse peak energy density, w_{0P}, is varied with neutral density filters. The samples were transversally pumped. The vertical polarized laser beam was elongated along the horizontal-optical axis with a concave cylindrical lens, C1 (beam extension to 14.5 mm FWHM), and focused perpendicular to the horizontal-optical axis with a convex cylindrical lens, C2 (beam

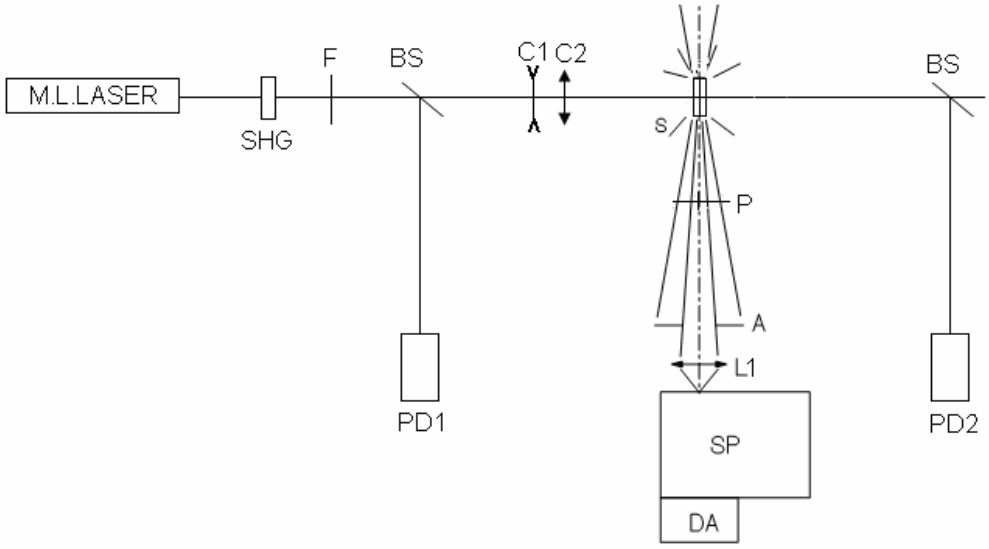

Fig. 3.10: Experimental setup of travelling wave lasing. M.L.Laser, active and passive mode-locked ruby laser; SHG, KD*P crystal for second harmonic generation; F, filter; C1, C2, cylindrical lenses for pump pulse line-focus formation; S, sample; P, polarizer; A, aperture; L1 lens; PD1, PD2, photodetectors; SP, spectrometer; DA, diode-array detection system.

narrowing to 0.245 mm FWHM). The excitation occurred along the 1 cm cell side, perpendicular to the 1mm cell windows. The cell windows acted as resonator mirrors (reflectivity $R \approx 0.036$). The detection part consists of a vertically polarized polarizer dichotic sheet, an aperture A with diameter 3 mm at 21 cm distance from the sample, and a lens L1. The aperture, A restricts the

full collection angle to $\Delta\theta = 0.82^{\circ}$, Lens L1 (focal length $f_1 = 100$ mm) focuses the emitted light to a spectrometer, SP, with diode-array detection system, DA (OMA system with intensified detector model 1455 from EG&G Princeton Applied Research). The silicon photodetectors PD1 and PD2 were used to measure the transmission through the samples. The input pulse energy W_P is measured with the energy calibrated photodetector, PD1. The pump laser beam width and height (FWHM), at the sample position were measured separately with a diode array camera.

3.9 Wave-guided travelling-wave laser studies

The amplification of spontaneous emission (ASE) of neat thin films was studied using second harmonic pulses of a picosecond ruby laser system [Wei93] (wavelength $\lambda_P = 347.15$ nm, pulse duration $\Delta t_P = 35$ ps, pulse energy up to 1 mJ). The experimental arrangement of ASE generation and detection is shown in Fig. 3.11. The samples are transversally pumped. The laser beam is elongated along the horizontal-optical axis with a concave cylindrical lens, C1 (beam extension to 14.5mm FWHM), and focused perpendicular to the horizontal-optical axis with a convex cylindrical lens, C2 (beam narrowing to 0.245 mm FWHM). The sample surface was tilted ($\alpha \approx 7^{\circ}$) off the perpendicular direction towards the excitation beam direction for better collection of the light propagating along the film substrate interface [Pen04]. The emission is collimated with lens L1 (focal length $f_1 = 65$ mm). An aperture, A (opening diameter d = 20 mm), restricts the full collection angle to $\Delta\theta = 17.5^{\circ}$. A lens L2 ($f_2 = 100$ mm) focuses the collimated light to a spectrometer, SP, with diode-array detection system, DA (OMA system with intensified detector model 1455 from EG&G Princeton Applied Research). The thickness, d, of the neat films for ASE measurements was determined by the neat film transmission, $T'(\lambda_P)$, measured at the laser excitation wavelength, λ_P. It is $T'(\lambda_P) = T(\lambda_P)/T_S(\lambda_P) = \exp(-\alpha_P d)$, where $T(\lambda_P)$ is the

transmittance of the neat film and the substrate, $T_S(\lambda_P)$ is the transmittance of the blank substrate and α_P is the absorption coefficient.

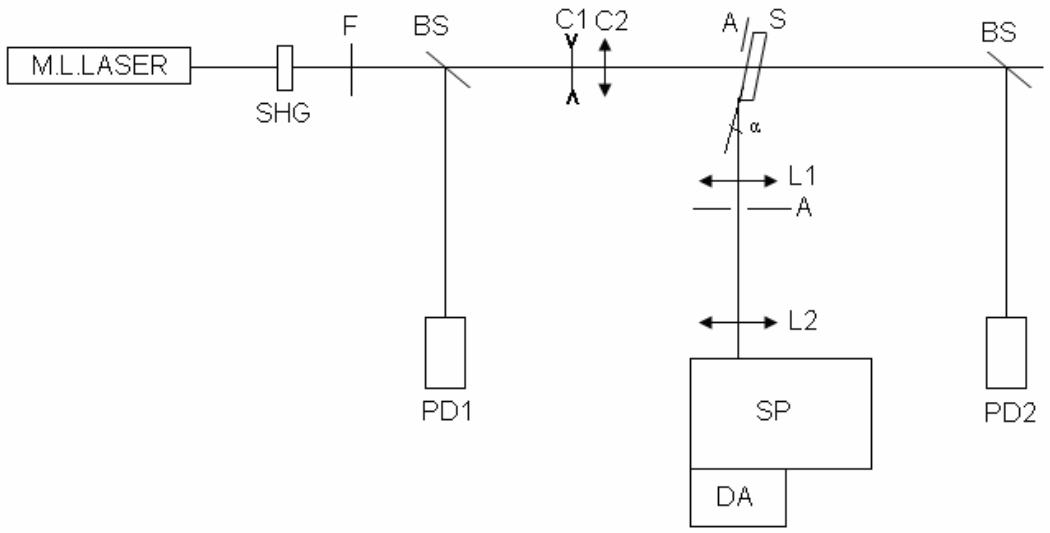

Fig. 3.11: Experimental setup for wave-guided travelling-wave lasing. M.L.Laser, active and passive mode-locked ruby laser; SHG, KD*P crystal for second harmonic generation; F, blocking filter for fundamental laser light; C1, C2, cylindrical lenses; S, sample; A, aperture; L1, L2 lenses; PD1, PD2, photo detectors; SP, spectrometer; DA, diode-array detection system.

The effective gain length (interaction length) of wave-guided travelling wave lasing, l_{TWL}, is determined by changing the exposed sample length, l_{ap}, with a variable slit A and measuring the threshold pump power energy density, $w_{P,th}$.

3.10 Distributed-feedback laser studies

For the distributed feedback lasing studies on organic materials (2CzV-MEH-B and PPBpy), the used experimental arrangement is shown in Fig. 3.12. Vertically polarised single second harmonic pulse of a picosecond ruby laser system [Wei93] (wavelength λ_L = 347.15 nm, pulse duration $\Delta t_L \approx$ 35 ps, pulse energy up to 1 mJ) were used for transversely exciting the samples. The pump pulse energy was measured with a calibrated photo-detector, PD1 (sensitivity 0.68±0.018 nJ/V). The negative cylindrical lens C1 (beam expansion in horizontal plane) and the positive cylindrical lens C2 (beam narrowing in vertical plane) form a line focus along the grating

axis. The beam diameter perpendicular to grating axis is $\ell_{\perp}$ = 0.13 mm. The beam diameter along grating axis is limited to $\ell_{\parallel}$ = 0.9 mm by an aperture, in order to avoid amplified spontaneous emission outside the grating region and to avoid imperfections at the grating – flat-surface borders. The samples were tilted to an angle of 45° to the excitation direction with grooves in vertical direction. The first-order-diffraction radiation mode (M = 1), which is emitted normal to the grating plane [Car98, Mor97], is collected by a lens, L, and detected spectrally resolved by a spectrometer, SP, with diode-array detection system, DA (OMA system with intensified detector model 1455 from EG&G Princeton Applied Research). The gratings were operated in second grating order (p = 2, Bragg wavelength $\lambda_{m,Bragg} = \Lambda$) [Hol02a]. The gratings were fabricated on fused silica plates. The grooves were processed by reactive ion beam etching [Hol02a]. The organic material films were deposited by spin coating as described earlier.

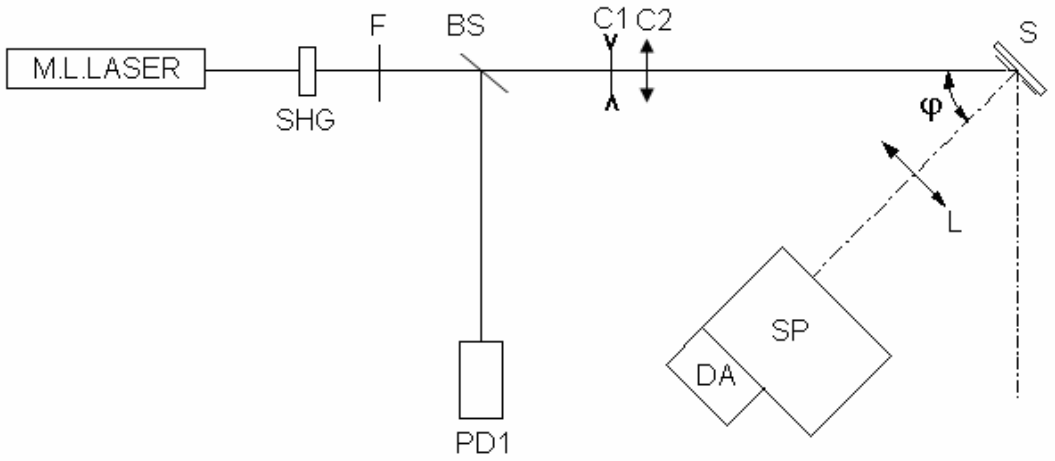

Fig. 3.12: Experimental arrangement for distributed-feedback lasing. M.L.Laser, modelocked ruby laser system; SHG, KD*P crystal for second-harmonic generation; F, filter; BS, beam splitter; C1, C2, cylindrical lenses; L, Lens; S, sample; φ = 45°; SP, spectrometer; DA, diode-array detection system.

4. Results and discussion

In this chapter the results of the investigated electroluminescent organic materials are elaborated which have been obtained using the experimental techniques described in chapter 3.

4.1 Dicarbazovinylene-MEH-Benzene Dye (2CzV-MEH-B)

Carbazole based polymers are applied as hole transport materials in xerographic industry and in organic light emitting diodes (OLEDs) [Rom96]. MEH-Benzene based polymers [Hol02] have shown laser action in neat thin films. The studied dye dicarbazovinylene-MEH-Benzene is a model compound for carbazovineylene and MEH-Benzene based polymers. It is a commercially available electroluminescent organic material by the name ADS084BE from American Dye Source, Inc. It has been used as light emitting oligomer in organic light emitting devices (OLEDs). It is abbreviated by 2CzV-MEH-B because of the two carbazovinylene cap-groups and the central MEH-benzene (or phenylene) part.

The oligomeric compound is studied in tetraydrofuran (THF) and as a thin film on a glass substrate. Absorption cross-section spectra, stimulated emission cross-section spectra, fluorescence quantum distributions, fluorescence quantum yields, degrees of fluorescence polarisation, and fluorescence lifetimes are determined. The saturable absorption of the dye at 347.15 nm (second harmonic of picosecond ruby laser) is measured and analysed. The amplification of spontaneous emission (wave-guided travelling-wave lasing) in neat films and the dye solution low-Q lasing in a cell (cell windows act as low reflectivity resonator mirrors) are studied by transverse sample pumping. The distributed-feedback lasing of the dye spin-coated on corrugated gratings etched into a quartz glass is investigated. The low-Q-lasing onset is analysed to extract the excited-state absorption cross-section spectrum of the dye in the fluorescence spectral region.

4.1.1 Optical and spectroscopic characterization

The transmittance spectrum and the reflectance spectrum of a 2CzV-MEH-B thin film on a fused silica substrate are shown in Fig. 4.1. The film was prepared by spin-coating, as explained in section 3.2, of a 2CzV-MEH-B/THF solution of dye concentration 15 mg/ml with a speed of 1500 rpm. The dashed curves in Fig 4.1 show the reflectance and transmittance curves of the fused silica substrate. A Fresnel equation analysis of the reflectance and transmittance curves allows to determine the absorption coefficient spectrum, $\alpha(\lambda)$, the refractive index spectrum, $n(\lambda)$, and thickness, d_f, of the neat film on transparent substrates [Pen98, Hol99a]. The film thickness is found to be d_f = 122 nm (for this value a smooth refractive index spectrum in the absorption region is obtained). The determined absorption coefficient spectrum, $\alpha(\lambda)$, and the refractive index spectrum, $n(\lambda)$, are displayed in Fig. 4.2. The refractive index dispersion of fused silica is also included in the figure (dashed curve). The absorption maximum occurs at 414 nm. At this wavelength the light penetration depth is $d_p = \alpha_P^{-1}$ = 57 nm. The refractive index spectrum shows the expected dispersion shape. In the displayed wavelength range the film refractive index is larger than the fused silica or the optical glass refractive index. Therefore the optical wave-guiding takes place in films above a critical film thickness [Kog79].

For transversal electric modes (TE modes, electrical field vector in plane of the film) the minimum film thickness is [Kog79]

$$d_{\min,TE} = \frac{\lambda}{2\pi\left(n_f^2 - n_s^2\right)^{1/2}} \arctan\left[\left(\frac{n_s^2 - n_c^2}{n_f^2 - n_s^2}\right)^{1/2}\right], \tag{4.1a}$$

and for transversal magnetic films (TM modes, magnetic field vector in plane of the film) it is

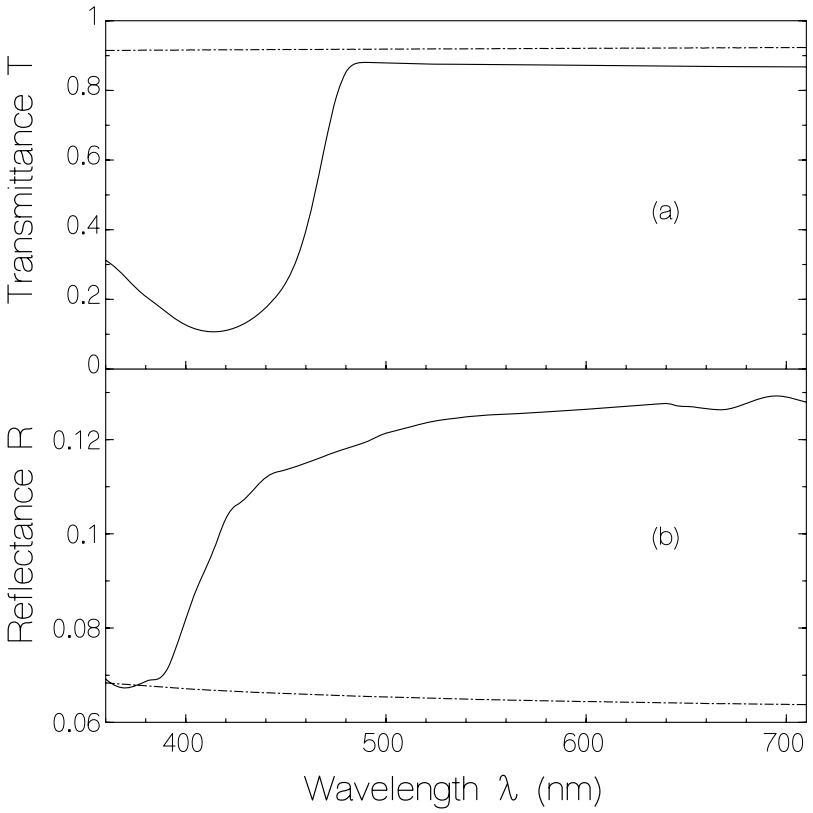

Fig. 4.1: (a) Transmittance, $T(\lambda)$, and (b) reflectance, $R(\lambda)$, spectra of an 2CzV-MEH-B film on fused silica substrate. Film thickness d_f = 122 nm. Dash-dotted lines belong to blank fused silica.

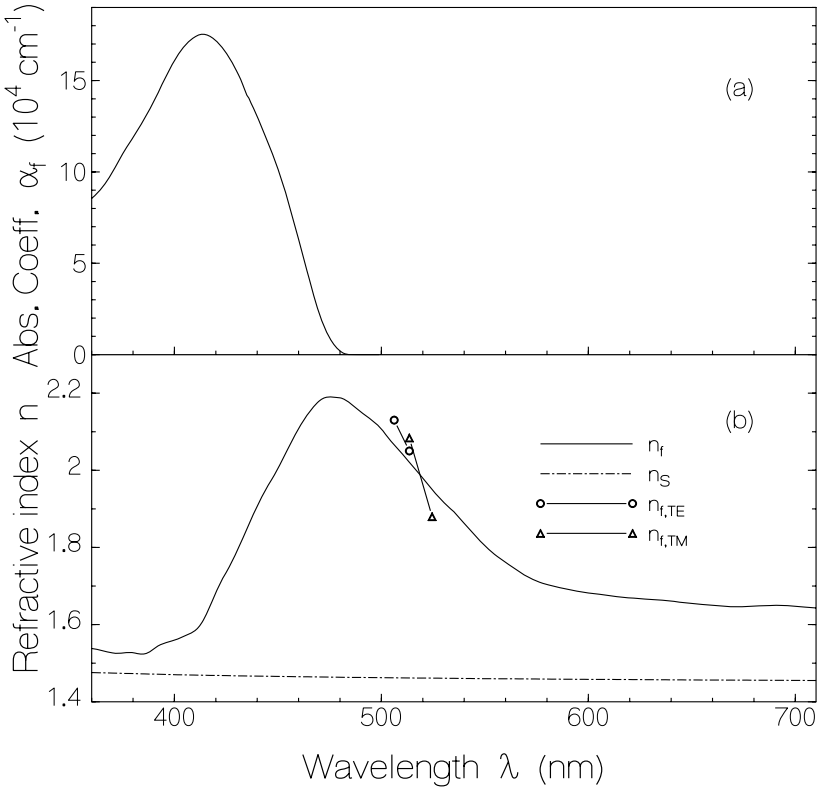

Fig. 4.2: (a) Absorption coefficient spectrum, $\alpha_f(\lambda)$, and (b) refractive index, $n(\lambda)$, spectra of 2CzV-MEH-B film and fused silica substrate. Results of distributed feedback laser analysis on the TE mode refractive index, $n_{f,TE}$, and the TM mode refractive index, $n_{f,TM}$, are included.

$$d_{\min,TM} = \frac{\lambda}{2\pi\left(n_f^2 - n_s^2\right)^{1/2}} \arctan\left[\frac{n_f^4}{n_c^4}\left(\frac{n_s^2 - n_c^2}{n_f^2 - n_s^2}\right)^{1/2}\right]. \tag{4.1b}$$

λ is the considered wavelength in vacuum, n_f, n_s, and n_c are the refractive indices of the film, the substrate, and the surrounding air ($n_c = 1$) at λ, respectively.

The absorption cross-section spectra, $\sigma_a(\lambda)$, of 2CzV-MEH-B in THF and of 2CzV-MEH-B neat film are displayed in Fig. 4.3 (the neat film curve is calculated assuming the same S_0-S_1 absorption cross-section integral for the solution and the film, Eq. 3.3). The absorption cross-section spectra of the film and the solution are similar, only the solution absorption maximum is approximately 5 nm blue-shifted compared to the film absorption maximum. The 2CzV-MEH-B molecule number density in the film is estimated to be $N_f = \alpha_f / \sigma_{a,f} \approx 8.51\times10^{20}$ cm^{-3} (calculated at λ = 416 nm). The mass density, ρ, of the 2CzV-MEH-B neat thin film is determined to be $\rho = \left(N_f / N_A\right)M_m \approx 0.954$ g cm^{-3}, where N_A is the Avogadro constant and M_m is the molar mass.

The stimulated emission cross-section spectra, $\sigma_{em}(\lambda)$, of the solution and the neat film are included in Fig. 4.3. They are calculated from the S_0-S_1 absorption spectra and the fluorescence quantum distributions (see Fig. 4.4a) using the Strickler-Berg formula [Str62, Bir63].

$$\tau_{rad,SB} = \left[\frac{8\pi c_0 n_F^3}{n_A}\frac{\int_{em} E_F(\lambda)d\lambda}{\int_{em} E_F(\lambda)\lambda^3 d\lambda}\int_{abs}\frac{\sigma_a(\lambda)}{\lambda}d\lambda\right]^{-1} \tag{4.2}$$

and the Einstein relation [Str62, Bir63]

$$\sigma_{em}(\lambda) = \frac{\lambda^4}{8\pi n_F^2 c_0 \tau_{rad,SB}}\frac{E_F(\lambda)}{\int_{em} E_F(\lambda')d\lambda'} \tag{4.3}$$

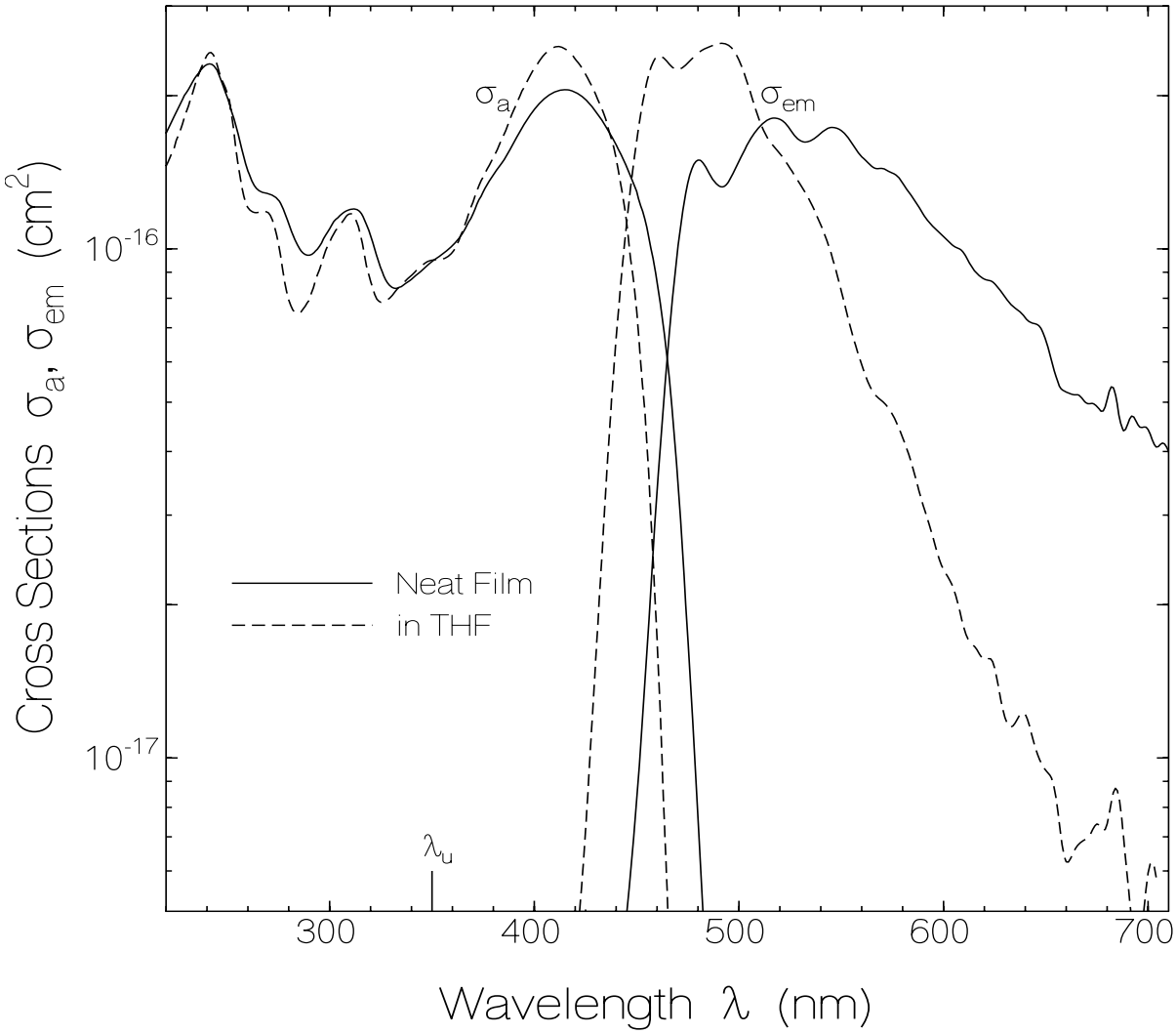

Fig. 4.3: Absorption cross-section, $\sigma_a(\lambda)$, and stimulated emission cross-section, $\sigma_{em}(\lambda)$, spectra of 2CzV-MEH-B thin film (solid curves) and of 2CzV-MEH-B dissolved in tetrahydrofuran (THF) (dashed curves, concentration 7.1×10^{-5}mol dm^{-3}).

In Eqs. 4.2 and 4.3 the integrals extend over the regions of $S_1 \rightarrow S_0$ emission (*em*) and $S_0 \rightarrow S_1$ absorption (*abs*, border λ_u is indicated in Fig. 4.3). n_F and n_A are the average refractive indices in the S_0-S_1 fluorescence and absorption region, respectively. c_0 is the velocity of light in vacuum. $\tau_{rad,SB}$ is the theoretical radiative lifetime determined by use of Eq. 4.2. The shapes of the stimulated emission cross-section spectra of 2CzV-MEH-B in solution and of 2CzV-MEH-B neat

film resolve a vibronic structure. The neat film spectrum is about 25 nm red-shifted compared to the solution spectrum, and the spectral half-width of the neat-film stimulated emission cross-section spectrum is considerably broader than that of the solution [$\Delta\tilde{\nu}_{em}$(film) ≈ 5060 cm^{-1}, $\Delta\tilde{\nu}_{em}$(solution) ≈ 3680 cm^{-1} (FWHM)].

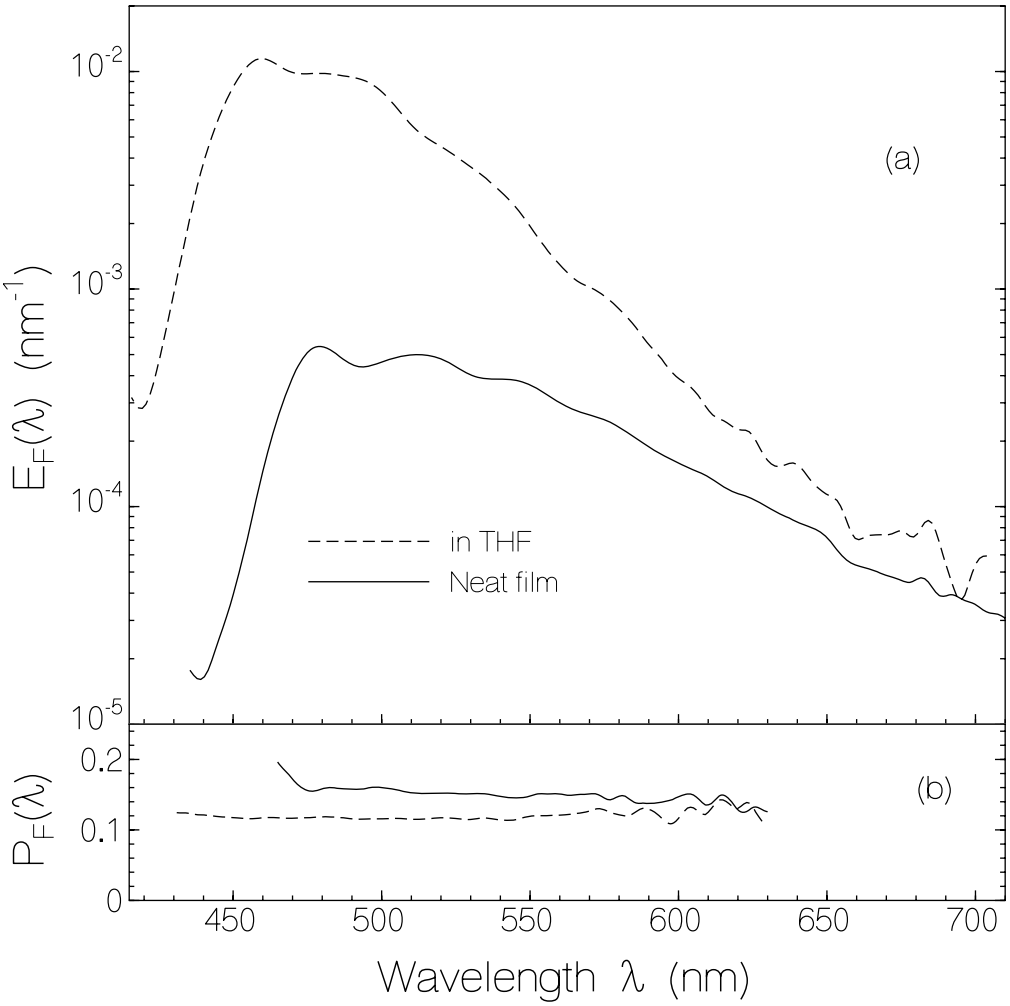

Fig. 4.4: (a) Fluorescence quantum distributions, $E_F(\lambda)$, and (b) degrees of fluorescence polarization, $P_F(\lambda)$, of solid curves, (film thickness 122 nm) and of 2CzV-MEH-B in THF (dashed curves, concentration 6.695 × 10^{-5}mol dm^{-3}).

The fluorescence quantum distributions, E_F (λ), of 2CzV-MEH-B in THF and of 2CzV-MEH-B neat film are shown in the Fig. 4.4a. The fluorescence quantum yield, $\phi_F = \int E_F(\lambda)d\lambda$,

(Eq. 3.5) of the solution is ϕ_F = 0.86±0.02 and of the film is ϕ_F = 0.062±0.003 and are also displayed in Table 4.1 The fluorescence in the solution is high, but in the film it is strongly reduced (self-quenching). The fluorescence peak of the solution occurs at 459 nm, while the fluorescence peak of the film occurs at 480 nm.

The degrees of fluorescence polarisation, P_F, of 2CzV-MEH-B in THF and of 2CzV-MEH-B neat film are shown in the Fig. 4.4b. In the solution it is $P_F \approx 0.12$, and in the neat film it is $P_F \approx 0.16$. The P_F values are also listed in Table 4.1. For isotropic media with parallel orientation of the absorption and emission transition dipole moments, P_F approaches 0.5 if there occurs no reorientation within the fluorescence lifetime (high viscosity and low concentration); and P_F approaches 0 if complete reorientation occurs within the fluorescence lifetime (either low viscosity for molecular reorientation, or high concentration for reorientation by site-to-site excitation transfer) [Lak83]. In the solution the obtained degree of fluorescence polarization is determined by molecular reorientation, while in the neat film it is determined by site-to-site excitation transfer.

The degree of fluorescence polarisation, P_F, is related to the reorientation time, τ_{or}, of the transition dipole moments by [Amm95, Lak83]

$$\tau_{or} = \frac{1/P_{F,0} - 1/3}{1 - P_F / P_{F,0}} P_F \tau_F \,, \tag{4.4}$$

where $P_{F,0}$ = 0.5, and τ_F is the fluorescence lifetime. For 2CzV-MEH-B in THF it is $P_F \approx 0.12$ and τ_F = 1.5 ns giving $\tau_{or} \approx 375$ ps. The 2CzV-MEH-B thin film has a $P_F \approx 0.16$ and $\tau_{F,av} \approx 60$ ps giving $\tau_{or} \approx 26$ ps. This short reorientation time is caused by fast excitation transfer in the random oriented molecules in the neat film (dipolar Förster-type energy transfer [För51, Val02] and Dexter-type exchange transfer [Val02, Dex53]).

The temporal fluorescence signals of a 4×10^{-5} molar solution of 2CzV-MEH-B in THF (solid line in part (a)) and of a 2CzV-MEH-B neat film (thickness 122 nm, solid line in part (b)) are shown in Fig. 4.5. The dotted curves show the detection system response functions (attenuated pump pulses directed to micro-channel plate photomultiplier or streak-camera). A single-exponential fluorescence-decay is observed for the dye in solution with a fluorescence lifetime of τ_F = 1.5 ns. The fluorescence decay fits well for the neat film to a two-exponential fluorescence decay according to $S_F(t) = S_{F,0}[x_1 \exp(-t/\tau_{F,1}) + (1-x_1)\exp(-t/\tau_{F,2})]$ with x_1 = 0.72, and

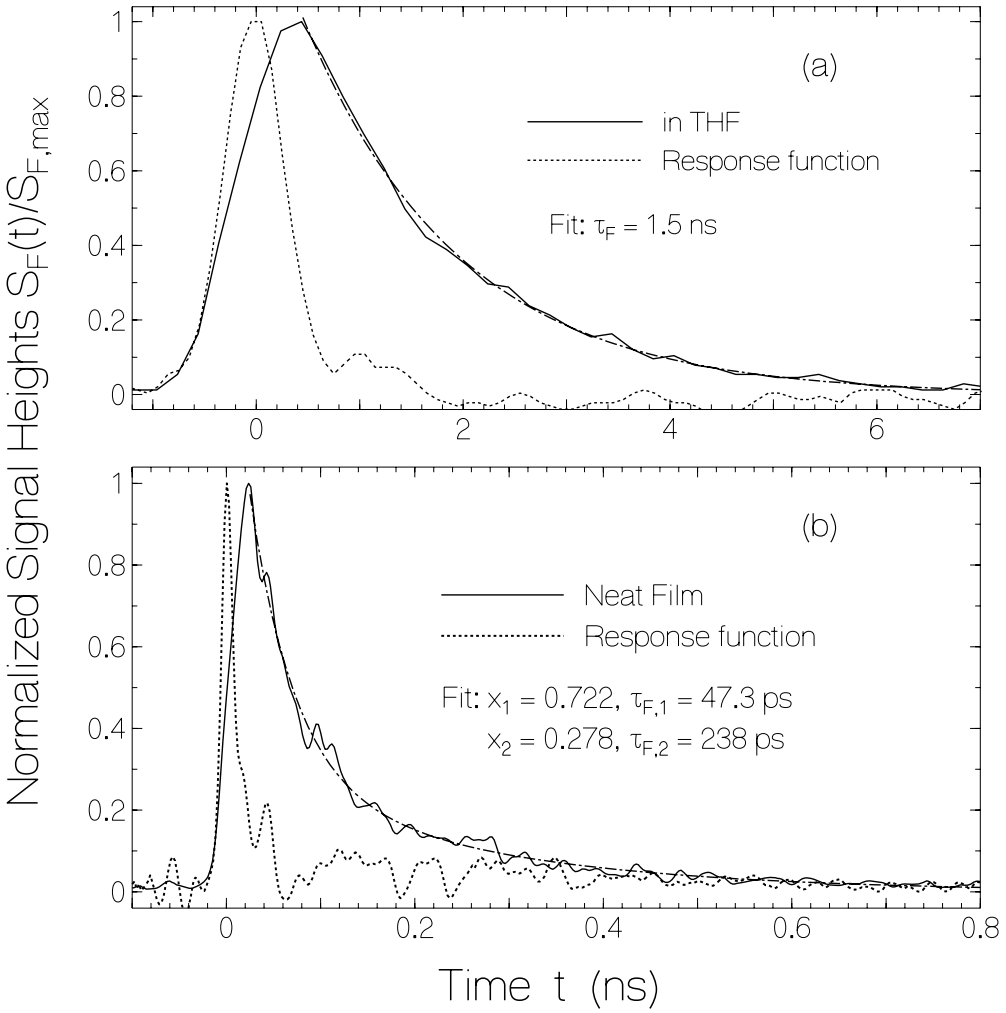

Fig. 4.5: Temporal fluorescence traces of 2CzV-MEH-B in THF (a) measured with micro-channel-plate photomultiplier neat film (concentration 3.9×10^{-5} mol dm^{-3}) and of 2CzV-MEH-B neat film (b) measured with streak-camera (film thickness 122 nm). Dotted curves show response functions.

$\tau_{F,1}$ = 47.3 ps, x_2 = 0.28, $\tau_{F,2}$ = 238 ps. The average fluorescence lifetime, defined as $1/\tau_{F,av} = x_1/\tau_{F,1} + x_2/\tau_{F,2}$, is found to be 60 ps. The fluorescence self-quenching seems to be distance and orientation dependent causing the non-single-exponential decay. The self-quenching is thought to be caused by reductive electron transfer (HOMO level of excited molecule is filled by electron from neighbour molecule), oxidative electron transfer (electron in LUMO level of excited molecule moves to LUMO level of a neighbouring unexcited molecule), and charge recombination [Val02, Bal01, Shi07].

The radiative lifetime determined from the fluorescence lifetime, $\tau_{F,av}$, and the fluorescence quantum yield, ϕ_F, is

$$\tau_{rad} = \frac{\tau_{F,av}}{\phi_F}. \tag{4.5}$$

The experimental results are τ_{rad}(solution) ≈ 1.74 ns and τ_{rad}(neat film) ≈ 0.97 ns. The radiative lifetime in the neat film is shorter than in the solution because of the higher refractive index of the neat film (Eq. 4.2: $\tau_{rad} \propto n_A n_F^{-3}$). The calculated monomeric radiative lifetimes, $\tau_{rad,SB}$, determined by use of the Strickler-Berg formula (Eq. 4.2) give $\tau_{rad,SB}$(solution) ≈ 1.74 ns and $\tau_{rad,SB}$(neat film) ≈ 1.22 ns. In liquid solution the experimental radiative lifetime, τ_{rad}, and the calculated monomeric Strickler-Berg radiative lifetime, $\tau_{rad,SB}$ (σ_a is the absorption cross-section per molecule) give the same value within our experimental accuracy, i.e. the emitting chromophore size and the molecule size are the same [Pet71]. This result is expected for diluted solutions (no dimers or higher aggregates present). The determined neat film radiative lifetime, τ_{rad}, is found to be slighter shorter than the calculated monomeric radiative lifetime, $\tau_{rad,SB}$, indicating some partial delocalisation of the excited-state wavefunction over adjacent molecules [Hol01]. The

average wavefunction delocalisation factor is $m_{del} = \tau_{rad,SB} / \tau_{rad} \approx 1.26$. This indicates that in the neat film, in about one quarter of cases the emitting chromophore consists of two adjacent molecules (wavefunction of emitting state extends over two monomeric units).

4.1.2 Saturable absorption behaviour

The experimental energy transmission, T_E, of second harmonic picosecond ruby laser pulses (duration $\Delta t_P = 35$ ps, wavelength $\lambda_P = 347.15$ nm) through a 1 mm cell filled with 2CzV-MEH-B in THF as a function of the input peak pulse intensity, I_{0P}, is shown by the circles in Fig. 4.6. The transmission rises from the small-signal transmission of $T_0 = 0.073$ at low excitation intensity to $T_E \approx 0.3$ at excitation intensity $I_{0P} = 2\times10^{10}$ W cm^{-2}. The applied energy level system for the saturable absorption simulations is shown in Fig. 2.7 in chapter 2. The pump laser excites the dye molecules from the S_0 ground-state 1 to a Franck-Condon level 2' in the S_1 band. From there the molecules relax to a thermalized level 2 with the Franck-Condon relaxation time constant, τ_{FC} ($\tau_{FC} = 0.5$ ps is used in the simulations [Pen76]). From the S_1 band excited-state absorption occurs to a higher lying singlet band S_n (level 3). The higher excited chromophores relax quickly back to the S_1 band with a time constant, τ_{ex} ($\tau_{ex} = 60$ fs is used in the simulations [Gra85]). The absorption anisotropy of the electric dipole interaction due to the orientation, θ, of the transition dipole moments relative to the polarization of the excitation pulses, and the reorientation of the transition dipole moments (time constants τ_{or}) are included in the analysis [Pen78].

The differential equation system for the determination of the intensity dependent pump pulse transmission [Hol00b] is:

$$\frac{\partial N_1}{\partial t'} = -\frac{3\sigma_{a,P}\cos^2(\theta)}{h\nu_P}(N_1 - N_{2'})I_P + \frac{N_2 + N_{2'}}{\tau_{S_1}} - \frac{N_1 - \overline{N}_1}{\tau_{or}}, \tag{4.6}$$

$$\frac{\partial N_{2'}}{\partial t'} = \frac{3\sigma_{a,P}\cos^2(\theta)}{h\nu_P}(N_1 - N_{2'})I_P - \frac{N_{2'} - N_{2',th}}{\tau_{FC}} - \frac{N_{2'}}{\tau_{S_1}} - \frac{3\sigma_{ex,P}\cos^2(\theta)}{h\nu_P}\left(N_{2'} - \frac{N_{2'}}{N_2 + N_{2'}}N_3\right)I_P - \frac{N_{2'} - \overline{N}_{2'}}{\tau_{or}}, \tag{4.7}$$

$$\frac{\partial N_2}{\partial t'} = \frac{N_{2'} - N_{2',th}}{\tau_{FC}} - \frac{3\sigma_{ex,P}\cos^2(\theta)}{h\nu_P}\left(N_2 - \frac{N_2}{N_2 + N_{2'}}N_3\right)I_P - \frac{N_2}{\tau_{S_1}} + \frac{N_3}{\tau_{ex}} - \frac{N_2 - \overline{N}_2}{\tau_{or}}, \tag{4.8}$$

$$\frac{\partial N_3}{\partial t'} = \frac{3\sigma_{ex,L}\cos^2(\theta)}{h\nu_P}(N_2 + N_{2'} - N_3)I_P - \frac{N_3}{\tau_{ex}} - \frac{N_3 - \overline{N}_3}{\tau_{or}}, \tag{4.9}$$

$$\frac{\partial I_P}{\partial z'} = -3\sigma_{a,P}I_P\int_0^{\pi/2}(N_1 - N_{2'})\cos^2(\theta)\sin(\theta)\,d\theta - 3\sigma_{ex,P}I_P\int_0^{\pi/2}(N_2 + N_{2'} - N_3)\cos^2(\theta)\sin(\theta)\,d\theta \tag{4.10}$$

$$\overline{N}_i = \int_0^{\pi/2} N_i(\theta)\sin(\theta)\,d\theta, \qquad i = 1, 2, 2', 3 \tag{4.11}$$

$$N_{2',th} = (N_2 + N_{2'})\exp\left(-\frac{h\nu_{2,2'}}{k_B\vartheta}\right). \tag{4.12}$$

where $N_i(r, z', t', \theta)$, $i = 1-3$, are the level population number densities. The moving frame transformation $t' = t - nz/c_0$ and $z' = z$ is used, where t is the time, z is the propagation coordinate, n is the refractive index, and c_0 is the velocity of light in vacuum. θ is the angle between the molecular transition dipole moment and the polarization direction of the pump laser [Feo64]. $\overline{N}_i$ is the orientation averaged population of level I. $N_{2',th}$ is the thermal population of level $2'$. $h\nu_{2,2'} = hc_0\tilde{\nu}_{2,2'}$ is the energy difference between level 2 and $2'$. k_B is the Boltzmann constant, and ϑ is the temperature.

The initial conditions are $N_1(r, t' = -\infty, z', \theta) = N_0 = CN_A$, $N_2(r, t' = -\infty, z', \theta) = N_3(r, t' = -\infty, z', \theta) = 0$ and $I_P(r, t', z' = 0) = I_{0P}\exp(-r^2/r_P^2)\exp(-t'^2/t_P^2)$.

N_0 is the total dye number density, C is the dye concentration, and N_A is the Avogadro constant. r is the radial coordinate; r_P and t_P are the 1/e-intensity pump beam radius and the pump pulse duration, respectively.

The pump pulse energy transmission is

$$T_E = \frac{\int_0^\infty r dr \int_{-\infty}^{\infty} I_P(r,l,t')dt'}{\int_0^\infty r dr \int_{-\infty}^{\infty} I_P(r,0,t')dt'} \tag{4.13}$$

where l is the sample length.

The solid curves in Fig. 4.6 are numerical fit simulations to the transmission measurements. The excited-state absorption cross-section is varied. The best fit to the experimental data is obtained for $\sigma_{ex,P} = 4\times10^{-17}$ cm^2. The ground-state absorption cross-section is $\sigma_{a,P} = 9.4\times10^{-17}$ cm^2.

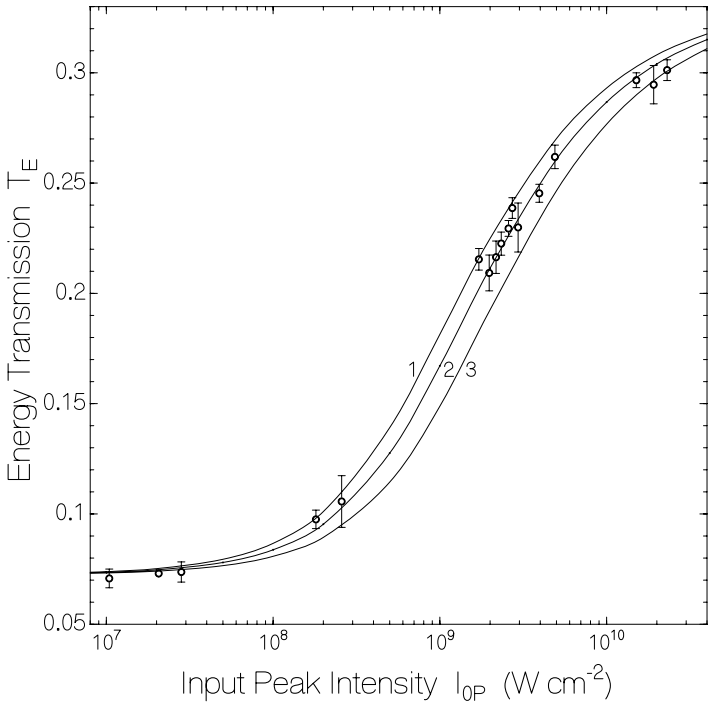

Fig. 4.6: Saturable absorption behaviour of 2CzV-MEH-B in THF. Circles are measured. Curves are calculated using excited-sate absorption cross-sections $\sigma_{ex} = 3 \times 10^{-17}$ cm^2 (1), 4×10^{-17} cm^2 (2), and 5×10^{-17} cm^2 (3).

Table 4.1: Optical and spectroscopic parameters of 2CzV-MEH-B (light emitting oligomer ADS084BE)

Parameter	2CzV-MEH-B in THF	2CzV-MEH-B neat film	Comments
$\lambda_{a,max}$ (nm)	410	414	Fig. 4.3
$\lambda_{em,max}$ (nm)	492	516	Fig. 4.3
$\lambda_{F,max}$ (nm)	459	480	Fig. 4.4
n_A	1.4178 [Hel62]	1.68	for film: Fig. 4.2b
n_F	1.4105 [Hel62]	1.93	for film: Fig. 4.2b
ϕ_F	0.86	0.062	Fig. 4.4
P_F	0.12	0.16	Fig. 4.4
$\tau_{F,av}$ (ns)	1.5	0.06	Fig. 4.5
τ_{rad} (ns)	1.74	0.97	Eq. 4.5
$\tau_{rad,SB}$ (ns)	1.74	1.22	Eq. 4.2
τ_{or} (ps)	375	26	Eq. 4.4

Abbreviations: $\lambda_{a,max}$: wavelength of peak absorption of first absorption band. $\lambda_{em,max}$: wavelength of peak stimulated emission cross-section. $\lambda_{F,max}$: wavelength of fluorescence maximum. n_F: average refractive index in fluorescence region. ϕ_F: fluorescence quantum yield. P_F: degree of fluorescence polarisation. τ_F: fluorescence lifetime. τ_{rad}: radiative lifetime. τ_{or}: transition dipole moment reorientation time.

4.1.3 Laser performance

The transverse pumped lasing of 2CzV-MEH-B/THF in a 1 cm × 1 mm dye-laser cell, the wave-guided travelling-wave lasing (amplification of spontaneous emission) of neat thin films of 2CzV-MEH-B on microscope carrier plates, and the distributed-feedback laser action of neat thin films of 2CzV-MEH-B on corrugated Bragg gratings etched into a fused silica plate are studied.

4.1.3.1 Transverse pumped low-Q laser

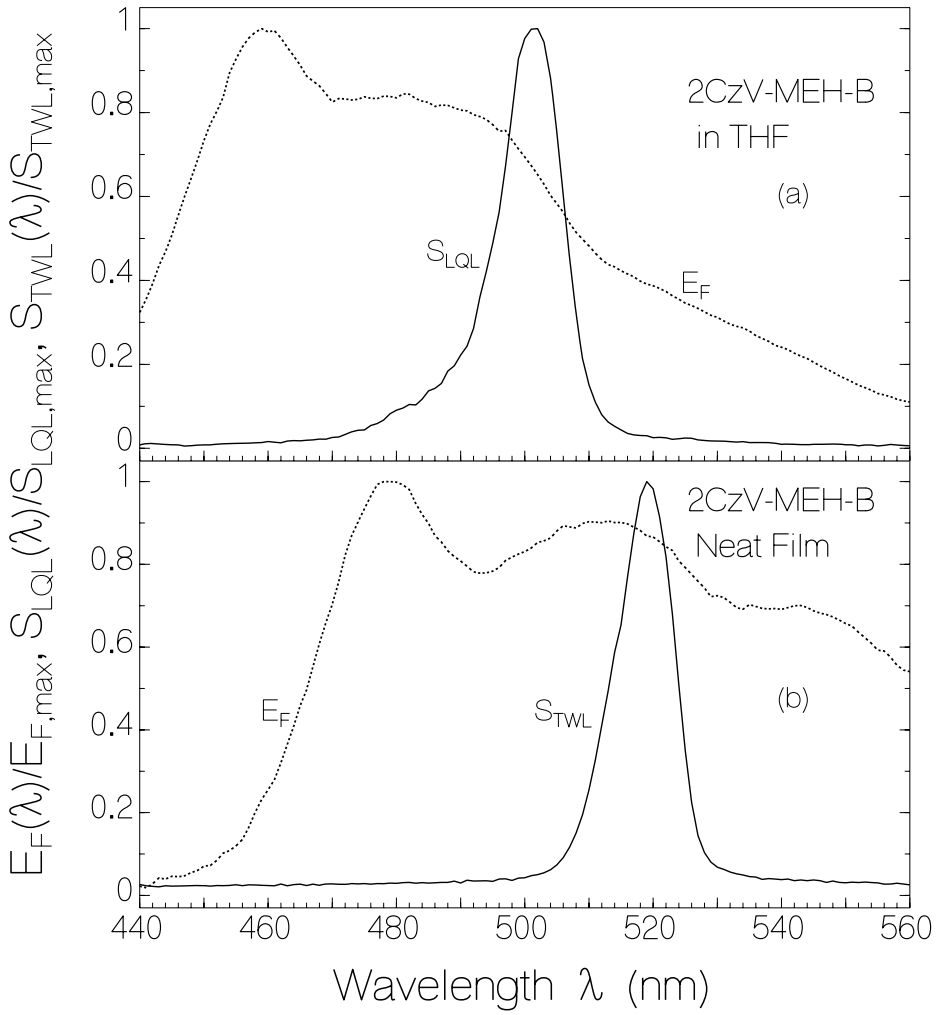

Fig. 4.7: Spectral shapes of (a) low-Q laser emission, $S_{LQL}(\lambda)/S_{LQL,max}$ of 2CzV-MEH-B in THF (concentration 4.46×10^{-4} mol dm^{-3}, excitation energy density $w_{0P} = 7.66\times10^{-4}$ J cm^{-2}).
(b) Travelling-wave laser emission, $S_{TWL}(\lambda)/S_{TWL,max}$, of 2CzV-MEH-B neat film (thickness 90 nm, $w_{0P} = 4.0\times10^{-4}$ J cm^{-2}). For comparison the normalized fluorescence quantum distributions, $E_F(\lambda)/E_{F,max}$, are also displayed.

The dye 2CzV-MEH-B in THF with concentration 4.46×10^{-4} molar solution (dye number density $N_0 = 2.69 \times 10^{17}$ cm^{-3}) was studied in a dye-laser cell of ℓ_s = 1 cm length and d = 1 mm length and was transverse pumped with line-focused picosecond second-harmonic pulses of the ruby laser system (pump beam cross-section 14.5 mm × 0.245 mm). The dye cell itself formed the optical laser resonator (low-Q resonator): the end surfaces of the cell acted as mirrors (reflectance $R = (n-1)^2/(n+1)^2 = 0.03527$, n = 1.4624 is refractive index of cell glass at 500 nm).

In Fig. 4.7a the output spectrum of the low-Q laser, $S_{LQL}(\lambda)$, is shown. It belongs to an excitation pulse energy density of $w_{0P} = 7.66 \times 10^{-4}$ J cm^{-2} The emission maximum is at $\lambda_{LQL,max}$ = 501 nm. It coincides with the wavelength position of peak stimulated emission cross-section which occurs at 492 nm (see Fig. 4.3). The laser line-width is $\Delta\lambda_{LQL} \approx 11.5$ nm (FWHM) at the applied excitation pulse energy.

The dependences of the laser output energy, W_{LQL}, of the laser wavelength peak position, $\lambda_{LQL,max}$, and of the spectral halfwidth (FWHM), $\Delta\lambda_{LQL}$, on the peak input pump laser energy density, w_{0P}, are displayed in Fig. 4.8a, b, and c, respectively. In Fig. 4.8a, above a certain threshold pump pulse energy density, $w_{0P,th} \approx 0.6$ mJ cm^{-2}, the emission begins to rise beyond the spontaneous emission and amplified spontaneous emission level due to low-Q laser oscillation action. In Fig. 4.8b it is seen, that the wavelength position of light emission below laser oscillator threshold is at about 490 nm, and above laser threshold is at about 500 nm. The peak position of the stimulated emission cross-section is at about 492 nm. The red-shift of peak laser emission is caused by the S_1-state excited-state absorption cross-section spectral distribution (peak of effective stimulated emission cross-section, $\sigma_{em,eff}(\lambda) = \sigma_{em}(\lambda) - \sigma_{ex}(\lambda)$, occur at ≈ 500 nm). In Fig. 4.8c it is seen that the spectral halfwidth, $\Delta\lambda_{LQL}$, of the light emission shrinks down from

about 55 nm before laser action ($w_{0P} < w_{0P,th}$) to about 12 nm at laser threshold and rises slightly with rising excess pump pulse energy density due to gain saturation (excited state population depletion) combined with inhomogeneous broadening [Hol04a].

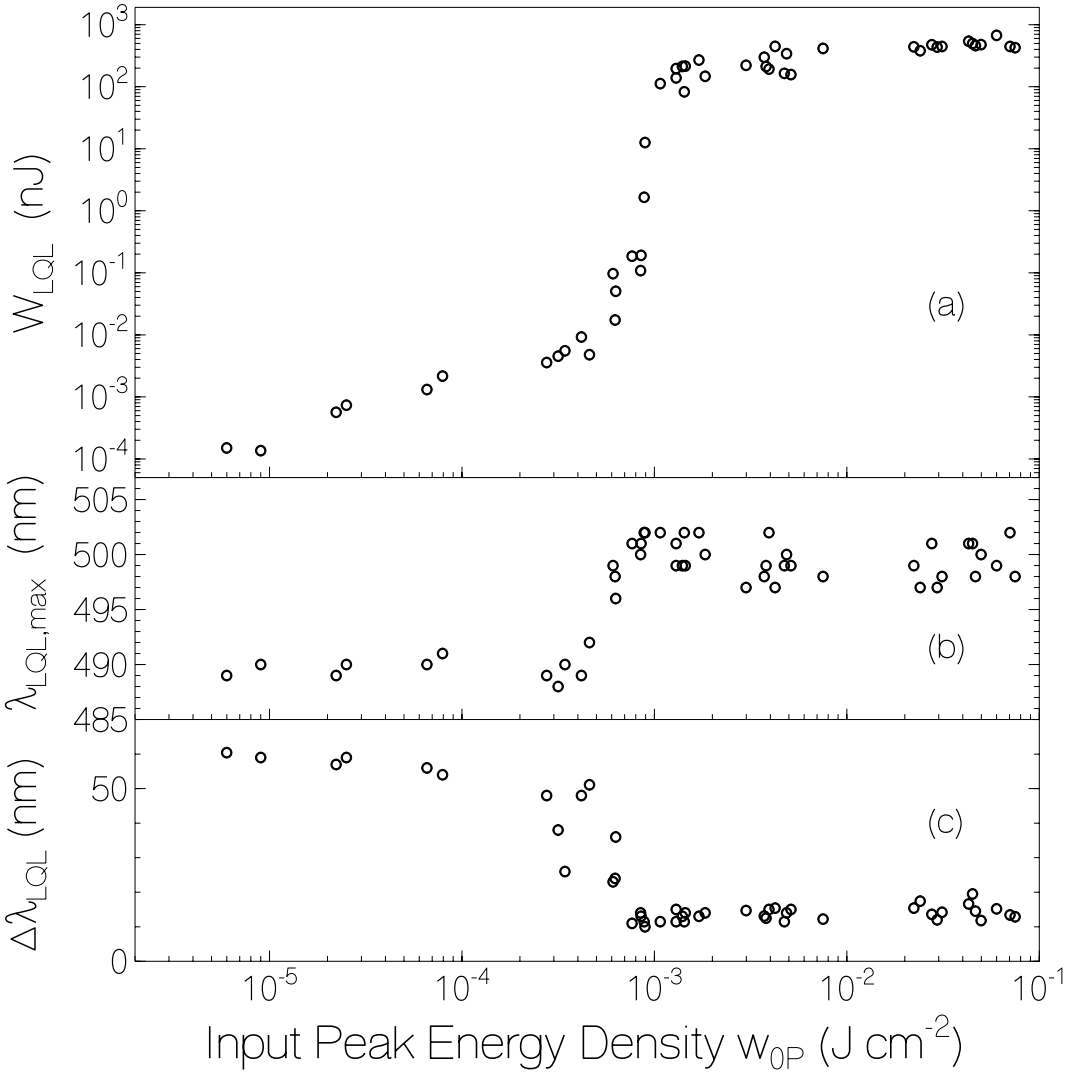

Fig. 4.8: Low-Q laser oscillator performance of 2CzV-MEH-B/THF in a dye-laser cell. Dye concentration $C_0 = 4.46 \times 10^{-4}$ mol dm^{-3}.
(a) Collected emission signal, W_{LQL}, versus input pump pulse energy density, w_{0P}. Full acceptance angle of fluorescence collection is $\Delta\theta = 0.83^\circ$. Pump laser threshold energy density $w_{0P,th} \approx 609$ µJ cm^{-2}.
(b) Peak wavelength of low-Q laser oscillator, $\lambda_{LQL,max}$, versus input pump pulse energy density, w_{0P}.
(c) Spectral line-width (FWHM) of low-Q laser oscillator, $\Delta\lambda_{LQL}$, versus input pump-pulse energy density, w_{0P}.

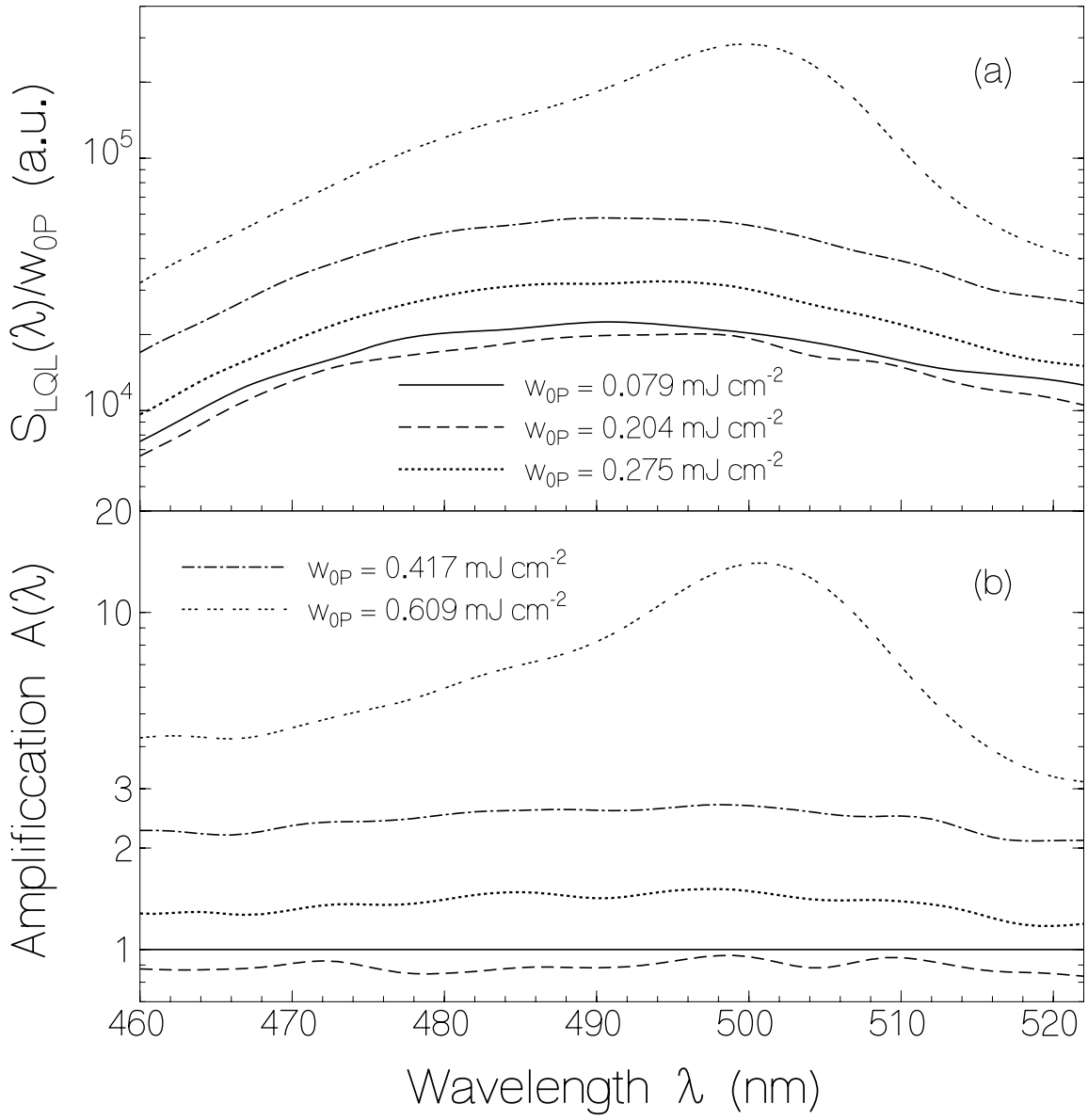

Fig.4.9: Spectral lasing performance of low-Q laser oscillator.
(a) Normalized spectral low-Q laser output, $S_{LQL}(\lambda)/w_{0P}$, of picosecond-laser transversely-pumped 2CzV-MEH-B/THF in 10 mm × 1 mm dye-laser cell. Dye concentration $C_0 = 4.46\times10^{-4}$ mol dm^{-3}. Cell wall thickness $\ell_w = 1.25$ mm.
(b) Spectral fluorescence light amplification, $A(\lambda)$, for several pump laser energy densities, w_{0P}.

Low-Q laser emission spectra, $S_{LQL}(\lambda)$, normalized to the excitation pump pulse peak energy density, w_{0P}, are shown in Fig. 4.9a for various pump pulse peak energy densities. Up to $w_{0P} \approx 0.4$

mJ cm^{-2} the normalized spectra are unchanged and are determined by the spontaneous emission, $S_{sp}(\lambda)$ (normal fluorescence). At higher pump pulse energy densities the normalized spectra rise steeply in the wavelength range of maximum stimulated emission cross-section (see Fig. 4.3).

In Fig. 4.9b the amplification of the spontaneous emission, $A(\lambda)$, which is defined as

$$A(\lambda) = \frac{S_{LQL}(\lambda)/N_{ex,0}(w_{0P})}{S_{sp}(\lambda)/N_{ex,0}(w_{0P,sp})} = \frac{S_{LQL}(\lambda)\left[1-\exp\left(-\frac{w_{0P,sp}}{w_{P,sat}}\right)\right]}{S_{sp}(\lambda)\left[1-\exp\left(-\frac{w_{0P}}{w_{P,sat}}\right)\right]} \tag{4.14}$$

is displayed, where $N_{ex,0}$ is the initial emission-state population number density. It is given by

$$N_{ex,0} = N_0\left[1-\exp\left(-\frac{w_{0P}}{w_{P,sat}}\right)\right] \tag{4.15}$$

Thereby $w_{0P} = I_{0P}\,\Delta t_P$ is pump pulse peak energy density. N_0 is the total molecule number density. $w_{P,sat}$ is the saturation energy density. It is given by [Pen88]

$$w_{P,sat} = h\nu_P/\sigma_{a,P}\,, \tag{4.16}$$

$\sigma_{a,P}$ is the ground-state absorption cross-section at the pump laser frequency ν_P. Eq. 4.15 is obtained by solving the rate equation for the ground-state population number density, $N_{1,0} = N_0 - N_{ex,0}$, which reads

$$\frac{dN_{1,0}}{dt} = -\frac{\sigma_{a,P}}{h\nu_P}N_{1,0}I_{0P} = -N_{1,0}\frac{I_{0P}}{w_{P,sat}}\,, \tag{4.17a}$$

neglecting excited population recovery within the pump pulse duration (slow saturable absorption [Grö84]), and which has the solution

$$N_{1,0} = N_0\exp\left(-\frac{I_{0P}\Delta t}{w_{P,sat}}\right) = N_0\exp\left(-\frac{w_{0P}}{w_{P,sat}}\right). \tag{4.17b}$$

The second part of Eq. 4.14 is obtained by insertion of Eq. 4.15 in the first part of Eq. 4.14. For $S_{sp}(\lambda)/w_{0P,sp}$ the curve with w_{0P} = 0.079 mJ cm^{-2} from Fig. 4.9a is used. Above the laser threshold pump pulse energy density, $w_{0P} > w_{0P,th} \approx 0.6$ mJ cm^{-2} the amplification around the peak laser wavelength rises steeply. Over the whole displayed wavelength range it is $A(\lambda) > 1$ indicating that $\sigma_{em}(\lambda) > \sigma_{ex}(\lambda)$.

For vertical polarized excitation and vertical polarized emission detection, the spontaneous emission amplification, $A(\lambda)$, of the short-length low-Q laser oscillator is approximately given by

$$A(\lambda) = A_{ASE}(\lambda) + A_{LQL}(\lambda)$$

$$\approx \frac{\int_{-\infty}^{\infty} dr e^{-r^2} \int_0^d dz e^{-\alpha_p z} \int_0^{\infty} dt e^{-t/\tau_F} \exp\left[\left[(\sigma_{em}(\lambda)+\sigma_a(\lambda)) f_{em}(t) - \sigma_{ex}(\lambda) f_{ex}(t)\right] N_{ex,0} e^{-r^2-\alpha_p z - t/\tau_F} \frac{\ell_s}{2}\right]}{\int_{-\infty}^{\infty} dr \exp(-r^2) \int_0^d dz \exp(-\alpha_p z) \int_0^{\infty} dt \exp(-t/\tau_F)} (1-R)$$

$$+ \frac{\int_{-\infty}^{\infty} dr e^{-r^2} \int_0^d dz e^{-\alpha_p z} \int_0^{\infty} dt e^{-t/\tau_F} \left\{R^2 \exp\left[\left[\sigma_{em}(\lambda) f_{em}(t) - \sigma_{ex}(\lambda) f_{ex}(t)\right] N_{ex,0} e^{-r^2-\alpha_p z - t/\tau_F} 2\ell_s\right]\right\}^{t/t_{rt}}}{\int_{-\infty}^{\infty} dr \exp(-r^2) \int_0^d dz \exp(-\alpha_p z) \int_0^{\infty} dt \exp(-t/\tau_F)} (1-R)$$

(4.18)

With the resonator round-trip time

$$t_{rt} = 2\frac{n_s l_s + 2 n_w l_w}{c_0}, \tag{4.19}$$

and the orientation factors for vertical polarized excitation and vertical polarized emission detection

$$f_{em}(t) = 2\exp(-t/\tau_{or}) \exp\left(-\frac{w_{0P}}{w_{P,sat}}\right), \tag{4.20a}$$

and

$$f_{ex}(t) = \begin{cases} 2\exp(-t/\tau_{or})\exp(-w_{0P}/w_{P,sat}) + 1 & for\ \vec{\mu}_{S1-Sn} \| \vec{\mu}_{S0-S1} \\ 1 - \exp(-t/\tau_{or})\exp(-w_{0P}/w_{P,sat}) & for\ \vec{\mu}_{S1-Sn} \perp \vec{\mu}_{S0-S1} \end{cases} . \qquad (4.20b)$$

r is the coordinate perpendicular to the direction of the pump laser propagation and perpendicular to the line-focus direction of the pump laser. z is the coordinate along the pump laser propagation. ℓ_s is the amplification length of the dye solution (inner dye cell length). ℓ_w is the wall thickness of the dye cell. n_s and n_w are the refractive indices of the dye solution and of the dye cell walls, respectively. c_0 is the velocity of light in vacuum. *d* is the inner cell width. w_{0P} is the peak pump laser energy density at the dye cell entrance. α_p is the absorption coefficient of the dye solution at the pump laser wavelength $\lambda_P = c_0/\nu_P$. *R* is the reflectance of the dye cell. τ_{or} is the molecular reorientation time. $\sigma_{em}(\lambda)$ and $\sigma_{ex}(\lambda)$ are the orientation averaged stimulated emission cross-section and the orientation averaged excited-state absorption cross-section of the dye at λ. The orientation dependence of the stimulated emission cross-section is given by $\sigma_{em}(\lambda)f_{em}(t)$ [Pen76]. At time $t = 0$ the transition dipole moment $\vec{\mu}_{S1-S0}$ is parallel to the vertical polarisation of the excitation and the stimulated emission cross-section is $3\sigma_{em}(\lambda)$. For time $t >> \tau_{or}$ the stimulated emission cross-section is $\sigma_{em}(\lambda)$. The orientation dependence of the excited-state absorption cross-section is given by $\sigma_{ex}(\lambda)f_{ex}(t)$. If the transition dipole moments of S_1-S_0 emission and excited-state absorption are parallel then it is $f_{ex}(t) = 2\exp(-t/\tau_{or}) + 1$. If the transition dipole moments of S_1-S_0 emission and excited-state absorption are perpendicular to one another then it is $f_{ex}(t) = 1 - \exp(-t/\tau_{or})$. Eq. 4.18 neglects emission level depopulation due to the laser action, and is therefore only valid for moderate amplification factors (emission state depopulation given by fluorescence lifetime τ_F). The first sum term of Eq. 4.18 takes care of the amplified spontaneous emission, A_{ASE}. The effective gain length for this amplified spontaneous emission is

approximated by $\ell_s/2$. The second sum term of Eq. 4.18 describes the amplification of the fed-back light (laser oscillator), A_{LQL}.

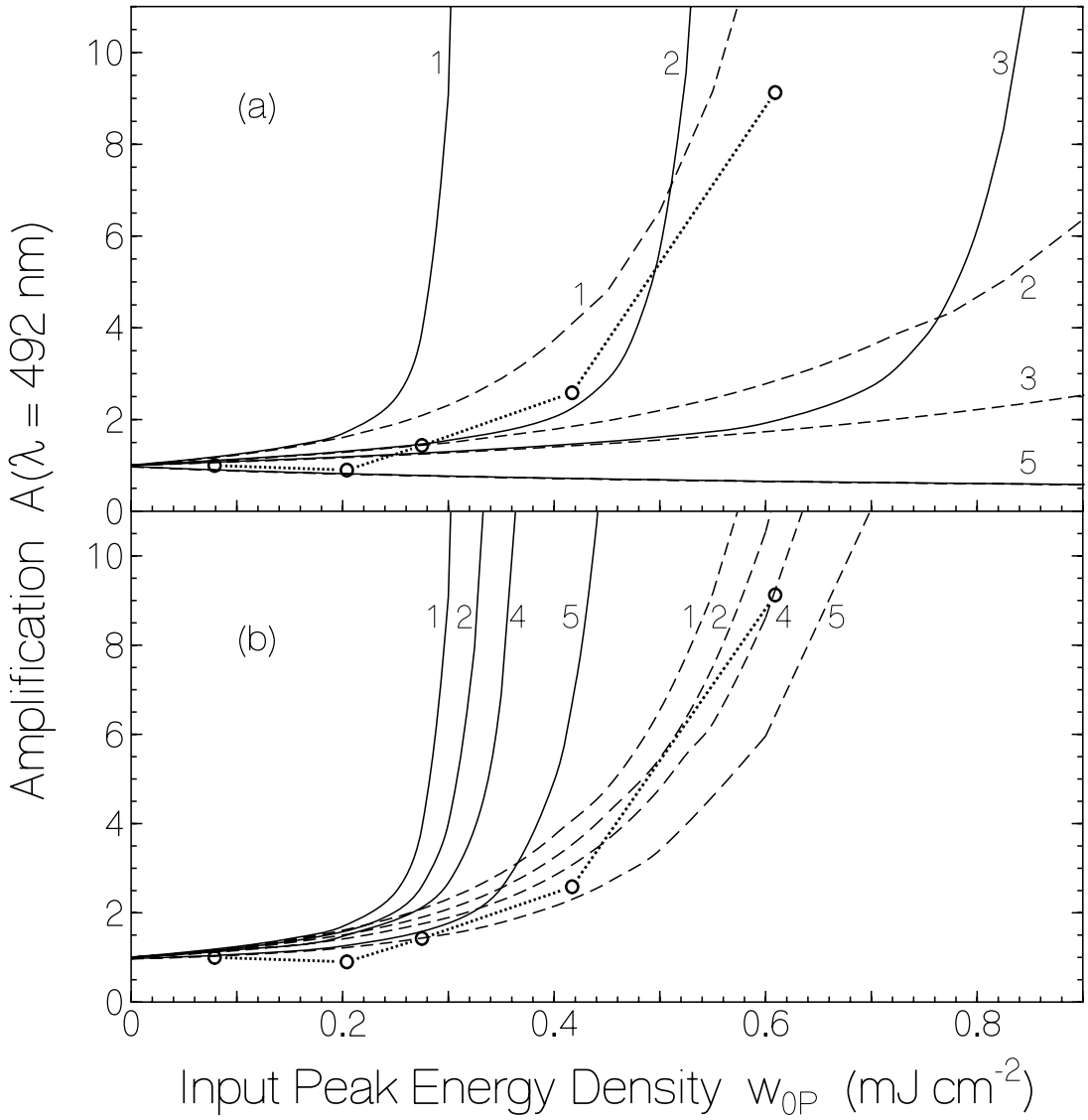

Fig. 4.10: Spectral light amplification, $A(\lambda$=492nm), versus input pump pulse peak energy density, w_{0P}. The experimental results are shown by the line-connected circles. The dashed curves are calculated amplifications due to the amplified spontaneous emission, A_{ASE} (first term of Eq. 4.18). The solid curves are calculated total amplifications, A, including amplified spontaneous emission (A_{ASE}) and low-Q laser oscillation (A_{LQL}). The top part (a) considers parallel orientation of ground-state and excited-state transition dipole moments. The bottom part (b) considers perpendicular orientation of ground-state and excited-state transition dipole moments. Experimental parameters are used in the calculations (σ_{em}(492nm) = 2.53×10^{-16} cm^2). The excited-state absorption cross-section is varied using (1) $\sigma_{ex} = 0$, (2) $\sigma_{ex} = 1\times10^{-16}$ cm^2, (3) $\sigma_{ex} = 1.5\times10^{-16}$ cm^2, (4) $\sigma_{ex} = 2\times10^{-16}$ cm^2 and (5) $\sigma_{ex} = 4\times10^{-16}$ cm^2

In Fig. 4.10a the dotted-line connected circles show the light amplification at 492 nm versus the input pump pulse energy density. The solid curves are calculated $A(\lambda)$ curves using (Eq. 4.18) the known dye laser parameters and varying the excited-state absorption cross-section, σ_{ex}(492 nm). The excited-state absorption transition dipole moment is assumed to be parallel to the ground-state absorption transition dipole moment (Eq. 4.20b). The dashed curves are calculated $A_{ASE}(\lambda)$ curves (First sum of Eq. 4.18) for the same parameters. The steep rise in amplification occurs at the laser oscillator threshold where the light amplification compensates the output losses (small reflectance R). The best fit of the calculation to the experimental data points is obtained for $\sigma_{ex}(492\text{nm}) = 1.2\times10^{-16}$ cm^2.

In Fig. 4.10b the same experimental data are shown as in Fig. 4.10a. Only the $A(\lambda)$ and $A_{ASE}(\lambda)$ curves are calculated for the situation of the excited-state absorption transition dipole moment perpendicular to the ground-state absorption transition dipole moment (Eq. 4.20b). The experimental data cannot be fitted by the theoretical curves. For times $t < \tau_{or}$ the S_1-S_n excited state transition does not couple to the induced emission since excited-state absorption cross-section for perpendicular oriented transition is zero, leading to a higher calculated amplification than experimentally observed. This indicates that for the considered transitions the transition dipole moments are not perpendicular to one another.

In Fig. 4.11 the extracted $\sigma_{em,eff}(\lambda) = \sigma_{em}(\lambda) - \sigma_{ex}(\lambda)$ and $\sigma_{ex}(\lambda)$ spectra together with the $\sigma_{em}(\lambda)$ spectrum (from Fig. 4.3) are shown for the situation of parallel orientation of the excited-state absorption and the ground-state absorption transition dipole moments.

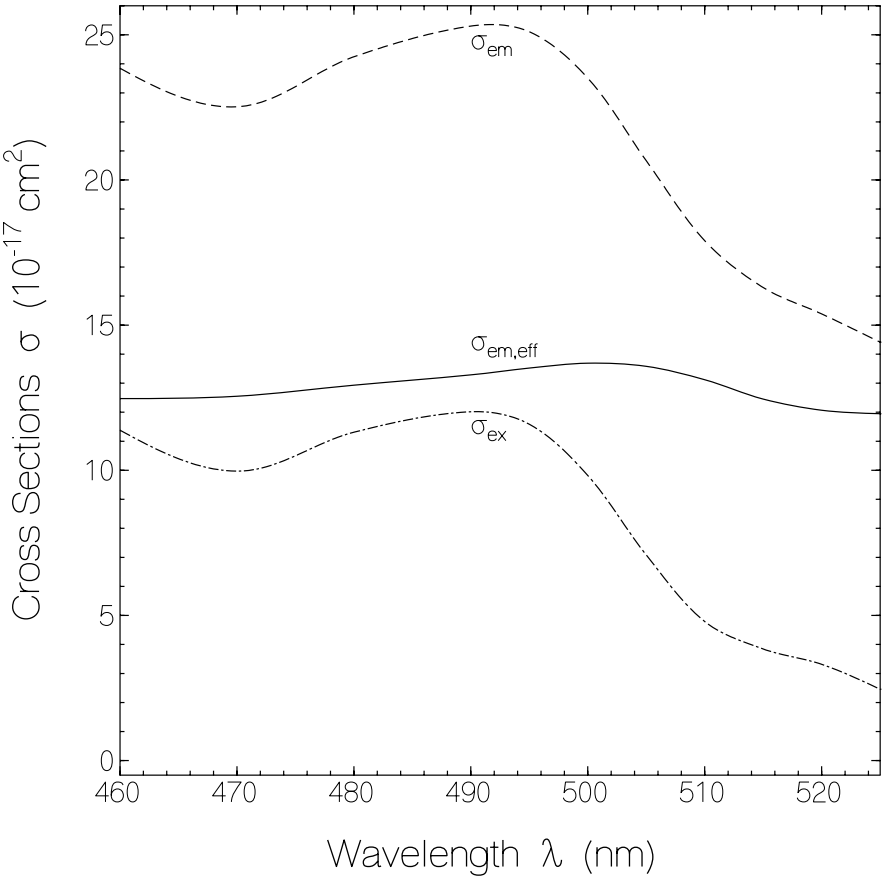

Fig. 4.11: Cross-sections of 2CzV-MEH-B in THF in lasing spectral region extracted by fit of Eq. 4.18 to the amplification $A(\lambda, w_{0P} = 0.609$ mJ cm$^{-2})$ of Fig. 4.9b. Solid curve: effective stimulated emission cross-section spectrum, $\sigma_{em,eff}(\lambda)$. Dashed curve: stimulated emission cross-section spectrum, taken from Fig. 4.3. Dash-dotted curve: excited-state absorption cross-section spectrum, $\sigma_{ex}(\lambda) = \sigma_{em}(\lambda) - \sigma_{em,eff}(\lambda)$.

At laser oscillator threshold the light amplification $V = \exp(\sigma_{em,eff,L} N_{ex,0,th} \ell_s)$ compensates the reflection losses $L = R^{-1}$. The effective stimulated emission is given by $\sigma_{em,eff,L} = \sigma_{em,L} - \sigma_{ex,L}$, where $\sigma_{em,L}$ is the stimulated emission cross-section at the peak laser wavelength, and $\sigma_{ex,L}$ is the excited-state absorption cross-section at the peak laser wavelength. There occurs no laser action if $\sigma_{ex,L} \geq \sigma_{em,L}$. The laser oscillator threshold is defined by

$$\exp\left(\sigma_{em,eff,L} N_{ex,0,th} \ell_s\right) = \exp\left[\sigma_{em,eff,L} N_0 \left[1 - \exp\left(-\frac{w_{0P,th}}{w_{P,sat}}\right)\right] \ell_s\right] = R^{-1}, \tag{4.21}$$

where $w_{0P,th}$ is the pump laser threshold energy density. Rewriting Eq. 4.21 to the effective stimulated emission cross-section gives

$$\sigma_{em,eff,L} == \frac{-\ln(R)}{N_0 \ell_s \left[1 - \exp\left(-\frac{w_{0P,th}}{w_{P,sat}}\right)\right]}, \tag{4.22}$$

Insertion of experimental values into Eq. 4.22 (R = 0.03527, λ_P = 347.15 nm, $w_{0P,th} = 6\times10^{-4}$ J cm^{-2}, $w_{P,sat} = 6.09\times10^{-3}$ J cm^{-2}, $N_0 = 2.69\times10^{17}$ cm^{-3}, $\sigma_{a,P} = 9.4\times10^{-17}$ cm^2, ℓ_s = 1 cm) gives $\sigma_{em,eff,L} = 1.33\times10^{-16}$ cm^2. This value is in good agreement with the result of Fig. 4.11. The laser threshold is the lower the higher the dye cell reflectance R, the higher the dye number density N_0, the longer the excited dye cell length, the higher the dye absorption cross-section, $\sigma_{a,P}$, at the pump laser wavelength, the higher the stimulated emission cross-section $\sigma_{em,L}$, and the lower the excited-state absorption cross-section $\sigma_{ex,L}$.

4.1.3.2 Neat thin film wave-guided travelling-wave laser

The wave-guided travelling-wave laser action (wave-guided amplification of spontaneous emission) was studied using thin films of 2CzV-MEH-B spin-coated from a THF solution (concentration 15 mg/ml, speed 1600 rpm) onto microscope carrier plates (optical glass similar to Schott type BK7) and cut in the film region for optimum edge emission. A transverse pumping scheme was used. The pump pulse cross-sectional area (FWHM) at the sample was A = 14.5 × 0.245 mm^2.

In Fig. 4.7b above the normalized edge-emitted travelling-wave laser spectral shape (TWL), $S'_{TWL}(\lambda) = S_{TWL}(\lambda) / S_{TWL}(\lambda_{TWL,\max})$ is shown (solid line) for a pump pulse energy density of w_{0P} = 4×10^{-4} J cm^{-2}. The wavelength of peak TWL emission, $\lambda_{TWL,\,max}$, is at 519 nm for the film. For comparison the shape of the fluorescence quantum distribution is included in the figure.

The dependences of the collected laser output energy, W_{TWL}, of the laser wavelength peak position, $\lambda_{TWL,max}$, and of the spectral halfwidth (FWHM), $\Delta\lambda_{TWL}$, on the peak input pump laser energy density, w_{0P}, are displayed in Figs. 4.12a, b, and c, respectively.

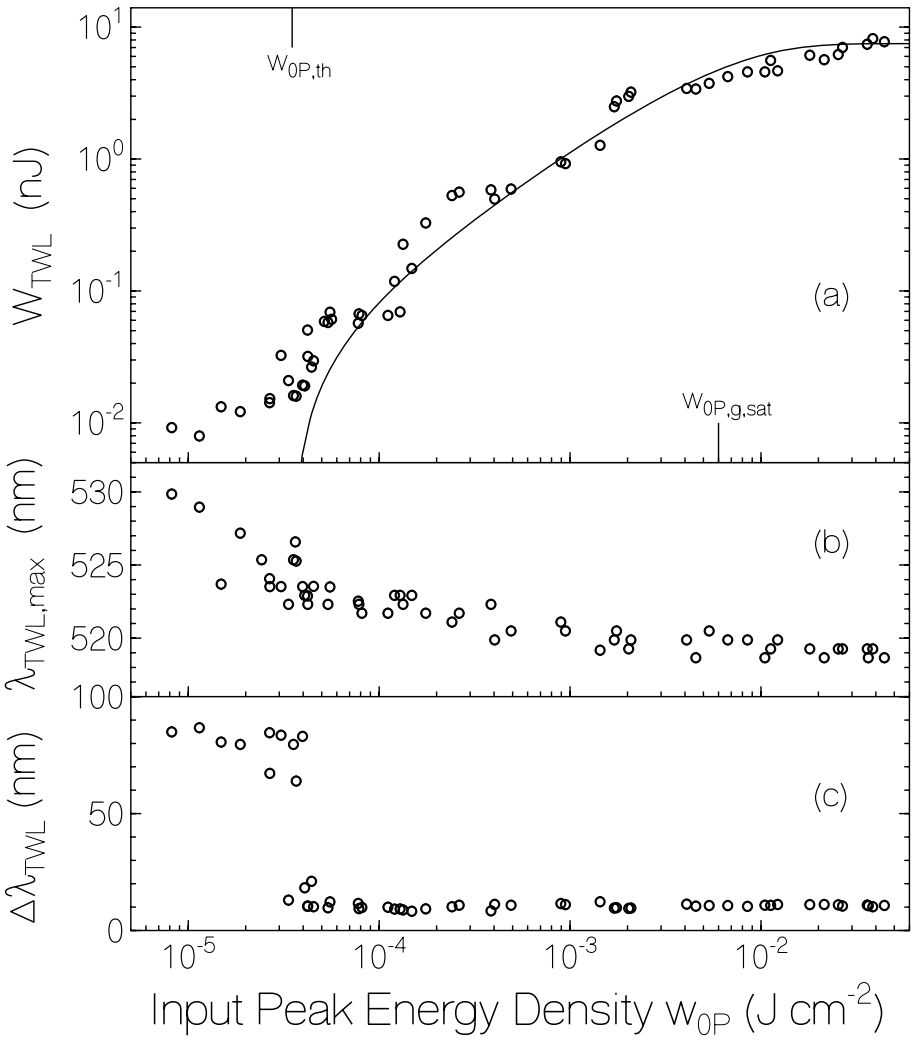

Fig. 4.12: Wave-guided travelling-wave laser performance of a 2CzV-MEH-B neat film on an optical glass substrate. Film thickness, d_f = 90 nm; pumped film area, 5 mm × 0.245 mm.
(a) Collected emission signal, W_{TWL}, versus input pump pulse energy density, w_{0P}. Full acceptance angle of fluorescence collection is $\Delta\theta$ = 0.3 rad. Curve is calculated by use of Eq. 4.23 with a pump laser threshold energy density $w_{0P,th}$ = 35 μJ cm^{-2}, a pump pulse energy density of gain saturation $w_{0P,g,sat}$ = 6 mJ cm^{-2}, and a maximum output energy $W_{TWL,max}$ = 7.5 nJ.
(b) Peak wavelength of travelling-wave laser, $\lambda_{TWL,max}$, versus input pump pulse energy density, w_{0P}.
(c) Spectral linewidth (FWHM) of travelling-wave laser, $\Delta\lambda_{TWL}$, versus input pump pulse energy density, w_{0P}.

In Fig. 4.12a, above a threshold pump pulse energy density, $w_{0P,th} \approx 4\times10^{-5}$ J cm^{-2}, the emission begins to rise beyond the spontaneous emission level due to stimulated emission (amplification of spontaneous emission). At high pump pulse energy density the output signal saturates to a maximum value, $W_{TWL,max} \approx 7.5$ nJ. The experimental behaviour is fitted by

$$W_{TWL} = W_{TWL,\max}[1-\exp(-\frac{w_{0P}-w_{0P,th}}{w_{0P,g,sat}-w_{0P,th}})], \tag{4.23}$$

where $w_{0P,g,sat} \approx 6\times10^{-3}$ J cm^{-2} is the pump pulse energy density of gain saturation. The saturation is thought to be caused by the exciton-exciton annihilation processes at high densities of excited molecules [Kep96, Hol02b].

In Fig. 4.12b, above laser threshold the wavelength position of peak light emission, $\lambda_{TWL,max}$, blue-shifts from about 530 nm at low excitation energy density towards 519 nm towards the position of peak stimulated emission cross-section at high excitation energy density (reduction of ground-state re-absorption).

In Fig. 4.12c it is seen that the spectral half-width, $\Delta\lambda_{TWL}$, of the light emission shrinks around the laser threshold from a spontaneous emission line-width of $\Delta\lambda_F \approx 85$ nm to $\Delta\lambda_{TWL} \approx 10$ nm, and then remains nearly constant.

The initial laser slope efficiency, $\eta_{sl,ini}$, at threshold concerning the collected TWL light is obtained from Eq. 4.22 by [Hol04a]

$$\eta_{sl,ini} = \frac{1}{A_{\exp}}\frac{\partial W_{TWL}}{\partial w_{0P}}|_{w_{0P}=w_{P,th}} = \frac{1}{A_{\exp}}\frac{W_{TWL,\max}}{w_{0P,g,sat}-w_{0P,th}}, \tag{4.24}$$

where A_{exp} is the exposed film area. A value of $\eta_{sl,ini} \approx 0.002$ is estimated. It should be noted that the true initial laser slope efficiency is larger since travelling-wave laser emission occurs in

forward and backward direction along the pump line focus and the emission angle at the film edge is larger than the acceptance angle of the collecting lens ($\Delta\theta = 0.3$ rad).

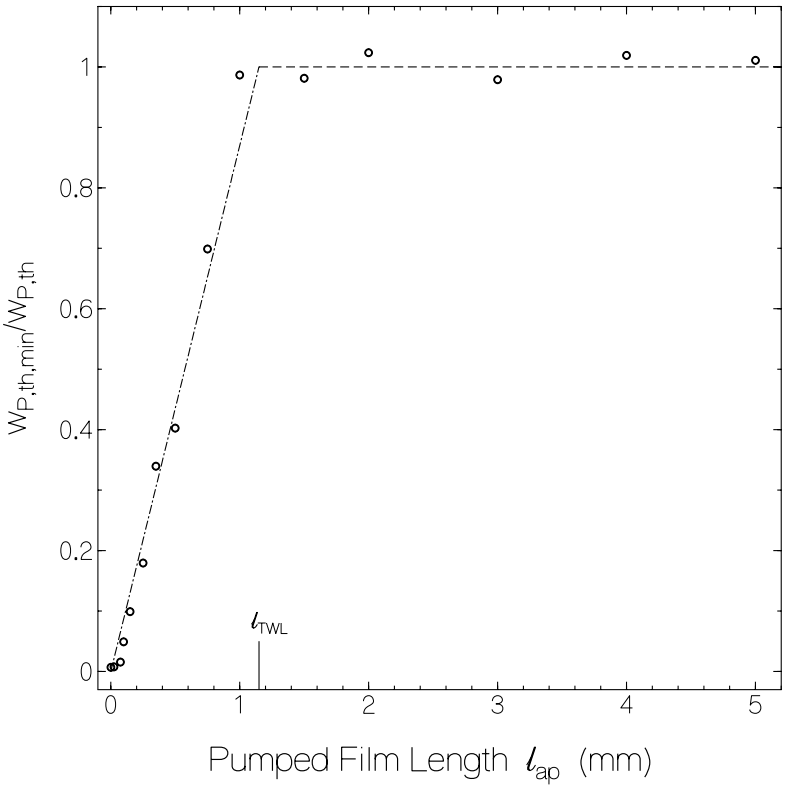

Fig. 4.13: Normalized inverse laser threshold pump pulse energy density, $w_{P,th,\min} / w_{P,th}$, versus exposed film length, ℓ_{ap}. The kink of the line gives the effective gain length, ℓ_{TWL}. Film thickness, $d_f = 90$ nm.

In Fig 4.13 the inverse ratio of the pump laser threshold energy density, $w_{P,th,min} / w_{P,th}$, versus the excited film length, ℓ_{ap}, is presented in order to determine approximately the effective length of light amplification, ℓ_{TWL}. The constant dashed line approximates the behaviour for pumped lengths longer than the effective gain length, and the dash-dotted line approximates the situation for pump lengths shorter than the effective gain length. From the crossing point of the lines one obtains $\ell_{TWL} \approx 1.15$ mm. If the gain length is limited by ground-state tail absorption, $\alpha(\lambda_{TWL,max})$, at the peak laser wavelength, $\lambda_{TWL,max} \approx 530$ nm, then it is $\alpha(530\text{ nm}) \approx \ell_{TWL}^{-1} \approx 8.7\text{ cm}^{-1}$ and the absorption cross-section is $\sigma_a(530\text{ nm}) = \alpha(530\text{nm})/N_f \approx 1\times10^{-20}\text{ cm}^2$.

4.1.3.3 Distributed-feedback laser

Distributed-feedback laser studies have been carried out for 2CzV-MEH-B neat thin films on corrugated gratings etched into a fused silica plate. Grating spacing of Λ = 320 nm, 300 nm, and 280 nm were used. The grating size was 1.5 mm × 0.5 mm (groove length 0.5 mm). The exposed grating area was 0.9 × 0.13 mm^2. The surface-emitted radiation was collected and detected. The laser wavelength, λ_{DFB}, is proportional to the grating spacing, and it increases with film thickness. TE modes (electrical field vector in film plane) and TM modes (electrical field vector perpendicular to film plane) are excited. The TE mode occurs at longer wavelength than the TM mode. A detailed description is given in [Hol02a].

Some lasing results are shown in Fig. 4.14 and some physical and spectroscopic parameters of the DFB lasers are collected in Table 4.2. In Fig. 4.14 the DFB laser spectra (solid curves) are compared with travelling-wave laser spectra (the same dash-dotted curves in each sub-figure), and with the shapes of the fluorescence quantum distributions. The spin-coated film on the substrate was 320 nm thick (solution 80 mg 2CzV-MEH-B per ml THF, spinning speed 2400 rpm). The DFB laser spectra shown were measured with no polarizer in the detection path. In Fig. 4.14a (grating spacing Λ = 320 nm) lasing occurred at λ_{DFB} = 513.5 nm (TM mode), the spectral width of $\Delta\lambda_{DFB} \approx 2$ nm. The applied pump pulse energy was $W_P \approx 190$ nJ, and the collected DFB laser energy was $W_{DFB} \approx 0.6$ nJ. In Fig. 4.14b (Λ = 300 nm) lasing occurred at λ_{DFB} = 513.5 nm with a spectral line-width of $\Delta\lambda_{DFB} \approx 2.6$ nm (TE mode) and at λ_{DFB} = 524.9 nm with $\Delta\lambda_{DFB} \approx 1.2$ nm (TM mode). The pump pulse energy was $W_P \approx 260$ nJ, and the collected DFB laser energy was $W_{DFB} \approx 3$ nJ. In Fig. 4.14c (Λ = 280 nm) lasing occurred at λ_{DFB} = 506.2 nm with $\Delta\lambda_{DFB} \approx 0.65$ nm (TE mode). The pump pulse energy was $W_P \approx 220$ nJ, and the collected DFB laser energy was $W_{DFB} \approx 1.2$ nJ.

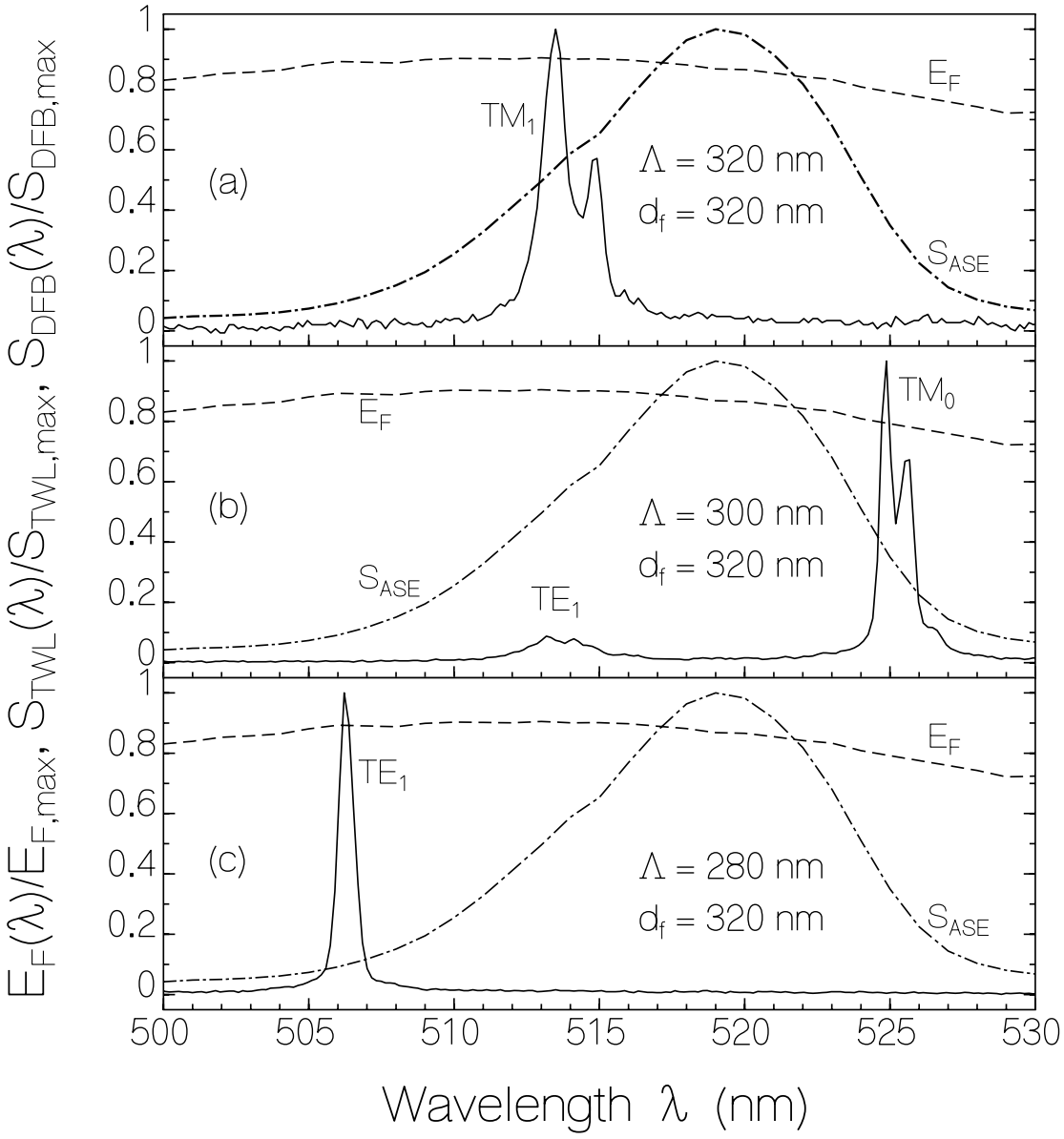

Fig. 4.14: Spectra of surface-emitting thin-film 2CzV-MEH-B distributed feed-back lasers (solid curves pumped area 0.9 mm × 0.13 mm, acceptance angle $\Delta\theta$ = 36°). For comparison edge emitted wave-guided thin-film travelling-wave laser emission spectrum (from Fig. 4.7b) and fluorescence quantum distribution (from Fig. 4.4) are included.
(a) DFB laser A. Grating spacing Λ = 320 nm. Film thickness d_f = 320nm. Applied pump pulse energy density $w_{0P} = 1.6\times10^{-4}$ J cm^{-2}.
(b) DFB laser B. Λ = 300 nm. d_f = 320nm. $w_{0P} = 2.2\times10^{-4}$ J cm^{-2}.
(c) DFB laser C. Λ = 280 nm. d_f = 320nm. $w_{0P} = 1.9\times10^{-4}$ J cm^{-2}.

Depending on the grating spacing and the film thickness the DFB laser wavelength could be tuned across the main part of the fluorescence spectrum. The DFB laser action suppressed the travelling-wave laser action.

A theoretical description of the DFB lasing allows the determinations of the polarisation mode (TE or TM, can also be determined by polarizer application), the number of the guided modes ($\kappa = 0, 1, 2, \ldots$ e.g. TE_0, TE_1, TM_0, …), the refractive index of the film (n_f), and the angle of propagation of the wavevector of the mode in the film (θ_κ). These determinations are carried out in the following.

The DFB laser wavelength is given by [Car98, Mor97]

$$\lambda_{DFB} = \frac{2\Lambda N}{p} = \frac{2\Lambda}{p} n_f \sin(\theta_\kappa) \ , \tag{4.25}$$

where $N = n_f \sin(\theta_k)$ is the effective refractive index, n_f is the refractive index of the film, and θ_κ is the wavevector angle of incidence in the film. p is the grating order (here used $p = 2$). In the case of using the grating in second-order ($p = 2$) with surface emission the diffraction order is $M = 1$ (angle of diffraction $\theta_d = 0°$) and the condition for constructive interference is given by [Hol02a]

$$\Lambda N = \Lambda n_f \sin(\theta_\kappa) = \lambda_{DFB} . \tag{4.26}$$

At fixed grating spacing, Λ, and film refractive index, n_f, the occurring laser wavelength, λ_{DFB}, is determined by the allowed propagation angles θ_κ which are determined by the resonance condition [Kog79]

$$\frac{4\pi}{\lambda_{DFB}} n_f d_{eff} \cos(\theta_\kappa) = \frac{4\pi}{\lambda_{DFB}} d_{eff} N \cot(\theta_\kappa) = 2\pi\kappa + 2\phi_s + 2\phi_c \tag{4.27}$$

where κ is the number of the guided mode (κ = 0,1,2,3,…), $d_{eff} = d + t\,c/\Lambda$ is the effective film thickness (d is film thickness, t is groove depth, c is groove width), ϕ_s is the phase change at the interface between the film and the substrate, and ϕ_c is the phase change at the interface between the film and the cover (air in our case). For TE modes these phase changes are (i = s or c) [Bir63].

$$\phi_{TE,i} = \arctan\left\{\frac{\left[n_f^2 \sin^2(\theta_\kappa) - n_i^2\right]^{1/2}}{n_f \cos(\theta_\kappa)}\right\}, \tag{4.28a}$$

and for TM modes they are

$$\phi_{TM,i} = \frac{n_f^2}{n_i^2}\,\phi_{TE,i}\,. \tag{4.28b}$$

To get a solution of Eq. 4.28 a minimum film thickness, $d_{\min,TE}$ for the TE_0 mode (Eq. 4.1a) and $d_{\min,TM}$ for the TM_0 mode (Eq. 4.1b), is required.

For neat film of 2CzV-MEH-B the application of Eq. 4.26 to the measured λ_{DFB} values of Fig. 4.14 determine the experimental effective refractive indices, $N = n_f \sin(\theta_\kappa)$. At fixed N the application of Eq. 4.27 to the experimental situation (fixed λ_{DFB}, d_{eff}) determines the angle of propagation, θ_κ, the film refractive index, n_f, the polarisation mode (TE or TM), and the number κ of the guided mode (for other parameters no solution at the fixed DFB laser emission wavelength, λ_{DFB}). The obtained parameters for the DFB laser spectra of Fig. 4.14 are listed in Table 4.2. The obtained film refractive indices, $n_{f,TE}$ and $n_{f,TM}$, from the DFB laser analysis are included in Fig. 4.2. The refractive indices obtained for the TE polarization and the TM polarization are approximately the same indicating that the spin-coated film on the grating is isotropic (no refractive index anisotropy due to special molecular alignment). The refractive indices obtained from the grating analysis agree reasonably well with the film refractive index data obtained from reflectance and transmittance measurement and Fresnel equation analysis.

Table 4.2: Physical and spectroscopic parameters of 2CzV-MEH-B distributed feedback lasers.

Parameter	DFB laser A	DFB laser B		DFB laser C
Λ (nm)	320	300		280
t (nm)	50	50		50
c (nm)	160	150		140
d_f (nm)	320	320		320
d_{eff} (nm)	345	345		345
M	1	1	1	1
λ_{DFB} (nm)	513.5	513.5	524.9	506.2
N	1.605	1.712	1.750	1.808
	TM	TE	TM	TE
κ	1	1	0	1
θ_κ (°)	50.35	56.96	68.76	58.05
n_f	2.08	2.05	1.88	2.13
d_{min} (nm)	69.47	36.15	89.27	31.23
θ_{crit} (°)	44.58	45.41	50.95	43.27
$\ell_{\parallel, exc}$ (mm)	0.9	0.9	0.9	0.9
$\ell_{\perp,exc}$ (mm)	0.13	0.13	0.13	0.13

Abbreviations: Λ: groove spacing. t: groove depth. c: groove width. d_f: film thickness. d_{eff}: effective film thickness in grating region. M: diffraction order. λ_{DFB}: distributed-feedback laser wavelength. N: effective refractive index. κ: guided mode number. θ_κ: propagation angle. n_f: refractive index of film. d_{min}: minimal film thickness for wave-guiding. θ_{crit}: critical angle for total internal reflection ($\theta_{crit} = \arcsin(n_s / n_f)$ with n_s refractive index of substrate). $\ell_{\parallel, exc}$: length of exposed grating area. $\ell_{\perp,exc}$: width of exposed grating area.

4.1.4 Conclusions

For the oligomeric dicarbazovinylene-MEH-benzene emitter high fluorescence efficiency of $\phi \approx 0.86$ was found in liquid solution. In the solid state the fluorescence efficiency reduced to $\phi \approx 0.062$ due to fluorescence self quenching probably by charge transfer and subsequent non-radiative charge recombination. The excited-state absorption cross-section spectrum in the lasing wavelength region was found to be (a factor of 3.2 at 492 nm) smaller than the stimulated emission cross-section allowing laser oscillation. In liquid solution a transverse pumped low-Q resonator dye cell laser was realized. Wave-guided travelling-wave laser edge emission was achieved for a thin film spin-coated on a glass substrate. Narrow spectral line-width surface emitting laser action with low laser threshold was obtained by transverse pumping of a spin-coated film on corrugated gratings.

The performed laser studies show that the application of the blue and green emitting di-carbazovinylene-MEH-benzene dye ADS084BE in organic light emitting devices may be extended to integrated-optics laser devices.

4.2 Triphenylamine dimer (TPB) and napthalene substituted triphenylamine dimer (β–NPB)

The widely used electroluminescent 3-methyl-TPD [Hol00] and its structure isomer 4-methyl-TPD [Phi03] turned out to work as efficient blue-wavelength thin-film lasers. Laser action was achieved for triphenylamine dimer (TPD) based conjugated and non-conjugated polymers [Hol02]. Here the hole transport materials N,N,N',N'-tetraphenylbenzidine (abbreviated TPB, also called triphenylamine dimer TAD, TPD without methyl group) [Kam04, Sar06] and N,N'-bis(2-naphtalenyl)-N,N'-bis(phenylbenzidine) (abbreviated β-NPB, also called naphtyl-diphenylamine dimer β-NPD) [Gro99, Sat00] are investigated.

The dyes are studied as neat thin films and dissolved in the organic liquid tetrahydrofuran (THF). Absorption cross-section spectra, stimulated emission cross-section spectra, fluorescence quantum distributions, fluorescence quantum yields, degrees of fluorescence polarisation, and fluorescence lifetimes are determined. In THF solution the excited-state absorption cross-sections of the dyes at 347.15 nm (wavelength of second harmonic of mode-locked ruby laser) are determined by saturable absorption measurements. The dyes are investigated for neat thin-film and organic-solution laser action. Low-Q laser oscillation is studied by transverse pumping the solutions in a rectangular cell. The solid-state dye lasing behaviour is investigated by transverse pumping a neat thin dye film on a glass plate and observing the amplification of spontaneous emission (wave-guided travelling-wave lasing).

4.2.1 Optical and spectroscopic characterization

The transmittance spectra, $T(\lambda)$, and the reflectance spectra, $R(\lambda)$, of a TPB and a β-NPB thin film on fused silica substrates are shown in Fig. 4.15. The transmittance and reflectance of blank substrate are also shown (dash-dotted curves). The films were prepared by spin-coating of THF

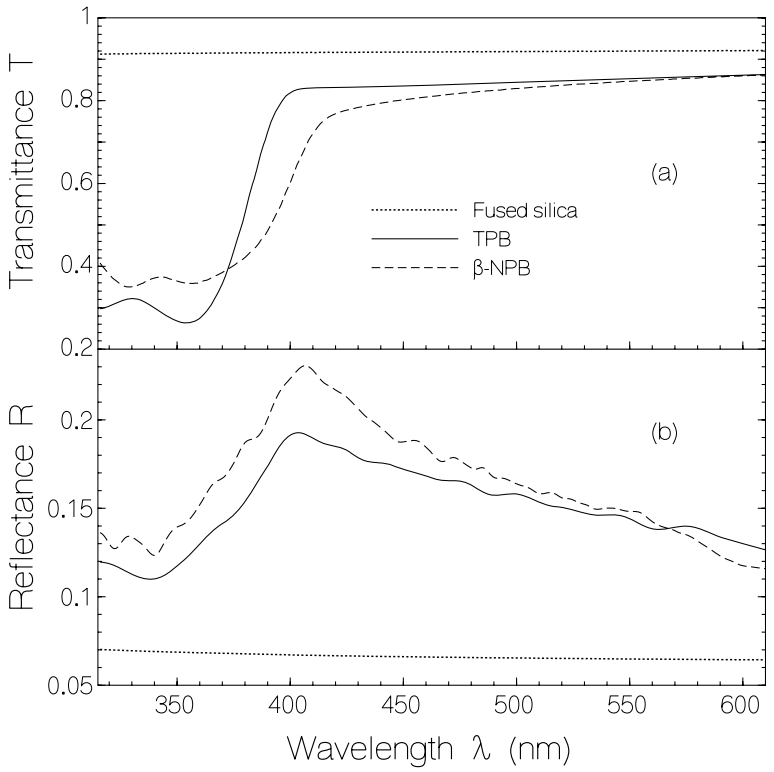

Fig. 4.15: (a) Transmittance, $T(\lambda)$, and (b) reflectance, $R(\lambda)$, spectra of a TPB film (solid curves, thickness d_f = 69.5 nm) and a β-NPB film (dashed curves, d_f = 57 nm) on fused silica substrates. Films were prepared by spin-coating from THF solution. Dotted lines belong to blank fused silica.

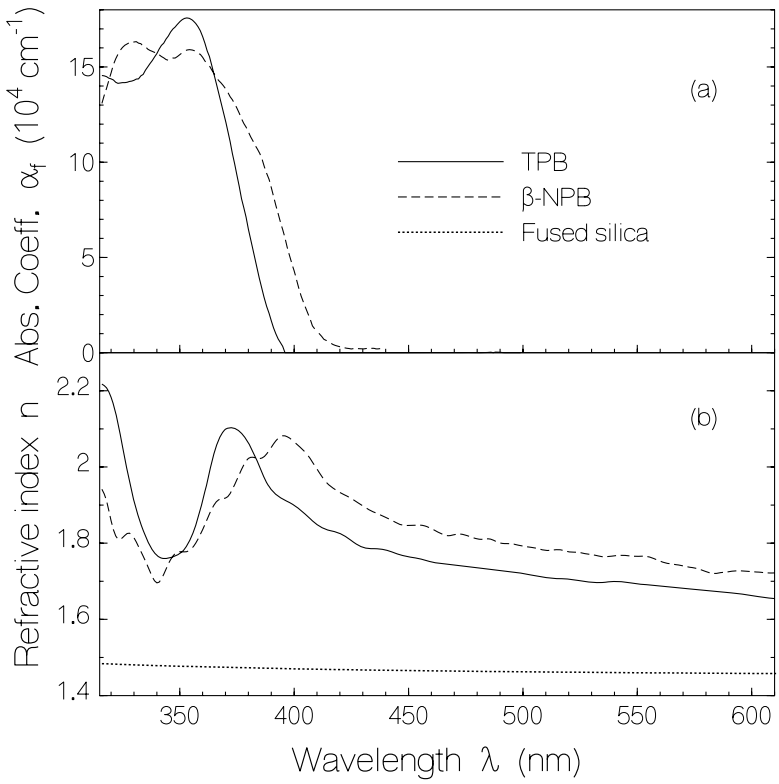

Fig. 4.16: (a) Absorption coefficient spectra, $\alpha_f(\lambda)$, and (b) refractive index, $n(\lambda)$, spectra of TPB film, β-NPB film, and fused silica substrate.

solutions. For TPB film preparation a dye concentration of 15 mg/ml was used and the spin-coater angular speed was 900 rpm. For β-NPB film preparation a dye concentration of 10 mg/ml was used and the spin-coater angular speed was 1200 rpm. The TPB film and the β-NPB have a transmission minimum at about 355 nm. The reflectance of both films has a minimum at about 340 nm and a maximum at about 405 nm.

The absorption coefficient spectra and the refractive index spectra together with the film thicknesses are extracted by a Fresnel equation approach [Pen98, Hol99] and are shown in Fig. 4.16. The film thickness turned out to be d_f = 69.5 nm for TPB and d_f = 57 nm. The absorption maximum occurs at 354 nm for TPB and at 355 nm for β-NPB. At these wavelengths the light penetration depth is $d_p = \alpha_f^{-1}$ = 57 nm for TPB and 63 nm for β-NPB. The refractive index spectra show the expected dispersion shapes. In the displayed wavelength range the film refractive indices are larger than the fused silica or optical glass refractive indices. Therefore optical wave-guiding takes place in films above a critical film thickness [Kog79]. By Eqs. 4.1a and 4.1b at λ = 420 nm, the critical film thicknesses are $d_{min,TE}$(TPB) = 48.1 nm, $d_{min,TM}$(TPB) = 91.2 nm, $d_{min,TE}$(β-NPB) = 37.6 nm, and $d_{min,TM}$(β-NPB) = 79 nm.

The absorption cross-section spectra, $\sigma_a(\lambda)$, of TPB and β-NPB in THF and as neat film are displayed in Fig. 4.17 (the neat film curves are calculated assuming the same S_0-S_1 absorption cross-section integral for the solution and the film, see above). The absorption cross-section spectra of the film and the solution have similar shape, only the solution absorption spectra are approximately 6 nm blue-shifted. The TPB and β-NPB molecule number densities in the film are estimated to be $N_f = \alpha_f / \sigma_{a,f} \approx 1.4\times10^{21}$ cm^{-3} and 1.0×10^{21} cm^{-3}, respectively (calculated at λ =

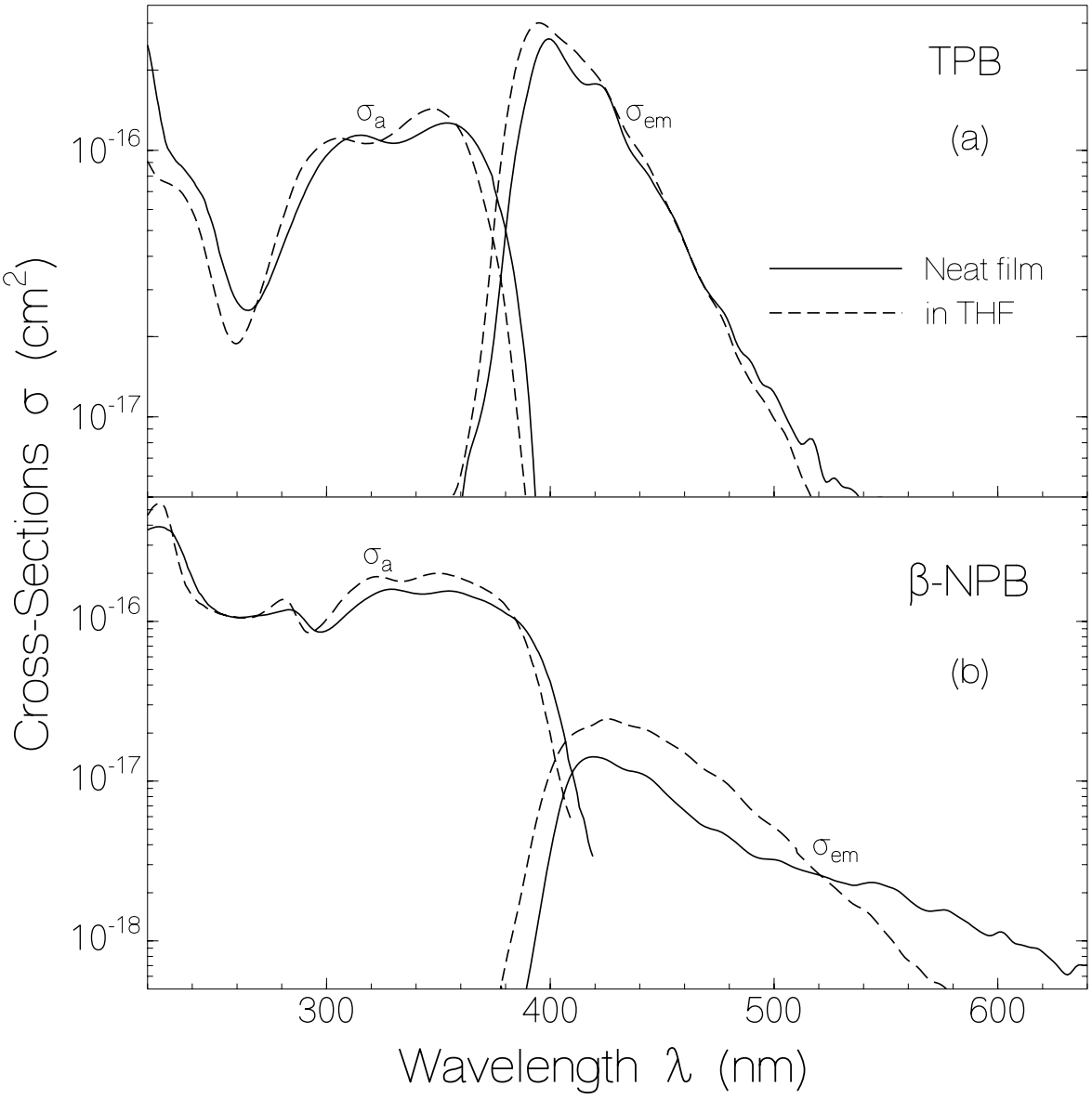

Fig. 4.17: Absorption cross-section, $\sigma_a(\lambda)$, and stimulated emission cross-section, $\sigma_{em}(\lambda)$, spectra of (a) TPB neat thin film (solid curves) and of tetrahydrofuran (THF) solution (dashed curves, concentration $C = 2.1\times10^{-4}$ mol dm^{-3}), and (b) β-NPB neat thin film (solid curve) and of THF solution (dashed curves, $C = 7.2\times10^{-5}$ mol dm^{-3}).

353 nm). The mass densities, ρ, of the neat thin films are determined to be $\rho = (N_f / N_A) M_m$ ≈1.136 g cm^{-3} for TPB and ≈ 0. 978 g cm^{-3} for β-NPB, where N_A is the Avogadro constant and M_m is the molar mass.

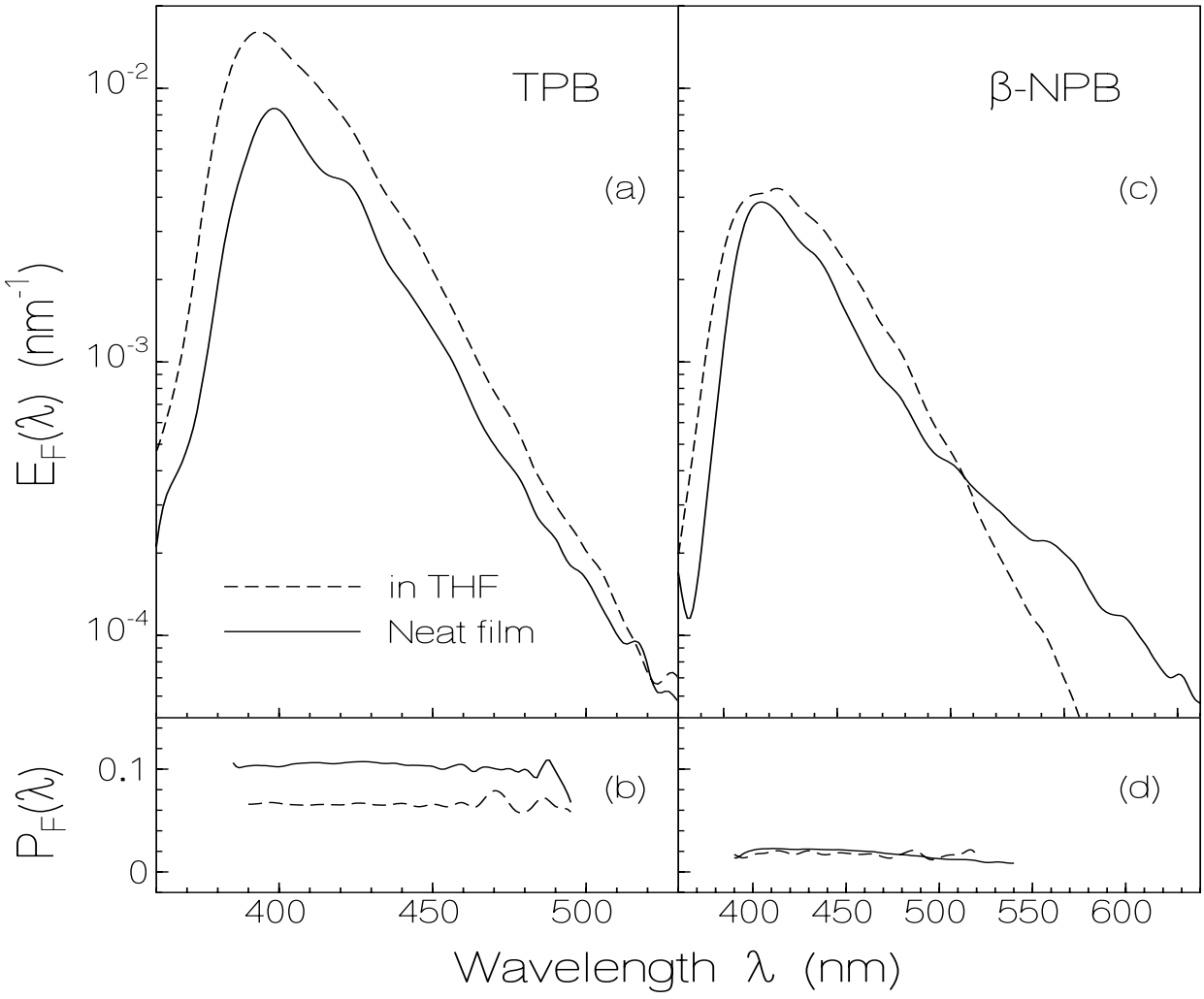

Fig. 4.18: (a,c) Fluorescence quantum distributions, $E_F(\lambda)$, and (b,d) degrees of fluorescence polarization, $P_F(\lambda)$, of TPB (a,b) and β-NPB (c,d). Excitation wavelengths λ_{exc} = 343 nm for TPB ands λ_{exc} = 365 nm for β-NPB. Solid curves belong to neat films (d_f(TPB) = 69.5 nm, d_f(β-NPB) = 97 nm), and dashed curves belong to solutions in THF (concentrations C(TPB) = 2.95×10^{-5} mol dm^{-3}, C(β-NPB) = 2.13×10^{-5} mol dm^{-3}).

The fluorescence quantum distributions, $E_F(\lambda)$, of TPB and β-NPB in THF and as neat films are shown in Fig. 4.18a and Fig. 4.18c, respectively. The fluorescence quantum yields, ϕ_F, (Eq. 3.5) of the solutions are ϕ_F(TPB) = 0.73±0.01, ϕ_F(β-NPB) = 0.28±0.01, and of the films are ϕ_F(TPB) = 0.36±0.01, ϕ_F(β-NPB) = 0.215±0.01. The results are collected in Table 4.3. The fluorescence in the solutions is higher than in the neat films (some self-quenching occurs).

The degrees of fluorescence polarisation, P_F, of TPB and β-NPB are shown Fig. 4.18b and Fig. 4.18d, respectively, for both THF solutions and neat films. The average values are collected in Table 4.3. For TPB the values are P_F(solution) = 0.065 and P_F(neat film) = 0.105. For β-NPB the values are P_F(solution) ≈ P_F(neat film) ≈ 0.02. In the solutions the obtained degree of fluorescence polarization is determined by molecular reorientation, while in the neat films it is determined by site-to-site excitation transfer [Lak83].

The degree of fluorescence polarisation, P_F, is related to the reorientation time, τ_{or}, of the transition dipole moments by Eq. 4.4. For TPB in THF it is $P_F \approx 0.065$ and $\tau_F \approx 850$ ps (see below) giving $\tau_{or} \approx 106$ ps. For TPB neat thin film it is $P_F \approx 0.105$ and $\tau_F \approx 300$ ps (see below) giving $\tau_{or} \approx 67$ ps. For β-NPB in THF and as neat film it is $P_F \approx 0.02$ while τ_F(THF) ≈ 3.76 ns and τ_F(neat film) ≈ 2.94 ns (see below) giving τ_{or}(THF) ≈ 130 ps and τ_{or}(neat film) ≈ 102 ps. The reorientation time in the solvent THF is determined by the viscosity and temperature dependent molecular reorientation ($\tau_{or} = \eta V_h / (k_B \vartheta)$ [Fle86] where η the dynamic viscosity, V_h is the hydrodynamic molecular volume, k_B is the Boltzmann constant, and ϑ is the temperature). The short reorientation time in the neat films is caused by fast excitation transfer in the random oriented molecules in the neat films (dipolar Förster-type energy transfer [För51, Val02] and Dexter-type exchange transfer [För51, Dex53]).

The temporal fluorescence signals of a 7.8×10^{-5} molar solution of TPB in THF (line-connected open circles) and of a TPB neat film (thickness d_f = 110 nm, line-connected dots) are shown in Fig. 4.19a. The dotted curve shows the detection system response function $g(t)$ (attenuated pump pulses directed to micro-channel-plate photomultiplier). The lines are convolutions of the experimental response function with single-exponential decays according to,

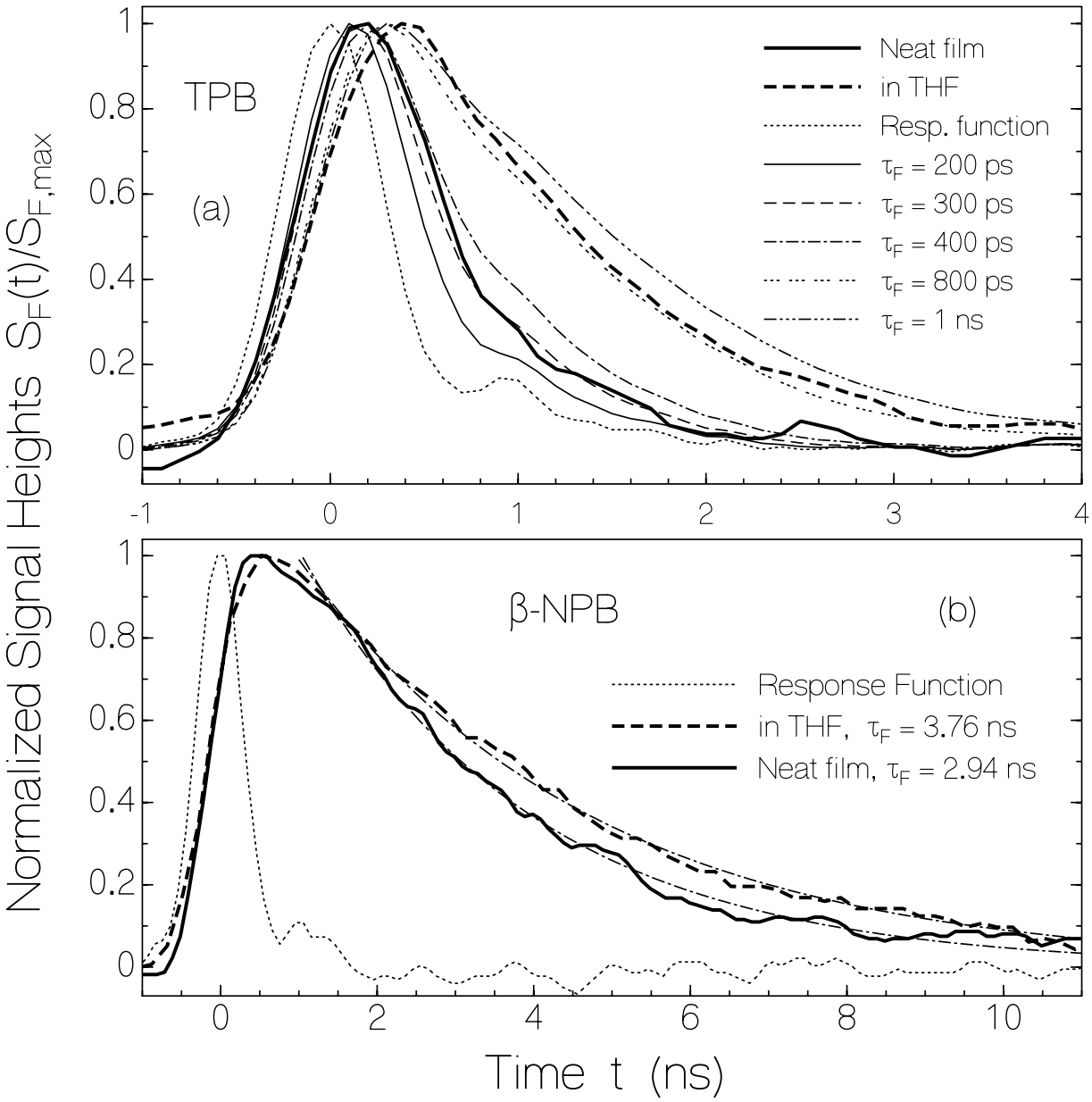

Fig. 4.19: Temporal fluorescence traces of TPB (a) and β–NPB (b) in THF (thick dashed curves) and as neat films (thick solid curves). Dotted curves show response functions. The thin lines in (a) are calculated convolution curves (Eq. 4.29) and the thin dash-dotted lines in (b) are non-linear regression fits.

$$S_{F,con}(t) = \int_{-\infty}^{t} g(t')S_{F,\delta}(t-t')dt' \tag{4.29a}$$

with

$$S_{F,\delta}(t) = S_{F,0}\begin{cases}\exp(-t/\tau_F) & for\ t \geq 0\\ 0 & for\ t < 0\end{cases} \tag{4.29b}$$

The experimental fluorescence curves are compared with the theoretical convoluted single-exponential decay curves in order to estimate the fluorescence lifetimes. For TPB in THF a value of $\tau_F \approx 850$ ps is determined. For the TPB neat film a value of $\tau_F \approx 300$ ps is obtained.

The temporal fluorescence signals of a 2.4×10^{-5} molar solution of β-NPB in THF (dashed curve) and of a β-NPB neat film (thickness $d_f = 66$ nm, solid curve) are shown in Fig. 4.19b. The dotted curve gives the system response function. The fluorescence signal decays are fitted by single-exponential decay functions, i.e. $S_F(t) = S_{F,0}\exp(-t/\tau_F)$. The best fitting fluorescence lifetimes are τ_F(β-NPB in THF) = 3.76 ns, and τ_F(β-NPB neat film) = 2.94 ns.

The radiative lifetime, τ_{rad}, of the emitting chromophores is given by the ratio of the fluorescence lifetime, τ_F, to the fluorescence quantum yield, ϕ_F, and is given by Eq. 4.5. The experimental values are τ_{rad}(TPB in THF) ≈ 1.16 ns, τ_{rad}(TPB neat film) ≈ 0.83 ns, τ_{rad}(β-NPB in THF) ≈ 13.4 ns, and τ_{rad}(β-NPB neat film) ≈ 13.7 ns.

The stimulated emission cross-section spectra, $\sigma_{em}(\lambda)$, of the solutions and the neat films has been calculated from the Einstein relation [Pet71, Des90] using Eq. 4.3. The stimulated emission cross-section spectra are included in Fig. 4.17.

The maximum of the stimulated emission cross-section spectrum of the TPB neat film is about 5 nm red-shifted compared to TPB dissolved in THF. The vibronic structure is more pronounced in the neat film than in the solution. The peak stimulated emission cross-sections are larger than the peak S_0-S_1 absorption cross-sections because of smaller spectral broadening of the emission spectra compared to the absorption spectra ($\Delta\tilde{\nu}_{em}(\textit{neat film}) \approx 2500$ cm^{-1}, $\Delta\tilde{\nu}_a$(neat film) ≈ 4600 cm^{-1}, inhomogeneous spectral broadening of absorption spectra).

The maximum of the S_1-S_0 stimulated emission cross-section of β-NPB is roughly a factor of ten smaller than the maximum cross-section of the first absorption band. This indicates that first exited-state S_1 is hidden in the tail of the broad first absorption band (note that $\int_{S0-S1}\sigma_a(\nu)d\nu \approx \int_{S1-S0}\sigma_{em}(\nu)d\nu$ according to the relation between the Einstein coefficients of absorption and emission [Des90, Pet71]). The neat film emission shoulder around 550 nm is likely due to photo-induced excited-state dimer (excimer, dimeric exciton) formation [Val02, And04, Ban06].

4.2.2 Saturable absorption behaviour

The experimental energy transmission, T_E, of second harmonic picosecond ruby laser pulses (duration Δt_P = 35 ps, wavelength λ_P = 347.15 nm) through a 1 mm cell filled with either TPB or β-NPB in THF as a function of the input peak pulse intensity, I_{0P}, is shown by circles in Fig. 4.20a and 4.20b respectively. The transmission rises from the small-signal transmission of $T_0 \approx$ 0.1 at low excitation intensity to T_E(TPB) ≈ 0.52 and T_E(β-NPB) ≈ 0.4 at excitation intensity I_{0P} = 2×10^{10} W cm^{-2}. The solid curves in Fig. 4.20a and 4.20b are numerical simulations to the transmission measurements obtained by using the Eqs. 4.6- 4.13 described in section 4.1.2. The best fit to the experimental data is obtained for $\sigma_{ex,P}$(TPB) = 4×10^{-17} cm^2 and $\sigma_{ex,P}$(β-NPB) = 7×10^{-17} cm^2.

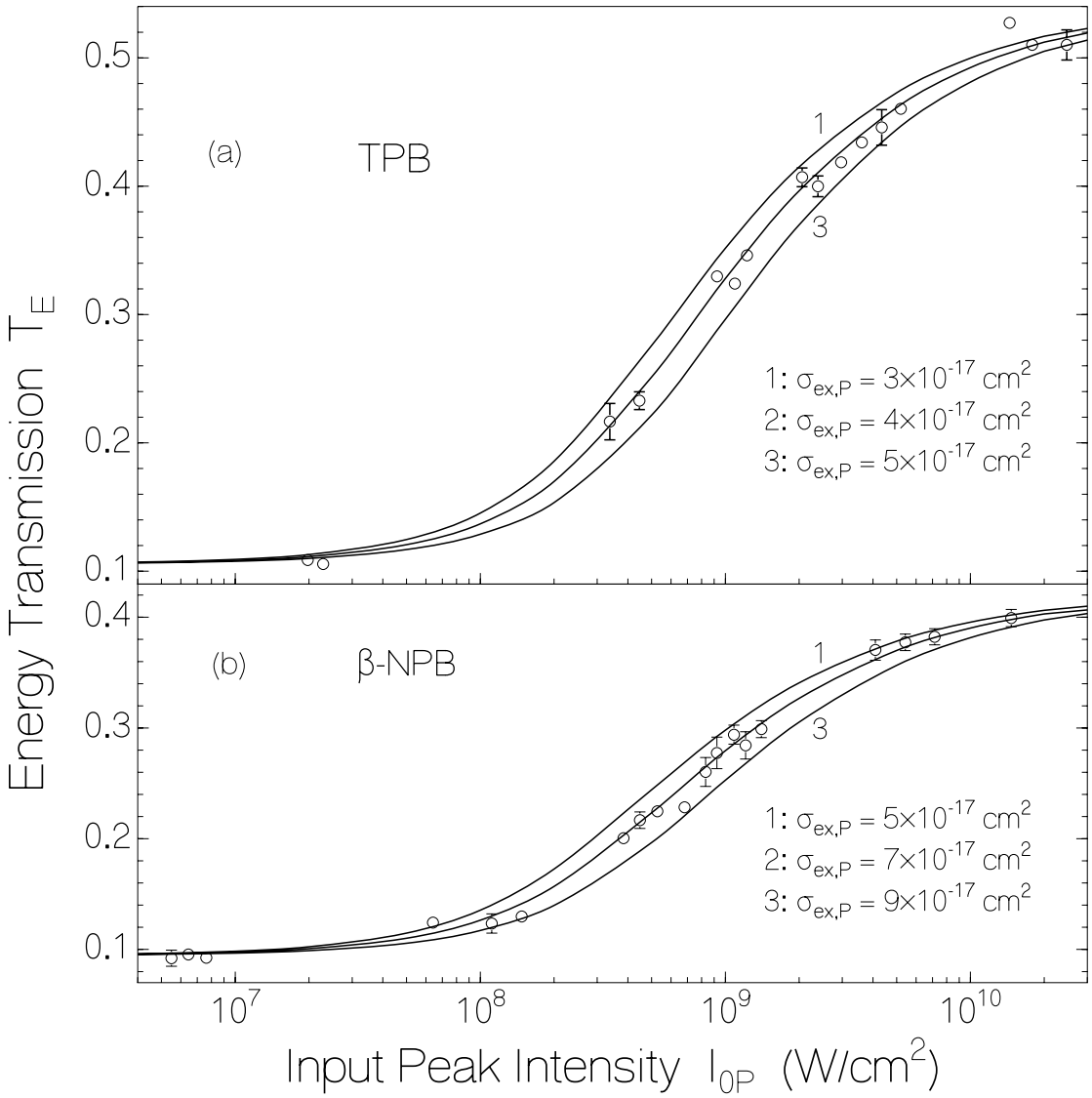

Fig. 4.20: Saturable absorption behaviour of (a) TPB and (b) β-NPB in THF. Circles are measured. Curves are calculated using excited-state absorption cross-sections $\sigma_{ex,P}$ listed in the figures. Pump laser pulses: second harmonic of picosecond ruby laser (wavelength 347.15 nm, duration 35 ps FWHM).

Table 4.3: Optical and spectroscopic parameters of TPB and β-NPB

Parameter	TPB in THF	TPB neat film	β-NPB in THF	β-NPB neat film	Comments
$\lambda_{a,max}$ (nm)	347.5	354	350	355	Fig. 4.17
$\lambda_{em,max}$ (nm)	394	400	426	419	Fig. 4.17
$\lambda_{F,max}$ (nm)	394	398.5	420	417	Fig. 4.18
n_F	1.4138 [Hel62]	1.90	1.4116 [Hel62]	1.93	for film: Fig. 4.16b
ϕ_F	0.73±0.01	0.36±0.01	0.28±0.01	0.215±0.01	Fig. 4.18
P_F	0.065±0.01	0.105±0.01	0.02±0.005	0.02±0.005	Fig. 4.18
τ_F (ns)	0.85±0.05	0.3±0.05	3.76±0.1	2.94±0.1	Fig. 4.19
τ_{rad} (ns)	1.16	0.83	13.4	13.7	Eq. 4.5
τ_{or} (ps)	106±15	66.5±7	130.5±30	102±25	Eq. 4.4

Abbreviations: $\lambda_{a,max}$: wavelength of peak absorption cross-section of first absorption band. $\lambda_{em,max}$: wavelength of peak stimulated emission cross-section. $\lambda_{F,max}$: wavelength of fluorescence maximum. n_F: average refractive index in fluorescence region. ϕ_F: fluorescence quantum yield. P_F: degree of fluorescence polarisation. τ_F: fluorescence lifetime. τ_{rad}: radiative lifetime. τ_{or}: transition dipole moment reorientation time.

4.2.3 Laser performance

The transverse pumped lasing in a 1 cm × 1 mm dye-laser cell and the wave-guided travelling-wave lasing (amplification of spontaneous emission) of neat thin films on microscope carrier plates are studied. Laser action is achieved for TPB but no laser action is observed for β-NPB.

4.2.3.1 Transverse pumped low-Q laser

As described above in section 4.1.3.1 in the low-Q lasing studies the dye solution in a 1 cm ×1 mm fused silica cell was transversally pumped with line-focused picosecond second-harmonic pulses of a ruby laser system (pump beam cross-section 14.5 mm × 0.245 mm). The dye cell itself forms the optical laser resonator (low-Q resonator): the end surfaces of the cell acts as mirrors (reflectance $R = (n-1)^2/(n+1)^2 = 0.0361$, $n = 1.4691$ is refractive index of cell glass at 410 nm).

In Fig. 4.21a a normalized output spectrum of the low-Q laser, $S_{LQL}(\lambda)/S_{LQL,max}$, is shown. The active medium is 3.2×10^{-4} molar TPB in THF. The applied excitation pulse energy density for the laser spectrum in Fig. 4.21b was 34.2 mJ cm^{-2}. The emission maximum is at $\lambda_{LQL,max}$ = 411 nm. It is red-shifted compared to the wavelength position of peak stimulated emission cross-section which occurs at 394 nm. The laser line-width is $\Delta\lambda_{LQL} \approx 10$ nm (FWHM).

The dependences of the laser output energy, W_{LQL}, of the laser wavelength peak position, $\lambda_{LQL,max}$, and of the spectral halfwidth (FWHM), $\Delta\lambda_{LQL}$, on the peak input pump laser energy density, w_{0P}, are displayed in Fig. 4.22a, b, and c, respectively. In Fig. 4.22a, above a certain threshold pump pulse energy density of laser action, $w_{0P,th} \approx 3$ mJ cm^{-2}, the emission rises steeply beyond the spontaneous emission and amplified spontaneous emission level due to low-Q laser oscillation action. In Fig. 4.22b it is seen, that the wavelength position of light emission below laser oscillator threshold is at about 425 nm, and above laser threshold it is at about 410 nm. The

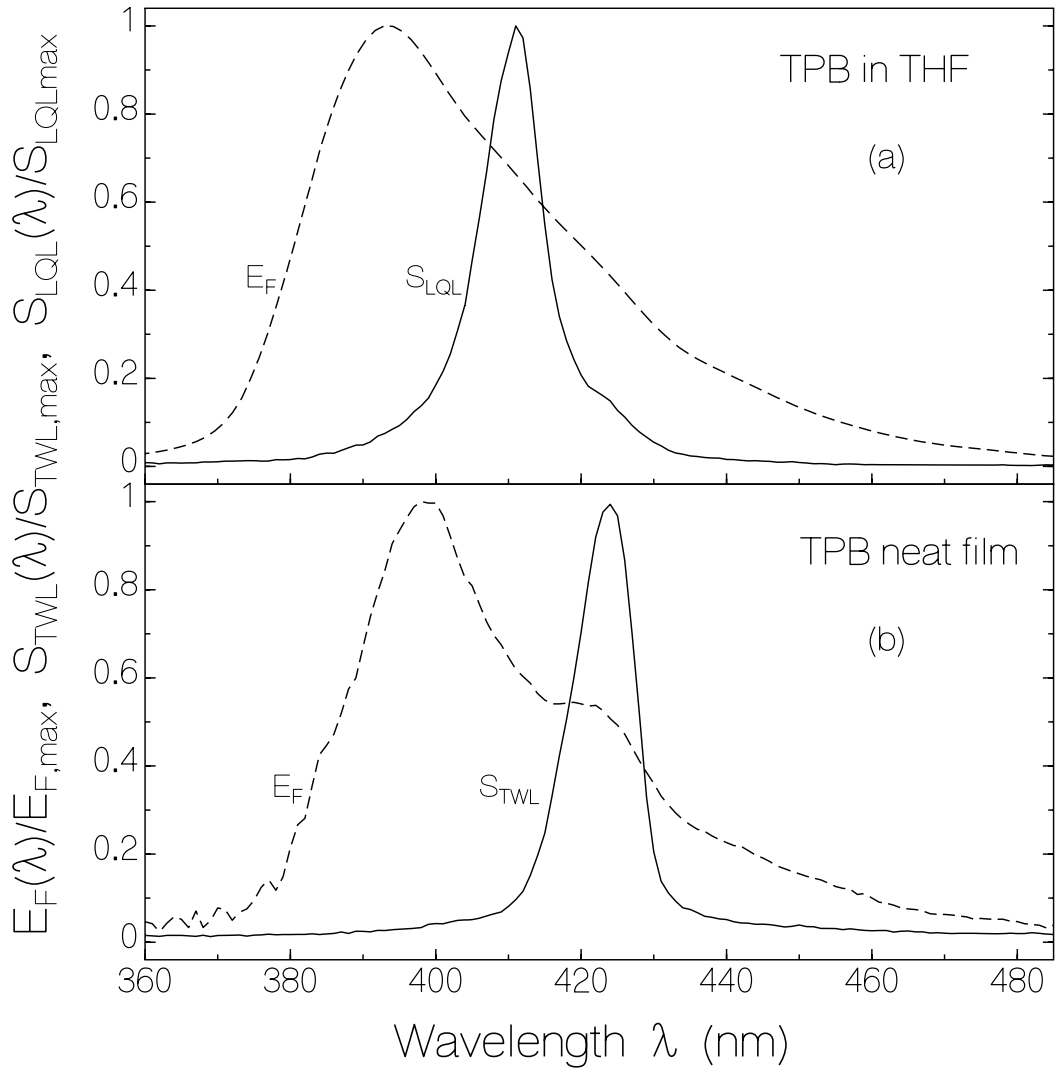

Fig. 4.21: Spectral shapes of (a): low-Q laser emission, $S_{LQL}/S_{LQL,max}$, of TPB in THF (concentration 3.2×10^{-4} mol dm^{-3}, excitation energy density w_{0P} = 34.2 mJ cm^{-2}).
(b): wave-guided travelling wave laser emission, $S_{TWL}/S_{TWL,max}$, of TPB neat film (thickness 262 nm, w_{0P} = 227 μJ cm^{-2}). For comparison the normalized fluorescence quantum distributions, $E_F(\lambda)/E_{F,max}$, are also displayed.

peak position of the stimulated emission cross-section is at about 394 nm. The wavelength position of the peak laser emission is thought to be caused by ground-state re-absorption. In Fig. 4.22c it is seen that the spectral halfwidth, $\Delta\lambda_{TWL}$, of the light emission shrinks down from about 48 nm before laser action ($w_{0P} < w_{0P,th}$) to about 15 nm above laser threshold.

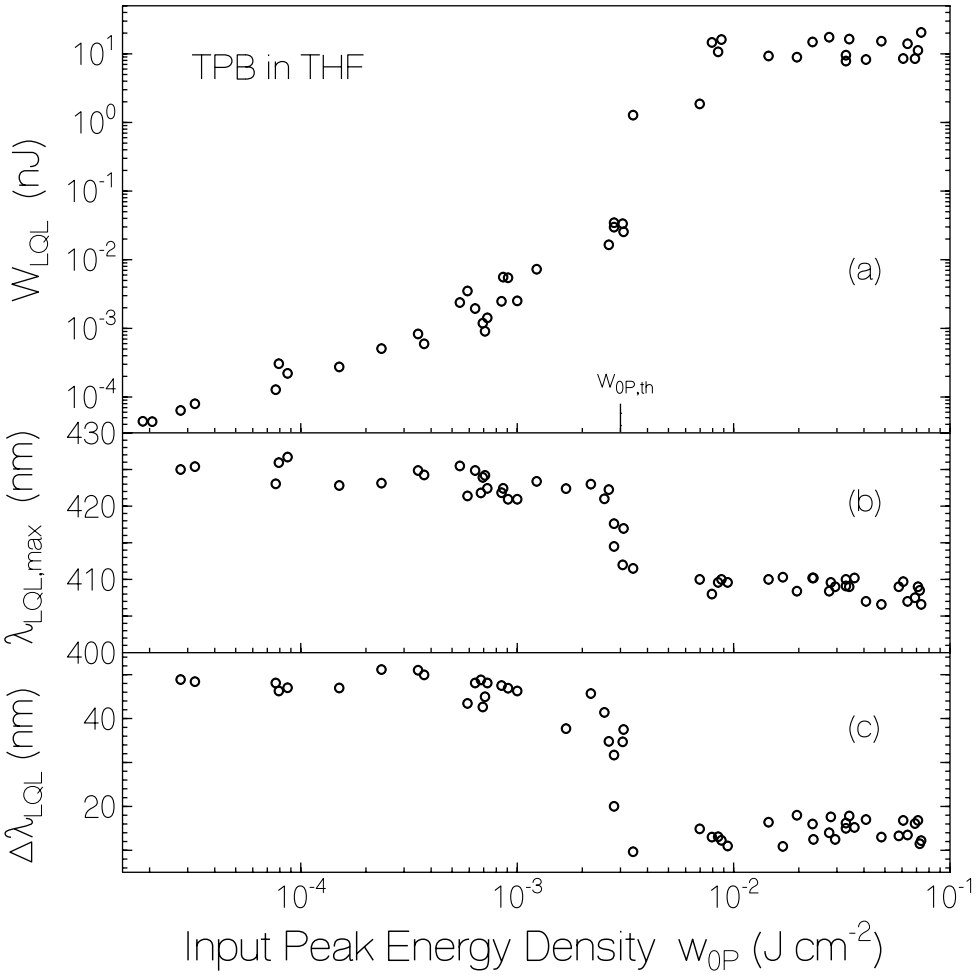

Fig. 4.22: Low-Q laser oscillator performance of TPB/THF in a dye-laser cell (1 cm length, 1 mm thick) transverse pumped with line-focused (beam cross-section 14.5 mm × 0.245 mm) second harmonic pulses of a mode-locked ruby laser ($\Delta t_P \approx 35$ ps, $\lambda_P = 347.15$ nm). Dye concentration $C_0 = 3.2\times10^{-4}$ mol dm^{-3}.
(a) Collected emission signal, W_{LQL}, versus input pump pulse energy density, w_{0P}. Full acceptance angle of fluorescence collection is $\Delta\theta = 0.82°$. Pump laser threshold energy density $w_{0P,th} \approx 3$ mJ cm^{-2}.
(b) Peak wavelength of low-Q laser oscillator, $\lambda_{LQL,max}$, versus input pump pulse energy density, w_{0P}.
(c) Spectral line-width (FWHM) of low-Q laser oscillator, $\Delta\lambda_{LQL}$, versus input pump-pulse energy density, w_{0P}.

Insertion of experimental values into Eq. 4.22 ($R = 0.0361$, $w_{0P,th} = 3\times10^{-3}$ J cm^{-2}, $w_{P,sat} = 4.0\times10^{-3}$ J cm^{-2}, $N_0 = 1.92\times10^{17}$ cm^{-3}, $\sigma_{a,P} = 1.43\times10^{-16}$ cm^2, $\ell_s = 1$ cm) gives $\sigma_{em,eff,L} = 3.28\times10^{-17}$

cm^2. Using $\sigma_{em,L} = 2.35\times10^{-16}$ cm^2 (λ_L = 411 nm) an excited-state absorption cross-section of $\sigma_{ex,L} = 2.02\times10^{-16}$ cm^2 is determined.

The dye β-NPB in THF showed no indication of low-Q laser action (no spectral narrowing of the emission). The same arrangement as for TPB in THF was used. The applied dye number density was $N_0 = 1.77\times10^{17}$ cm^{-3}, and pump pulse energy densities up to 0.057 J cm^{-2} were applied ($w_{0P,th} > 0.057$ J cm^{-2}). The pump pulse saturation energy of β-NPB is $w_{P,sat} = 2.89\times10^{-3}$ J cm^{-2} (λ_P = 347.15 nm, $\sigma_{a,P} = 1.99\times10^{-16}$ cm^2). Insertion of these parameters into Eq. 4.22 gives $\sigma_{em,eff,L} < 1.97\times10^{-17}$ cm^2 and $\sigma_{ex,L} = \sigma_{em,L} - \sigma_{em,eff,L} > 4.3\times10^{-18}$ cm^2.

4.2.3.2 Neat thin film wave-guided travelling-wave laser

The wave-guided travelling-wave laser action (wave-guided amplification of spontaneous emission) was studied using thin films of TPB and β-NPB spin-coated from a THF solution (concentration 20 mg/ml, speed 750 rpm, film thickness 262 nm for TPB; concentration 10 mg/ml, speed 750 rpm, film thickness 102 nm for β-NPB) onto microscope carrier plates (optical glass similar to Schott type BK7) and cut in the film region for optimum edge emission.

In Fig. 4.21b an edge-emitted travelling-wave laser spectral shape is shown (solid line) for TPB. A pump pulse energy density of $w_{0P} = 2.27\times10^{-4}$ J cm^{-2} was used. For comparison the shape of the fluorescence quantum distribution is included in the figure. For the β-NPB neat film, no indication of travelling wave lasing was observed up to a pump pulse energy density of 1.8×10^{-2} J cm^{-2} (no spectral narrowing, curves are not shown).

The dependences of the collected laser output energy, W_{TWL}, of the laser wavelength peak position, $\lambda_{TWL,max}$, and of the spectral halfwidth (FWHM), $\Delta\lambda_{TWL}$, on the peak input pump laser energy density, w_{0P}, are displayed in Figs. 4.23a, b, and c, respectively, for a TPB neat film

(thickness 262 nm). For β-NPB no travelling wave laser action was observed and therefore no curves are shown.

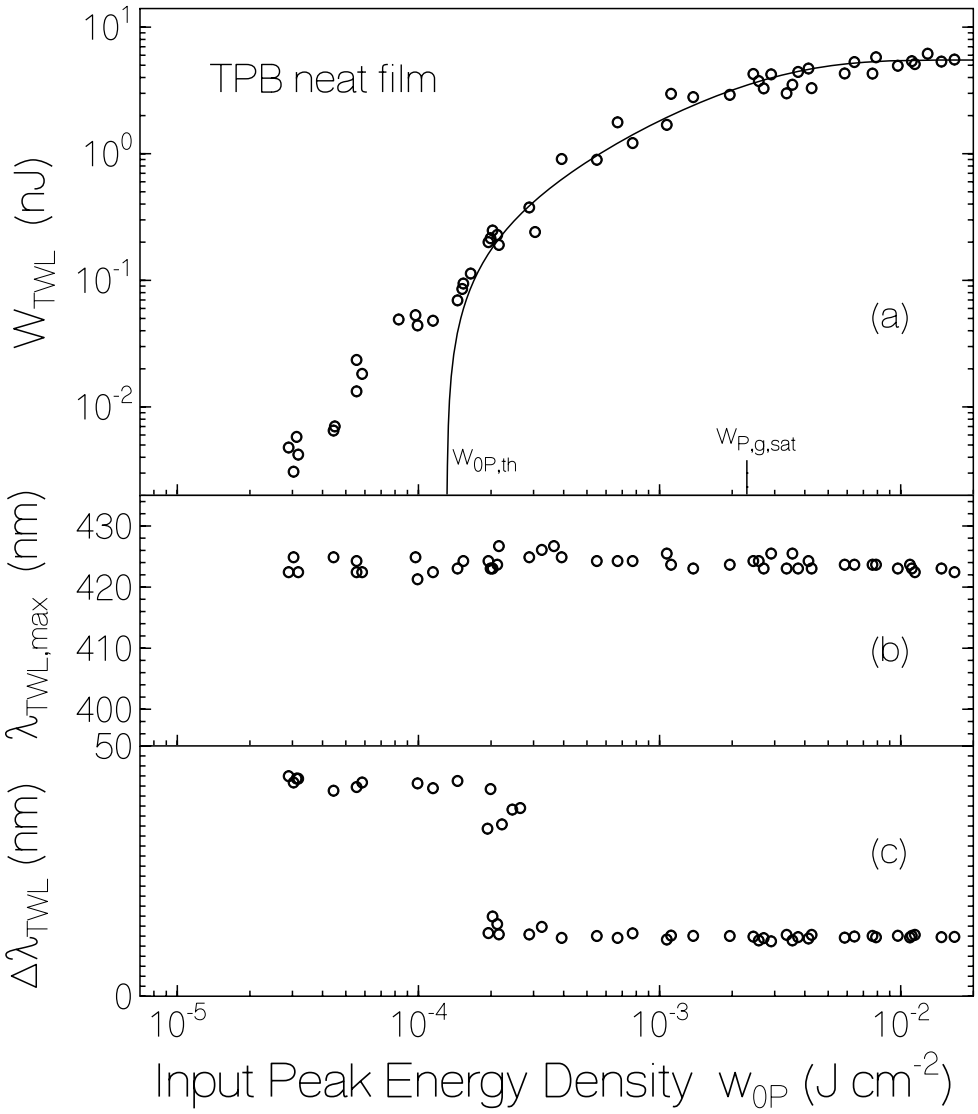

Fig. 4.23: Wave-guided travelling-wave laser performance of a TPB neat film on an optical glass substrate. Film thickness, d_f = 262 nm; pumped film area, 5 mm × 0.245 mm.
(a) Collected emission signal, W_{TWL}, versus input pump pulse energy density, w_{0P}. Full acceptance angle of fluorescence collection is $\Delta\theta$ = 0.3 rad. Curve is calculated by use of Eq. 4.23 with a pump laser threshold energy density $w_{0P,th}$ = 130 μJ cm^{-2}, a pump pulse energy density of gain saturation $w_{P,g,sat}$ = 2.3 mJ cm^{-2}, and a maximum output energy $W_{TWL,max}$ = 5.5 nJ
(b) Peak wavelength of travelling-wave laser, $\lambda_{TWL,max}$, versus input pump pulse energy density, w_{0P}.
(c) Spectral linewidth (FWHM) of travelling-wave laser, $\Delta\lambda_{TWL}$, versus input pump pulse energy density, w_{0P}.

In Fig. 4.23a, above a threshold pump pulse energy density, $w_{0P,th} \approx 1.3\times10^{-4}$ J cm^{-2}, the emission begins to rise beyond the spontaneous emission level due to stimulated emission (amplification of spontaneous emission). At high pump pulse energy density the output signal saturates to a maximum value, $W_{TWL,max} \approx 5.5$ nJ. The experimental behaviour is fitted by using the Eq. 4.23. The pump pulse energy density of gain saturation, $w_{P,g,sat} \approx 2.3\times10^{-3}$ J cm^{-2} is used. The saturation is thought to be caused by exciton-exciton annihilation processes at high densities of excited molecules [Kep96, Hol02b].

In Fig. 4.23b, the wavelength position of peak light emission, $\lambda_{TWL,max}$, is at about 424 nm independent of the excitation energy density. Its position coincides with the first vibronic sideband of the stimulated emission cross-section spectrum (Fig. 4.17a). Laser emission at the wavelength of peak stimulated emission cross-section (≈ 400 nm) is thought to be hindered by ground-state re-absorption and possibly increased excited-state absorption.

In Fig. 4.23c it is seen that the spectral halfwidth, $\Delta\lambda_{TWL}$, of the light emission shrinks around the laser threshold from a spontaneous emission line-width of $\Delta\lambda_F \approx 48$ nm to $\Delta\lambda_{TWL} \approx 15$ nm, and then remains nearly constant.

The initial laser slope efficiency, $\eta_{sl,ini}$, at threshold concerning the collected TWL light is obtained by using Eq. 4.24. A value of $\eta_{sl,ini} \approx 2\times10^{-4}$ is estimated.

In Fig. 4.24, for the investigated TPB neat film the inverse ratio of the pump laser threshold energy density, $w_{P,th,min}/w_{P,th}$, versus the excited film length, ℓ_{ap}, is presented in order to determine approximately the effective length of light amplification, ℓ_{TWL}. The constant dashed line approximates the behaviour for pumped lengths longer than the effective gain length, and the dash-dotted line is a guide line for the situation of pump lengths shorter than the effective gain

length. From the crossing point of the lines one obtains $\ell_{TWL} \approx 2.2$ mm. If the gain length is limited by ground-state tail absorption, $\alpha(\lambda_{TWL,max})$, at the peak laser wavelength, $\lambda_{TWL,max} \approx 424$ nm, then it is $\alpha(424\text{ nm}) \approx \ell_{TWL}^{-1} \approx 4.55$ cm^{-1} and the absorption cross-section is $\sigma_a(424\text{ nm}) = \alpha(424\text{nm})/N_f \approx 3.25\times10^{-21}$ cm^2.

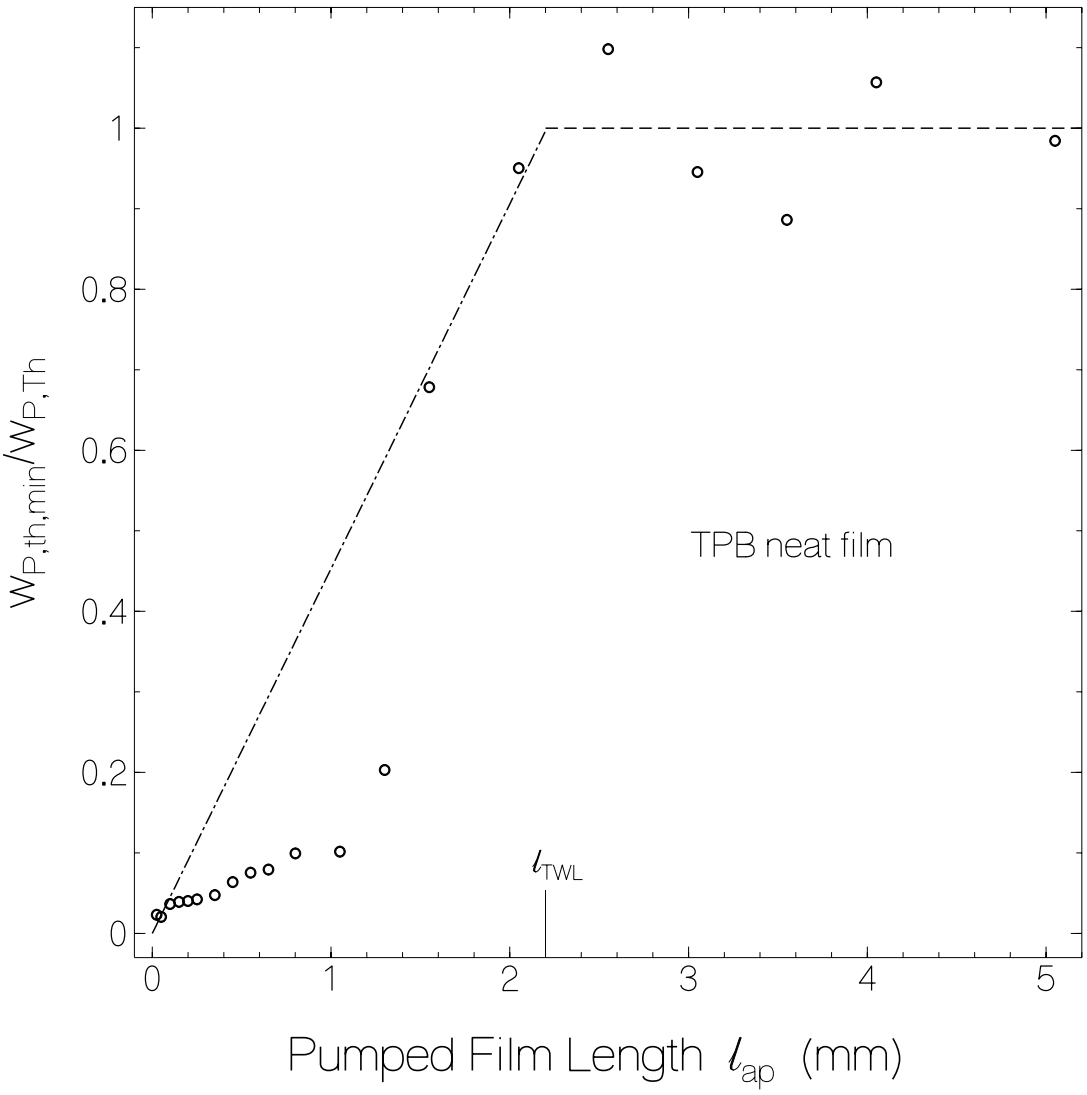

Fig. 4.24: Inverse laser threshold pump pulse energy density, $w_{0P,th}^{-1}$, versus exposed film length, ℓ_{ap}. The crossing of the dashed and the dash-dotted guide-lines determines the effective gain length, ℓ_{TWL}. Film thickness, $d_f = 262$ nm.

4.2.4 Conclusions

For the light-emitting hole-transport materials TPB (N,N,N',N'-tetraphenylbenzidine) and β-NPB (N,N'-bis(2-naphtalenyl)-N,N'-bis(phenylbenzidine) relatively high fluorescence quantum yields were obtained. The determined efficiencies are ϕ(TPB/THF) = 0.73, ϕ(β-NPB/THF) = 0.28, ϕ(TPB neat film) = 0.36 and ϕ(β-NPB neat film) = 0.215. The peak stimulated emission cross-section of β-NPB, σ_{em}(428 nm) = 2.44×10^{-17} $cm^2$was found to be approximately a factor of ten smaller than the peak stimulated emission cross-section of TPB, σ_{em}(411 nm) = 2.97×10^{-16}. The substitution of phenyl groups by naphthalene groups caused the formation of a low lying weakly absorbing state (S_1-state) with long radiative lifetime and small stimulated emission cross-section. Laser action was achieved for TPB both in tetrahydrofuran solution and as neat film. No laser action was achieved for β-NPB because of its low stimulated emission cross-section spectrum and due to the dominance of excited-state absorption.

The performed studies showed that the triphenylamine dimer TPB, similar as its methyl derivatives 3-methyl-TPD [Hol00] and 4-methyl-TPD [Phi03], is a good violet laser dye both in liquid solution as well as in the neat solid state. Besides its application as hole-transport material in organic light emitting devices TPB may find application in violet liquid dye lasers and solid-state integrated-optics laser devices.

4.3 Triphenylamine (TPA) and tris-3 methyl- triphenylamine (m-MTDAB)

The molecule triphenylamine (TPA) and derivatives thereof are applied as hole transport materials in electrophotography [Bro78, Abk86], and in organic light emitting diodes [Tan89, Van96]. They are used in the backbone [Nom04, The02] or in side-groups [Kol96, Liu00] of polymers applied in light emitting diodes. Laser action was also achieved on triphenylamine based conjugated polymers [Hol01c] and triphenylamine-dimer based conjugated and non-conjugated polymers [Hol02].

Star-shaped oligomers and dendritic structures of triphenylamines are attractive photo- and electro-active organic materials because of their amorphous nature [The02, Shi05]. Methyl-substituted derivatives of the starburst molecule, 1,3,5-tris(diphenylamino)benzene (TDAB) belong to low-molecular-mass organic materials which form stable amorphous glasses with glass transition temperatures above room temperature [Ish91, Ish93]. 1,3,5-tris(3-methylphenylphenylamino)benzene (m-MTDAB) has stable amorphous glass properties below 49 °C, it crystallizes at about 88 °C, and melts at 183 °C [Ish93]. Its synthesis is described in [Ish91]. It is used as hole-transport material in light emitting devices.

Here triphenylamine (TPA) dissolved in tetrahydrofuran (THF) and m-MTDAB dissolved in (THF) and as neat thin film are characterized by absorption and emission spectroscopy. Absorption cross-section spectra, stimulated emission cross-section spectra, fluorescence quantum distributions, fluorescence quantum yields, degrees of fluorescence polarisation, and fluorescence lifetimes are determined. The nonlinear transmission behaviour of the samples at the second harmonic of a picosecond ruby laser is studied and the responsible excited-state absorption cross-section is extracted. The amplification or attenuation of spontaneous emission

(ASE) is investigated by transverse sample pumping with second harmonic pulses of a mode-locked ruby laser in order to check the lasing ability of these materials and to determine the excited-state absorption cross-section spectra of the samples in the fluorescence spectral region.

4.3.1 Optical and spectroscopic characterization

The reflectance and transmittance spectra of a neat thin film of starburst triphenylamine oligomer m-MTDAB on a fused silica substrate are shown in Fig. 4.25 (solid curves). The thin film was prepared by spin-coating of m-MTDAB THF solution of dye concentration 10 mg/ml at a speed of 450 rpm. The dashed curves in Fig. 4.25 show the reflectance and transmittance curves of the fused silica substrate. The fitting of the experimental spectra to the Fresnel laws of reflection and transmission allows the determination of the optical constants $n(\lambda)$ (refractive index spectrum) and $\alpha(\lambda)$ (absorption coefficient spectrum) and the film thickness d_f [Pen98, Hol99]. The optical constants spectra are shown in Fig. 4.26. The film thickness turned out to be d_f = 52 nm. The absorption maximum occurs slightly below 316 nm (limit of experimental measurement range). At 316 nm wavelength the light penetration depth is $d_p = \alpha_f^{-1}$ = 52.5 nm. The refractive index spectrum shows the expected dispersion shape. Therefore the optical wave-guiding takes place in films above a critical film thickness [Kog79]. At λ =400 nm minimum wave-guiding thicknesses of $d_{min,TE}$ = 63.5 nm by Eq. 4.1a and $d_{min,TM}$ = 97.4 nm by Eq. 4.1b are calculated (n_f = 1.7677, n_s = 1.47024).

For triphenylamine (TPA) molecule no good films could be made by spin-coating because of crystallisation.

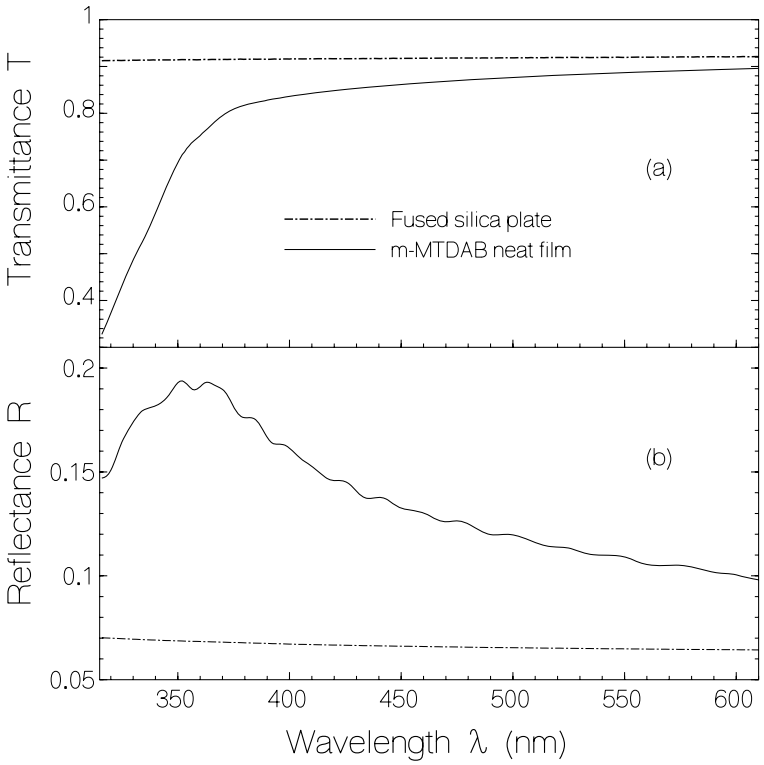

Fig. 4.25: (a) Transmittance, $T(\lambda)$, and (b) reflectance, $R(\lambda)$, spectra of a m-MTDAB neat film on a fused silica substrate. Dotted lines belong to blank fused silica.

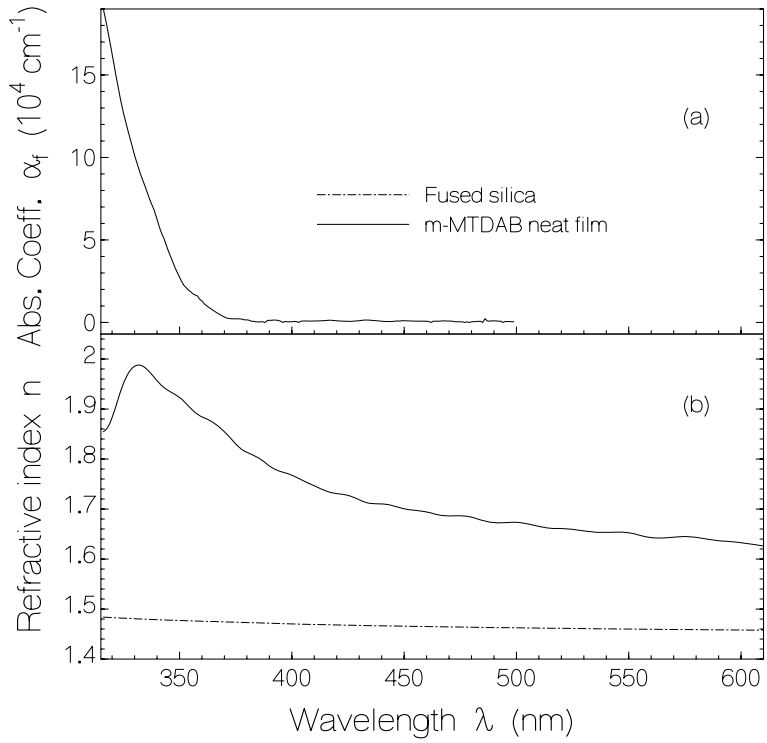

Fig. 4.26:(a) Absorption coefficient spectra, $\alpha_f(\lambda)$, and (b) refractive index, $n(\lambda)$, spectra of m-MTDAB neat film(thickness $d_f = 52$ nm) and fused silica substrate.

The absorption cross-section spectra, $\sigma_a(\lambda)$, of TPA, m-MTDAB in THF and of m-MTDAB neat film are displayed in Fig. 4.27. The neat film curve is calculated assuming the same S_0-S_1 absorption cross-section integral for the solution and the film. The film absorption cross-section

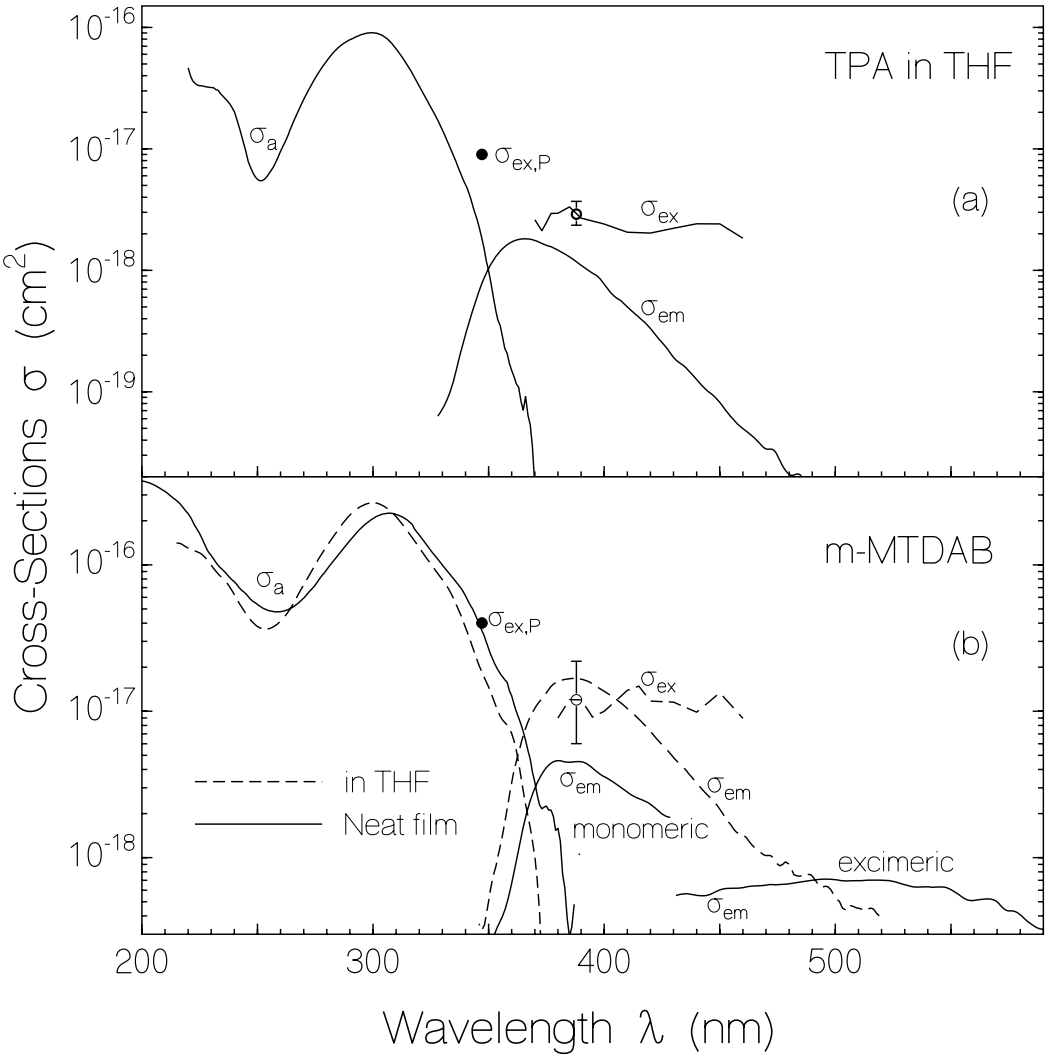

Fig. 4.27: Absorption cross-section, $\sigma_a(\lambda)$, stimulated emission cross-section, $\sigma_{em}(\lambda)$, and excited-state absorption cross-section spectra, $\sigma_{ex}(\lambda)$. Dots show excited-state absorption cross-sections of THF solutions at pump laser wavelength λ_P =347.15 nm.
(a) TPA in tetrahydrofuran (THF).
(b) m-MTDAB neat film and m-MTDAB in THF

spectrum below 316 nm was obtained by transmission measurement relative to a blank fused silica plate. TPA/THF absorption spectrum has peak at 300 nm. The dye m-MTDAB/THF also

has its absorption maximum at 300 nm. The peak absorption of the m-MTDAB film is at 307 nm. The m-MTDAB molecule number density in the film is estimated to be $N_f = \alpha_f / \sigma_{a,f} \approx 8.43\times10^{20}$ cm^{-3} (calculated at λ = 316 nm). The mass density, ρ, of the m-MTDAB neat thin films is determined to be $\rho = (N_f / N_A) M_m \approx 0.874$ g cm^{-3}, where N_A is the Avogadro constant and M_m =621.83 g mol^{-1} is the molar mass.

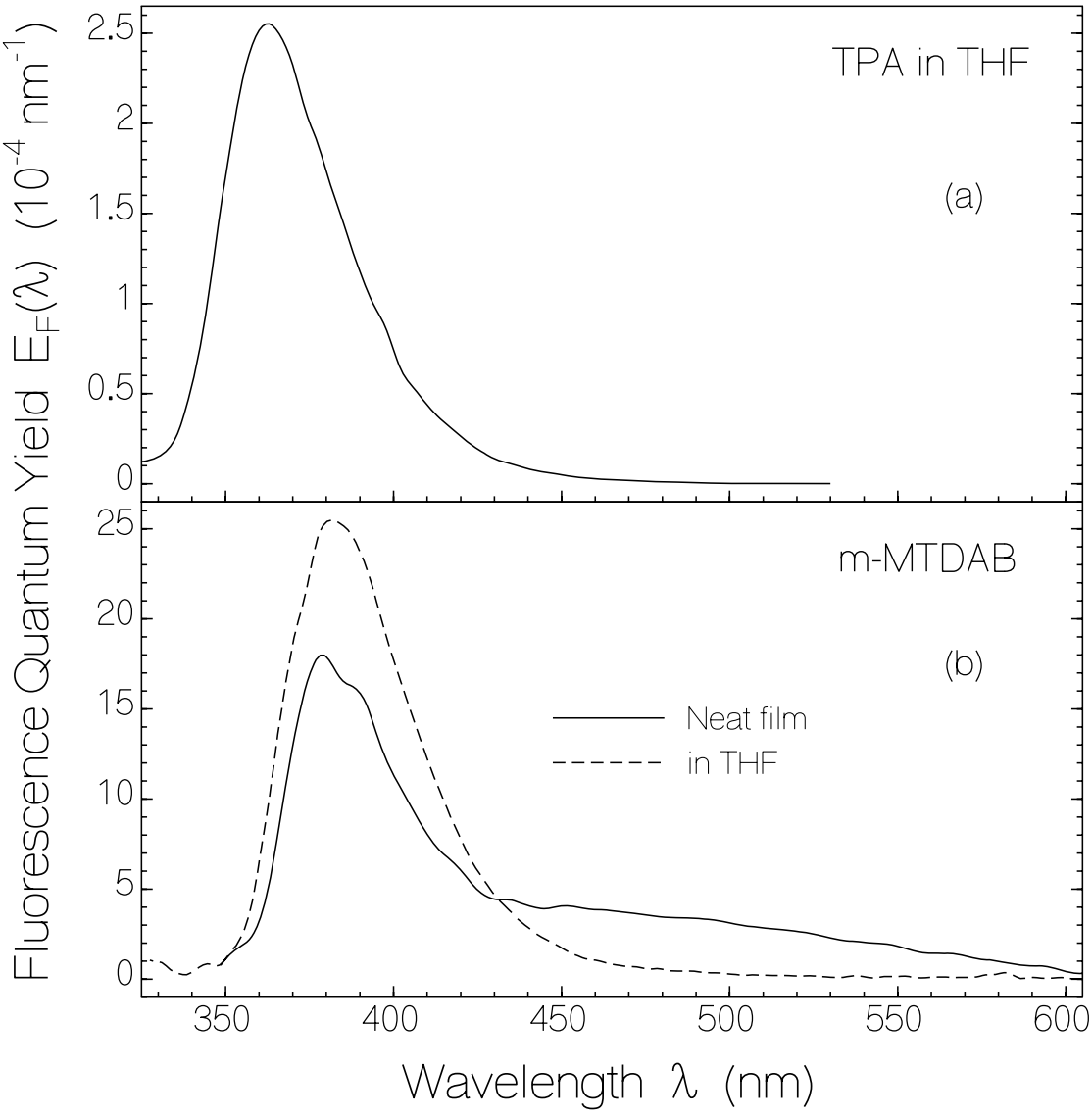

Fig. 4.28: Fluorescence quantum distributions, $E_F(\lambda)$, of (a) 4×10^{-5} molar TPA in THF, and of (b) 5×10^{-4} molar m-MTDAB in THF and m-MTDAB neat film. Excitation wavelength: 311 nm.

The fluorescence quantum distributions, $E_F(\lambda)$, of TPA in THF and of m-MTDAB in THF and as neat film are shown in Fig. 4.28a and 4.28b, respectively. The fluorescence quantum yields, (Eq. 3.5) $\phi_F = \int E_F(\lambda) d\lambda$, are ϕ_F(TPA/THF) = 0.012±0.001, ϕ_F(m-MTDAB/THF) = 0.128±0.005, and ϕ_F(m-MTDAB neat film) = 0.123±0.005. The fluorescence efficiency of TPA in solution is rather low. Some rotation freedom of the phenyl groups may cause non-radiative decay by internal conversion [Amo87, Val02]. The starburst molecule m-MTDAB seems to be more rigid giving lower non-radiative decay. The m-MTDAB film shows a short-wavelength monomeric emission similar to the solution emission (peak at 379 nm) and a long-wavelength broad-band excimeric emission (peak at 450 nm, excited-state charge re-distribution over more than one molecule, bound complex formation in the excited state [Val02]). The fluorescence efficiency of the neat film is composed of monomeric and excimeric contribution, i.e. ϕ_F(m-MTDAB neat film) = $\phi_{F,M} + \phi_{F,Ex}$, with $\phi_{F,M} \approx 0.082$, and $\phi_{F,Ex} \approx 0.041$.

The degrees of fluorescence polarisation, P_F, were measured to be 0.035±0.005 for TPA in THF, and 0.055±0.005 for m-MTDAB in THF. For isotropic media with parallel orientation of the absorption and emission transition dipole moments, P_F approaches 0.5 if there occurs no reorientation within the fluorescence lifetime; and P_F approaches 0 if complete reorientation occurs within the fluorescence lifetime [Lak83].

Temporal fluorescence signals of a 1.5×10^{-3} molar solution of TPA in THF (a), of a 4.7×10^{-5} molar solution of m-MTDAB in THF (b), and of a m-MTDAB neat film (c) at 407 nm (monomeric part, thin solid curve) and at 500 nm (excimeric part, thick sold cure) are shown in Fig. 4.29. The dotted curves show the detection system response function (attenuated pump pulses directed to micro-channel-plate photomultiplier). Single-exponential fluorescence-decays are fitted to the fluorescence decay parts (dash-dotted curves.). The obtained fluorescence

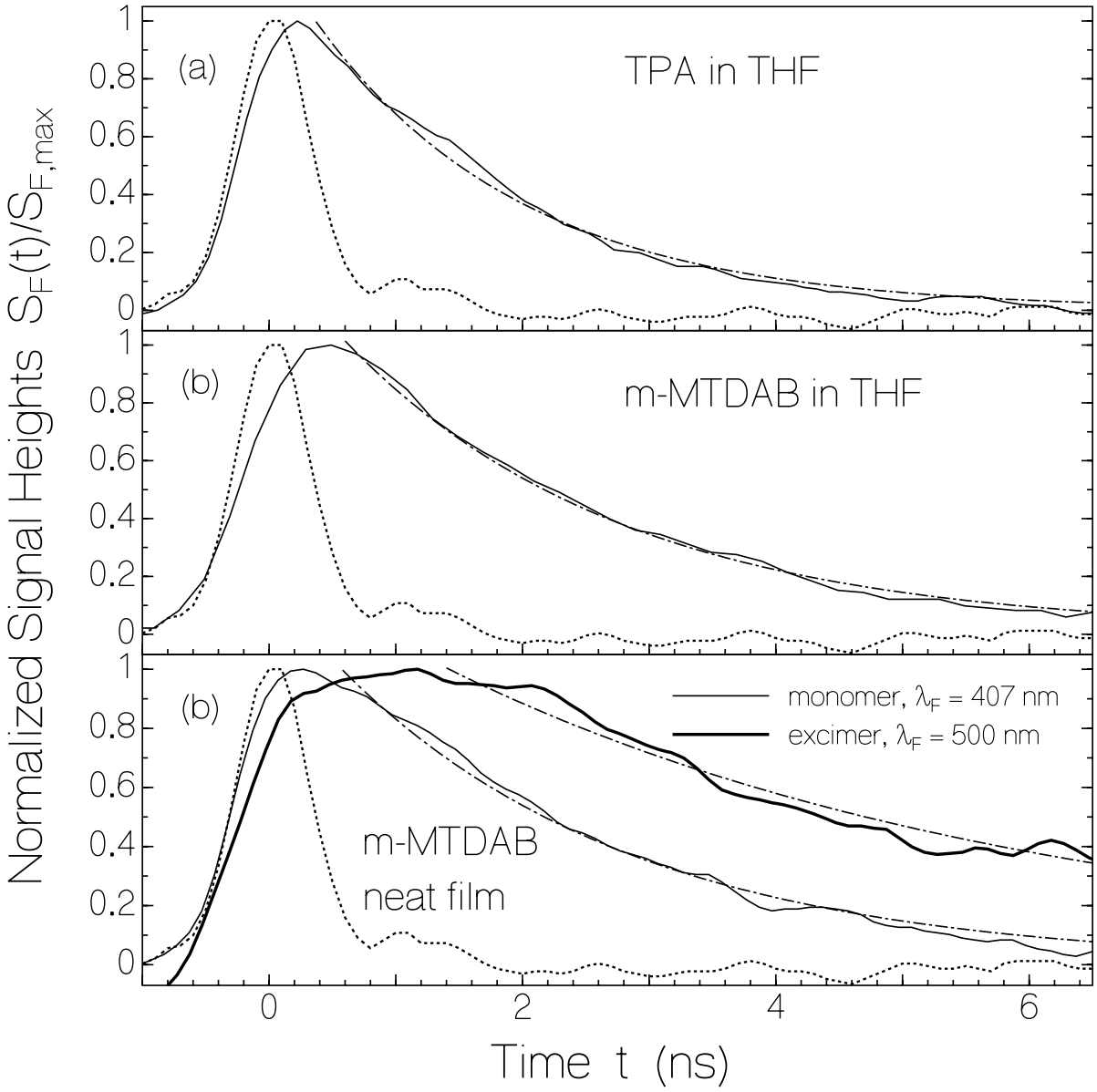

Fig. 4.29: Temporal fluorescence traces. Excitation with second harmonic pulses of mode-locked ruby laser (duration Δt_P = 35 ps, wavelength λ_P = 347.15 nm). Dotted curves show response function of detection system. Dash-dotted curves display single-exponential regression fits, $S_F(t) = S_{F,0} \exp[-(t-t_0)/\tau_F]$, where t_0 is the temporal start position of fitting.

(a) TPA in THF. Concentration $C = 1.5\times10^{-3}$mol dm^{-3}. Fluorescence detection at λ_{obs} = 407 nm (spectral width 10 nm). Fluorescence lifetime: τ_F = 1.63 ns.

(b) m-MTDAB in THF. $C = 4.7\times10^{-5}$ mol dm^{-3}, λ_{obs} = 407 nm, τ_F = 2.2 ns.

(c) m-MTDAB neat film of thickness d_f = 335 nm. Thin solid curve: λ_{obs} = 407 nm, τ_F = 2.3 ns (monomeric emission). Thick solid curve: λ_{obs} = 500 nm (spectral width 4.4 nm), τ_F = 4.66 ns (excimeric emission).

lifetimes are τ_F(TPA/THF) = 1.63 ns, τ_F(m-MTDAB/THF) = 2.19 ns, τ_F(m-MTDAB neat film, monomeric) = $\tau_{F,M}$ = 2.3 ns, and τ_F(m-MTDAB neat film, excimeric) = $\tau_{F,Ex}$ = 4.66 ns,. During the short-wavelength component emission ($\tau_{F,M}$) the fluorescence of the long-component emission builds up and decays with a slower decay time ($\tau_{F,Ex}$) (exited-state excimer formation within excited monomer lifetime).

The radiative lifetime, τ_{rad}, may be determined from the fluorescence lifetime, τ_F, and the fluorescence quantum yield, ϕ_F, according to Eq. 4.5. The experimental results are τ_{rad}(TPA/THF) ≈ 136 ns and τ_{rad}(m-MTDAB/THF) ≈ 17.2 ns.

For the m-MTDAB neat film the situation is more complex. The following reaction scheme 1 is expected.

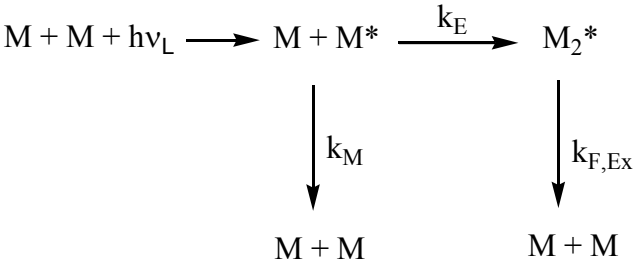

(Scheme 1)

A corresponding energy level scheme is shown in Fig. 4.30. Level 1 considers two monomers, M + M, in the ground-state. Level 2 describes the situation immediately after excitation of one monomer, M* + M. Level 3 considers the formed excimer, M_2*. Finally level 4 describes the unstable ground-state dimer, M_2, which separates back to two monomers, M + M. After excitation the relevant relaxation dynamics is described by

$$\frac{dN_2}{dt} = -(k_M + k_E)N_2\,, \tag{4.30a}$$

$$\frac{dN_3}{dt} = k_E N_2 - k_{F,Ex} N_3\,. \tag{4.30b}$$

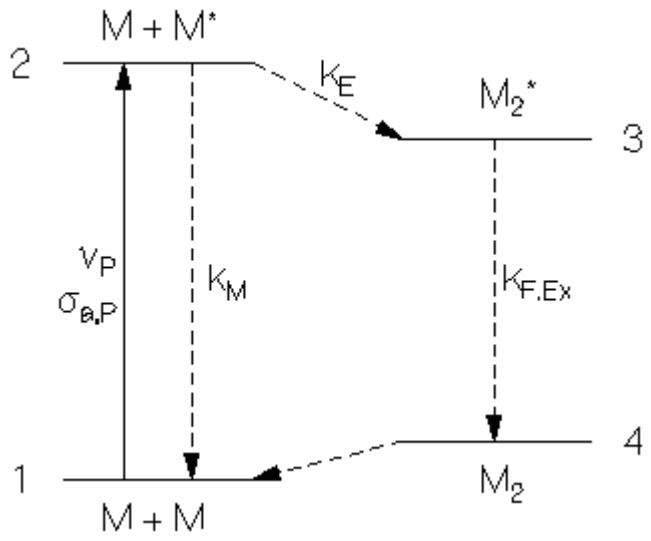

Fig. 4.30: Level scheme illustration of photo-induced excited-state dimer formation, and monomeric and excimeric light emission.

k_M is the monomeric decay rate to the ground-state. k_E is the transfer rate to the excimeric form. $k_{F,2} = k_M + k_E = \tau_{F,M}^{-1}$ is the monomeric fluorescence rate. $k_{F,3} = \tau_{F,Ex}^{-1}$ is the excimeric fluorescence rate. The solution of the equation system 4.30a is

$$N_2(t) = N_{2,0} \exp\left(-t/\tau_{F,M}\right), \tag{4.31a}$$

and the solution of Eq. 4.30b (linear inhomogeneous differential equation) gives

$$N_3(t) = N_{2,0} \frac{k_E}{\tau_{F,M}^{-1} - \tau_{F,Ex}^{-1}} \left[\exp\left(-t/\tau_{F,Ex}\right) - \exp\left(-t/\tau_{F,M}\right)\right]. \tag{4.31b}$$

The total fluorescence quantum yield, ϕ_F, is composed of a monomeric contribution and a excimeric contribution

$$\phi_F = \phi_{F,M} + \phi_{F,Ex}\,. \tag{4.32}$$

These contributions are

$$\phi_{F.M} = \frac{k_{rad,M} \int_0^\infty N_2(t)dt}{N_{2,0}} = k_{rad,M}\tau_{F,M} = \frac{\tau_{F.M}}{\tau_{rad,M}}, \tag{4.33a}$$

$$\phi_{F.Ex} = \frac{k_{rad,Ex}\int_0^\infty N_3(t)dt}{N_{2,0}} = k_{rad,Ex}\frac{k_E}{\tau_{F,M}^{-1} - \tau_{F,Ex}^{-1}}\left(\tau_{F,Ex} - \tau_{F,M}\right) = k_{rad,Ex}k_E\tau_{F,M}\tau_{F,Ex} = \frac{k_E\tau_{F,M}\tau_{F,Ex}}{\tau_{rad,Ex}}$$

(4.33b)

with the monomeric radiative $\tau_{rad,M}$, and the excimeric radiative lifetime $\tau_{rad,Ex}$. Approximating k_M in $k_{F,M} = k_M + k_E = \tau_{F,M}^{-1}$ by $k_M = k_{rad,M} = \tau_{rad,M}^{-1}$ gives $k_E = \tau_{F,M}^{-1} - \tau_{rad,M}^{-1} = (\phi_{F,M}^{-1} - 1)\tau_{rad,M}^{-1}$. Insertion into Eq. 4.33b gives

$$\phi_{F,Ex} \approx \frac{(\phi_{F,M}^{-1} - 1)\tau_{F,M}\tau_{F,Ex}}{\tau_{rad,M}\tau_{rad,Ex}} = \frac{(\phi_{F,M}^{-1} - 1)\phi_{F,M}\tau_{F,Ex}}{\tau_{rad,Ex}} = (1 - \phi_{F,M})\frac{\tau_{F,Ex}}{\tau_{rad,Ex}}, \quad (4.34a)$$

and

$$\tau_{rad,Ex} \approx \frac{1 - \phi_{F,M}}{\phi_{F,ex}}\tau_{F,Ex}. \quad (4.34b)$$

Using the experimental parameters, $\tau_{F,M}$ = 2.3 ns and $\phi_{F,M}$ = 0.082, gives $\tau_{rad,M} = \tau_{F,M}\phi_{F,M}^{-1}$ = $\tau_{rad,M} \approx$ 28 ns. The parameters for the excimeric contribution are $\tau_{F,Ex}$ = 4.66 ns and $\phi_{F,Ex}$ = 0.041, giving $\tau_{rad,ex} \approx$ 104 ns.

The reorientation time, τ_{or}, of the emission transition dipole moments may be extracted from the degree of fluorescence polarisation, P_F, by the relation Eq. 4.4, For TPA in THF it is $P_F \approx$ 0.035 and τ_F = 1.63 ns giving $\tau_{or} \approx$ 100 ps. For m-MTDAB in THF the parameters are $P_F \approx$ 0.065 and τ_F = 2.19 ns giving $\tau_{or} \approx$ 270 ps. In the solutions the transition dipole moment reorientation is determined by molecular reorientation.

The stimulated emission cross-section spectra, $\sigma_{em}(\lambda)$, of the investigated molecules may be determined by the Einstein relation Eq. 4.3. The calculated stimulated emission cross-section spectra are included in Fig. 4.27. From the Einstein relation between absorption and emission it is

known that the S_0-S_1 absorption cross-section integral, $\int \sigma_a(\nu) d\nu$, is about the same as the stimulated emission cross-section integral, $\int \sigma_{em}(\nu) d\nu$, and the S_0-S_1 absorption cross-section spectrum and the S_1-S_0 emission cross-section spectrum are mirror symmetric. This shows that for both TPA and m-MTDAB the S_0-S_1 transitions are only weakly allowed, their absorption bands are located in the long-wavelength absorption tails of the molecules and their shapes are hidden in the stronger absorbing S_0-S_n absorption bands ($n \geq 2$). For m-MTDAB in solid state the monomeric S_1-S_0 and the excimeric S_1-S_0 stimulated emission cross-section spectra are extracted. The emission cross-section intergral for the molecules in mommeric state is roughly a factor of two larger than for the molecules in excimeric state.

4.3.2 Reverse saturable absorption behaviour

The experimental energy transmissions, T_E, of second harmonic picosecond ruby laser pulses (duration Δt_P = 35 ps, wavelength λ_P = 347.15 nm) through 1 mm cells filled with either TPA or m-MTDAB in THF as a function of the input peak pulse intensity, I_{0P}, are shown by circles in Fig. 4.31. The transmissions decrease from the small-signal transmission of T_0(TPA) = 0.157 and T_0(m-MTDAB) = 0.12 at low excitation intensity to T_E(TPA) ≈ 0.073 and T_E(m-MTDAB) ≈ 0.042 at excitation intensity $I_{0P} = 2.5 \times 10^{10}$ W cm^{-2}. One speaks of saturable absorption if the transmission rises with excitation intensity [Her67, Pen88] and of reverse or inverse saturable absorption if the transmission decreases with rising intensity [Tut93, Jos98]. Reverse saturable absorption is applied for optical limiting [Jos98]. The solid curves in Fig. 4.31 are numerical simulations to the transmission measurements. The differential equation system for the intensity dependent pump pulse transmission is given in [Hol00b] and are (Eqs. 4.6 - 4.13) shown above. For the solid curves in Fig. 4.31 the excited-state absorption cross-section is varied. The best fit

to the experimental data is obtained for $\sigma_{ex,P}$(TPA) = 9×10^{-18} cm^2 and $\sigma_{ex,P}$(m-MTDAB) = 4×10^{-17} cm^2. The ground-state absorption cross-sections are $\sigma_{a,p}$(TPA) = 1.85×10^{-18} cm^2 and $\sigma_{a,P}$(m-MTDAB) = 1.86×10^{-17} cm^2. The slow-absorber ground-state depletion saturation intensities, $I_{P,sat} = h\nu_P/(\sigma_{a,P}\Delta t_P)$, for TPA and m-MTDAB in THF are indicated in Fig. 4.31.

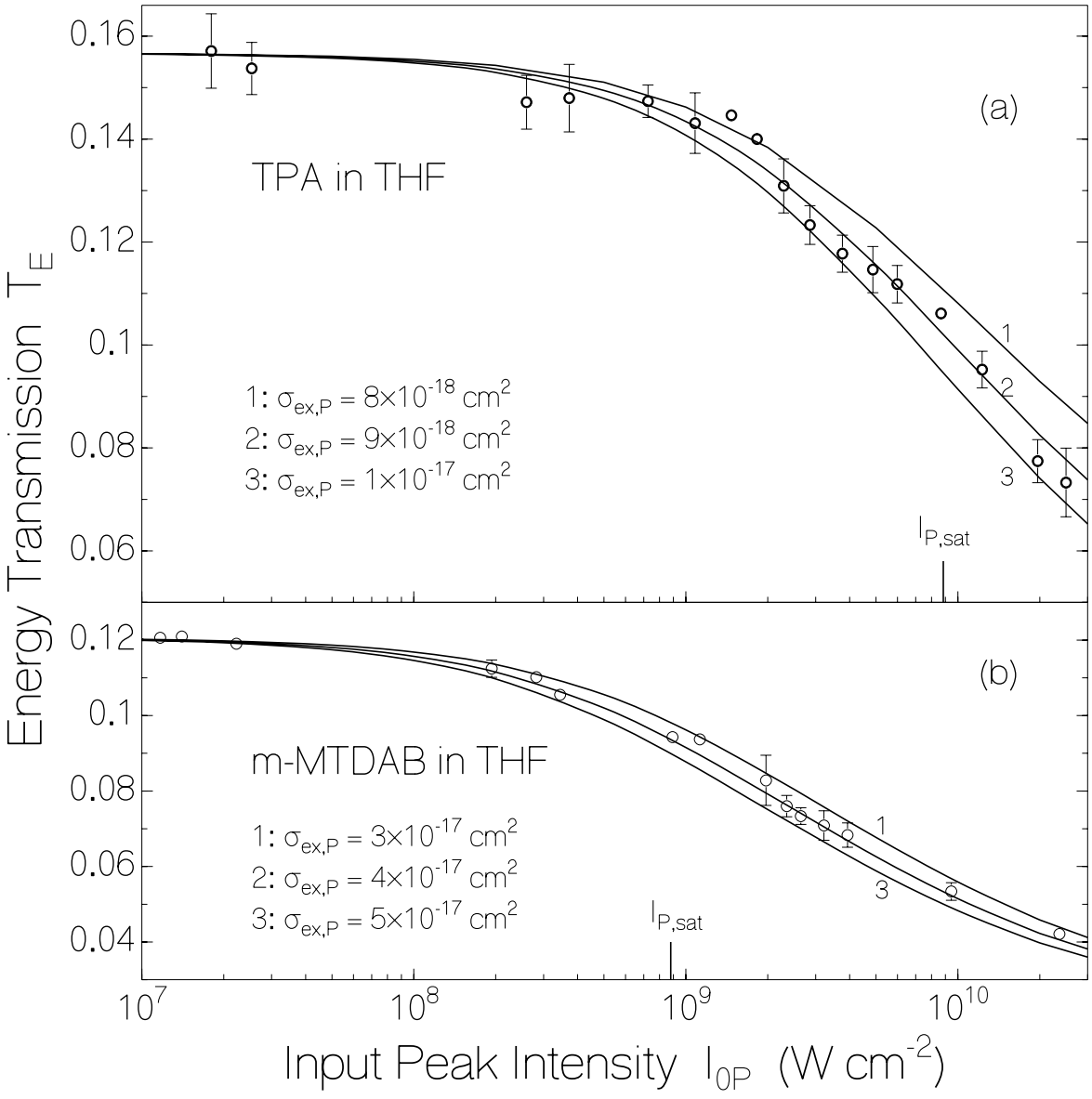

Fig. 4.31: Reverse saturable absorption behaviour of TPA (a) and m-MTDAB (b) in THF. Circles are measured. Curves are calculated using excited-state absorption cross-sections $\sigma_{ex,P}$ listed in the figure. Pump laser pulses: second harmonic of picosecond ruby laser (wavelength 347.15 nm, duration 35 ps FWHM). $I_{P,sat}$, of ground-state population depletion is indicated.

4.3.3 Attenuation and amplification of spontaneous emission

TPA/THF and m-MTDAB/THF solutions in a 1 cm × 1 mm fused silica dye-laser cell and a neat film of m-MTDAB on an optical glass substrate were transverse pumped and the attenuation/amplification of the spontaneous emission along the pumped region was studied by measuring the output light along the line-focus direction perpendicular to the pump pulse propagation direction.

The obtained emission output spectra are shown in Fig. 4.32a, b, and c for 2.25×10^{-2} molar TPA in THF, 1.52×10^{-3} molar m-MTDAB in THF, and a 725 nm thick m-MTDAB neat film (exposed length 5 mm), respectively. The emitted light from the solution is collected within an acceptance angle of 0.82°. For the edge emission from the wave-guided film an acceptance angle of 0.3 rad was used. For the liquid solutions no change in the spectral shape is observed for the different pump pulse energy densities. For the neat film some spectral changes with excitation energy density are seen.

The dependence of the collected output energy on the input pump pulse energy density is shown in Fig. 4.33 for TPA in THF (a), and m-MTDAB in THF (b). The slow-absorption ground-state depletion saturation energy densities, Eq. 4.16 $w_{P,sat} = h\nu_P / \sigma_{a,P}$, [Pen91, Pen92] are indicated. The rise of the output energy with pump pulse energy density in the absence of any attenuation or amplification, $W_{\mathrm{ASE,no}}$, is shown by the dash-dotted curves in Fig. 4.33. They are given by

$$W_{ASE,no} = W_{ASE,0}\frac{1-\exp\left(-w_{0P}/w_{P,sat}\right)}{1-\exp\left(-w_{0P,0}/w_{P,sat}\right)} \tag{4.35}$$

where $W_{\mathrm{ASE,0}}$ is the output energy at the lowest applied excitation energy density $w_{\mathrm{0P,0}}$. In the case of TPA in THF the measured output energy is lower than $W_{\mathrm{ASE,no}}$ indicating attenuation of

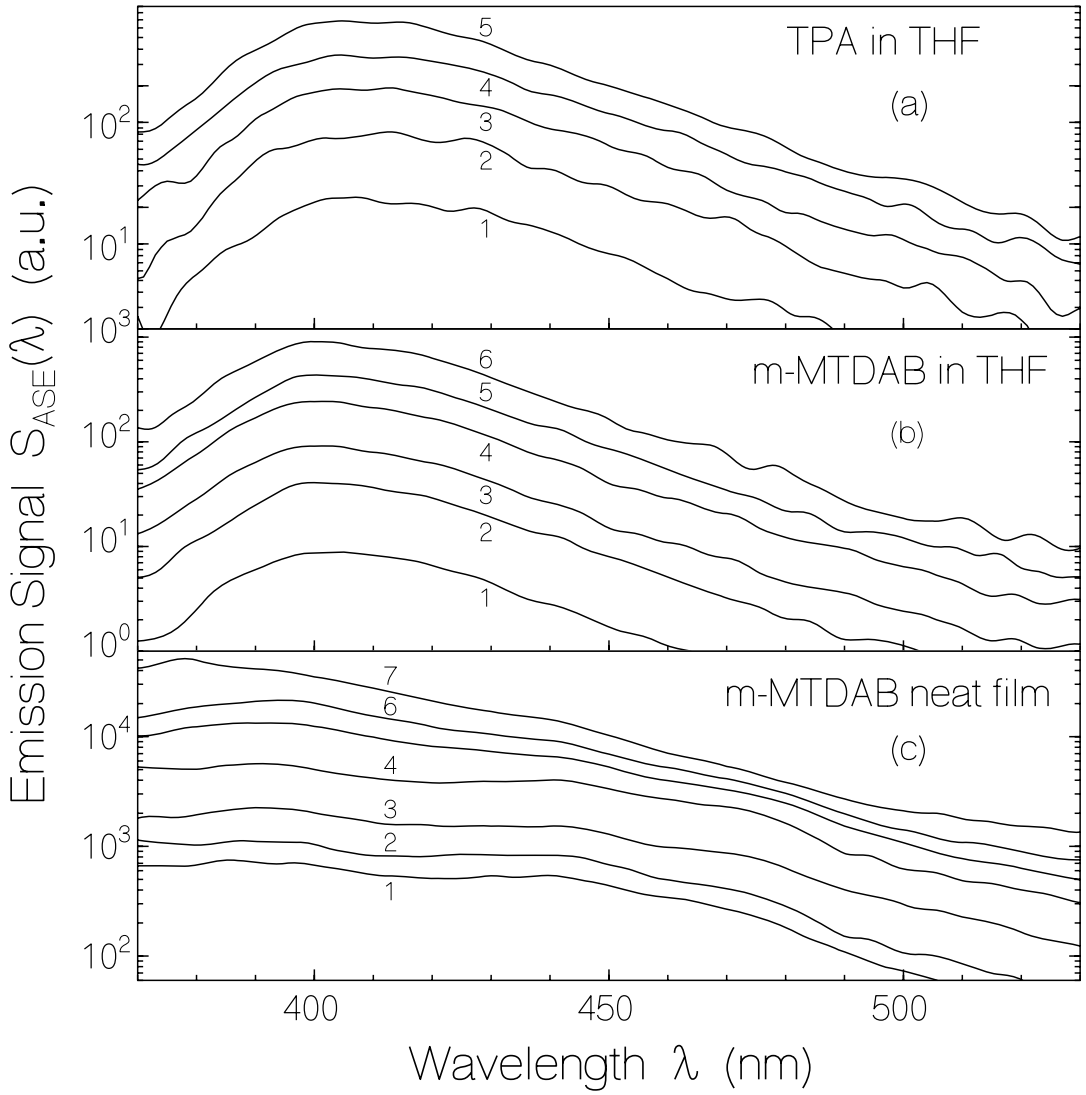

Fig. 4.32 Emission spectra of picosecond pump pulse excited samples (excitation wavelength λ_P = 347.15 nm, pulse duration Δt_P = 35 ps, pump pulse beam profile: 14.5 mm × 0.254 nm) for various pump pulse excitation energy densities, w_{0P}, (amplification or attenuation of spontaneous emission).

(a) Transverse pumped 0.0225 molar TPA in THF in 1 cm × 1 mm cell. Full collection angle: 0.82°. The curves belong to w_{0P} = 0.77 mJ cm^{-2} (1), 3.07 mJ cm^{-2} (2), 9.09 mJ cm^{-2} (3), 28.5 mJ cm^{-2} (4), and 75.1 mJ cm^{-2} (5).

(b) Transverse pumped 1.52×10^{-3} molar m-MTDAB in THF in 1 cm × 1 mm cell. Full collection angle: 0.82°. The curves belong to w_{0P} = 0.27 mJ cm^{-2} (1), 1.28 mJ cm^{-2} (2), 2.84 mJ cm^{-2} (3), 9.69 mJ cm^{-2} (4), 19.6 mJ cm^{-2} (5), and 49.88 mJ cm^{-2} (5).

(c) Transverse pumped m-MTDAB neat film. Film thickness: 725 nm. Length of film exposed: 5 mm. Full collection angle of edge-emitted light: 0.3 rad. The curves belong to w_{0P} = 0.0622 mJ cm^{-2} (1), 0.115 mJ cm^{-2} (2), 0.294 mJ cm^{-2} (3), 0.67 mJ cm^{-2} (4), 1.75 mJ cm^{-2} (5), 3.14 mJ cm^{-2} (6), and 17.3 mJ cm^{-2}.

spontaneous emission due to excited-state absorption larger than stimulated emission. In the case of m-MTDAB in THF the measured output energy practically coincides with $W_{ASE,no}$ indicating no, over the spectrum integrated, attenuation or amplification of spontaneous emission. For the investigated m-MTDAB neat film the output emission is displayed separately for the monomeric

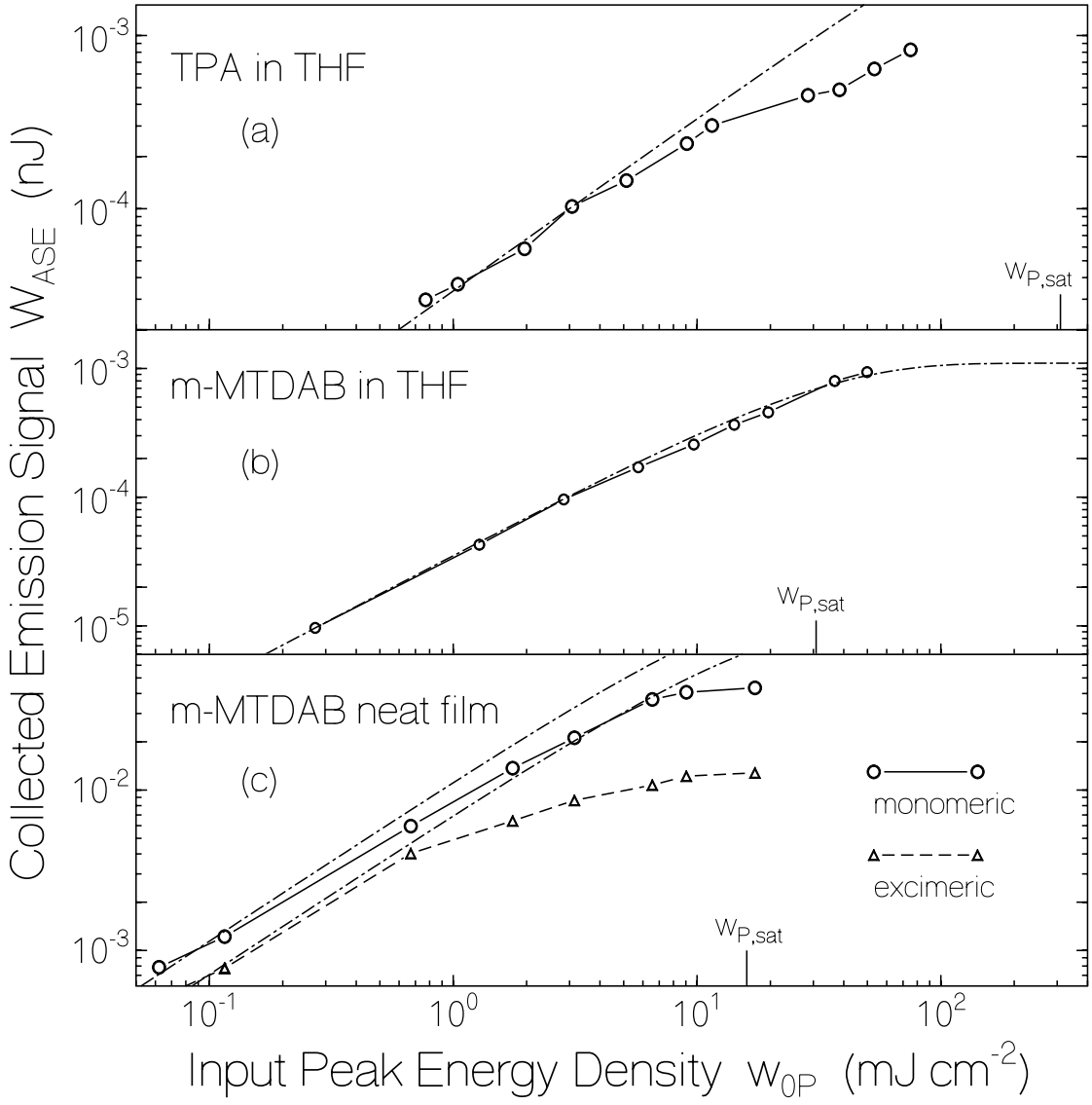

Fig. 4.33: Collected attenuated or amplified spontaneous emission energy, W_{ASE}, versus pump pulse excitation energy, w_{0P}. The same experimental conditions apply as in Fig. 4.32. The dash-dotted lines show the expected dependence in absence of attenuation or amplification of the spontaneous emission (Eq. 4.35).
(a) TPA in THF, (b) m-MTDAB in THF and(c) m-MTDAB neat film.

emission and the excimeric emission. In both cases at high excitation it is $W_{ASE} < W_{ASE,no}$ showing that the excited-state absorption is larger than the stimulated emission with larger difference for the excimeric form than for the monomeric form.

In Fig. 4.34 the attenuation or amplification,

$$A(\lambda) = \frac{S_{ASE}(\lambda)/N_{ex,0}(w_{0P})}{S_{sp}(\lambda)/N_{ex,0}(w_{0P,sp})} = \frac{S_{ASE}(\lambda)\left[1-\exp\left(-w_{0P,sp}/w_{P,sat}\right)\right]}{S_{sp}(\lambda)\left[1-\exp\left(-w_{0P}/w_{P,sat}\right)\right]} \tag{4.36}$$

of the spontaneous emission for several pump pulse energy densities is displayed. Thereby $N_{ex,0}$ is the initial emission-state population number density. It is given by Eq. 4.15.

$$N_{ex,0} = N_0\left[1-\exp\left(-\frac{w_{0P}}{w_{P,sat}}\right)\right]. \tag{4.37a}$$

For $w_{0P} << w_{P,sat}$ one obtains

$$N_{ex,0} = N_0\frac{w_{0P}}{w_{P,sat}} = \frac{N_0\sigma_{a,P}w_{0P}}{h\nu_P} = \frac{\alpha_{P,0}w_{0P}}{h\nu_P}, \tag{4.37b}$$

where $\alpha_{P,0}$ is the small-signal absorption coefficient. The second part of Eq. 4.36 is obtained by insertion of Eq. 4.37a in the first part of Eq. 4.36. For $S_{sp}(\lambda)/w_{0P,sp}$ the curves with the lowest excitation energy density in Fig. 4.32 are used. In the displayed wavelength region it is $A < 1$ (attenuation) for TPA in THF and for m-MTDAB neat film, while it is A ($\lambda < 410$ nm) ≥ 1 (slight amplification to unmodified behaviour) for m-MTDAB in THF.

For vertical polarized transverse excitation and vertical polarized longitudinal emission detection the spontaneous emission attenuation or amplification, $A(\lambda)$, for $w_{0P} << w_{P,sat}$ is approximately given by

$$A(\lambda) \approx \frac{\int_{-\infty}^{\infty} dr e^{-r^2} \int_0^d dz e^{-\alpha_P z} \int_0^{\infty} dt e^{-t/\tau_F} \exp\left\{\left[\sigma_{em}(\lambda) + \sigma_a(\lambda) - \sigma_{ex}(\lambda)\right] f(t) N_{ex,0} e^{-r^2 - \alpha_P z - t/\tau_F} \frac{\ell_s}{2}\right\}}{\int_{-\infty}^{\infty} dr \exp(-r^2) \int_0^d dz \exp(-\alpha_P z) \int_0^{\infty} dt \exp(-t/\tau_F)} \tag{4.38}$$

Thereby the orientation factor, $f(t)$, for parallel oriented transition dipole moments of ground-state absorption (σ_a), stimulated emission (σ_{em}), and excited-state absorption (σ_{ex}) is given by

$$. f(t) = 2\exp\left(-\frac{t}{\tau_{or}}\right)\exp\left(-\frac{w_{0P}}{w_{P,sat}}\right) + 1 \tag{4.39}$$

r is the coordinate perpendicular to the direction of the pump laser propagation and perpendicular to the line-focus direction of the pump laser. z is the coordinate along the pump laser propagation. ℓ_s is the pumped length of the sample. The effective length for amplification or attenuation of spontaneous emission is approximated by $\ell_s/2$. d is the sample thickness along the pump pulse direction. w_{0P} is the peak pump laser energy density at the sample entrance. α_P is the absorption coefficient of the sample at the pump laser wavelength λ_P. τ_{or} is the reorientation time of the transition dipoles. $\sigma_{em}(\lambda)$ and $\sigma_{ex}(\lambda)$ are the orientation averaged stimulated emission cross-section and the orientation averaged excited-state absorption cross-section at λ. $\sigma_a(\lambda)$ is the orientation averaged ground-state absorption cross-section in the fluorescence spectral region. Its contribution takes into account the reduced fluorescence re-absorption due to ground-state population depletion (the spontaneous emission is by this contribution more strongly absorbed than the amplified spontaneous emission). The orientation dependence of the cross-sections is given by $\sigma(\lambda)f(t)$ [Pen76].

Eq. 4.38 may be employed to determine the excited-state absorption cross-section spectrum, $\sigma_{ex}(\lambda)$, from the amplification/attenuation, $A(\lambda, w_{0P})$ displayed in Fig. 4.34. The obtained excited-state absorption spectra are included in Fig. 4.27. For m-MTDAB the excited-state absorption

cross-section spectrum is only calculated from the solution amplification/attenuation results since for the neat film the transition dipole reorientation time is not well known. The excited-state absorption cross-section spectrum of m-MTDAB in solution is larger than the stimulated emission cross-section spectra belonging to the monomeric and excimeric emission of the neat film explaining the observed spontaneous emission attenuation.

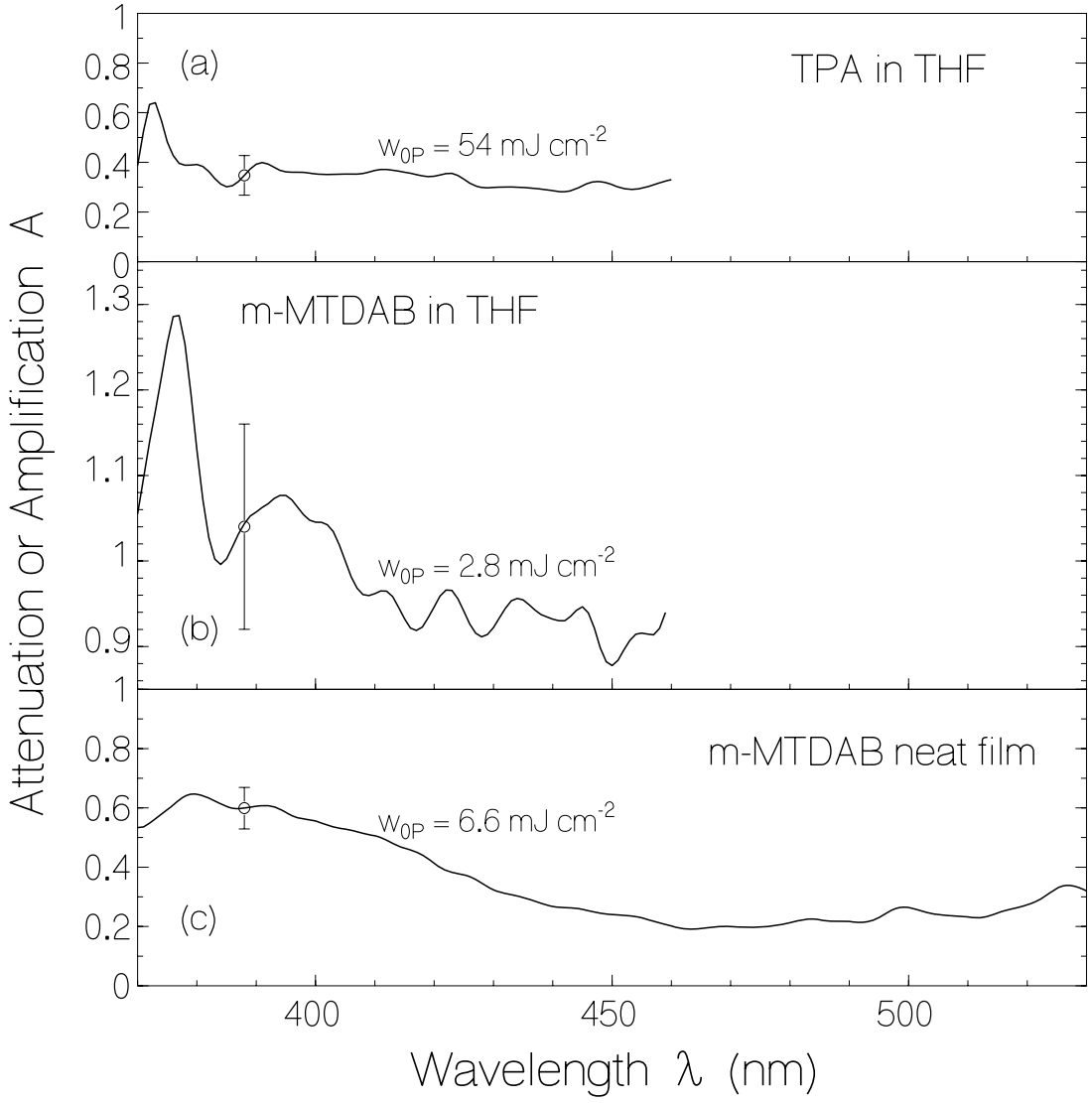

Fig. 4.34: Spectral attenuation or amplification, $A(\lambda)$, of the spontaneous emission at selected input pump pulse excitation energy densities, w_{0P}, for TPA in THF (a), m-MTDAB in THF (b), and m-MTDAB neat film (c).

Table 4.4: Optical and spectroscopic parameters of TPA and m-MTDAB

Parameter	TPA in THF	m-MTDAB in THF	m-MTDAB neat film	Comments
$\lambda_{a,max}$ (nm)	300	300	307	Fig. 4.27
$\lambda_{F,max}$ (nm)	363	383	379	Fig. 4.28
n_F	1.4182 [Hel62]	1.4155 [Hel62]	1.7677 [a)]	for film: Fig. 4.26b
			1.694 [b)]	
ϕ_F	0.012	0.128	0.123	Fig. 4.28
			0.082 [a)]	
			0.041 [b)]	
P_F	0.035	0.055		
τ_F (ns)	1.63	2.19	2.3 [a)]	Fig. 4.29
			4.66 [b)]	
τ_{rad} (ns)	136	17.2	28 [a)]	Eq. 4.5
			104 [b)]	
τ_{or} (ps)	100	270		Eq. 4.4
$\sigma_{a,P}$ (cm^2)	1.85×10^{-18}	1.86×10^{-17}	3.6×10^{-17}	Fig. 4.27
$w_{P,sat}$ (J cm^{-2})	0.31	0.0308	0.016	Eq. 4.16

a: monomeric emission. b: excimeric emission.

4.3.4 Conclusions

The fluorescence efficiency of TPA in solution, ϕ(TPA/THF) = 0.012 was found rather low due to some rotation freedom of the phenyl groups that may cause non-radiative decay by internal conversion. The fluorescence efficiency of the starburst molecule m-MTDAB was found approximately the same is both liquid and solid form i.e. ϕ(m-MTDAB/THF) = 0.128, and ϕ(m-MTDAB neat film) = 0.123. The photo-excitation of m-MTDAB neat films led to excimer formation showing up in red-shifted emission and elongated emission lifetime. In the nonlinear transmission studies at 347.15 nm with second harmonic pulses of a mode-locked ruby laser reverse saturable absorption was observed. The excited state absorption cross-section of $\sigma_{ex,P}$(TPA/THF) = 9×10^{-18} cm^2, and $\sigma_{ex,P}$(m-MTDAB/THF) = 4×10^{-17} cm^2 was found to be lower than the ground state absorption of $\sigma_{a,P}$(TPA/THF) = 1.85×10^{-18} cm^2 and $\sigma_{a,P}$(m-MTDAB/THF) = 1.86×10^{-17} cm^2. The transverse picosecond laser pumped attenuation/amplification of spontaneous emission was exploited to determine the excited-state absorption behaviour of the materials in the fluorescence spectral region. For m-MTDAB in THF a weak amplification of spontaneous emission in the wavelength range from 370 nm to 405 nm was found, while for TPA in THF and m-MTDAB neat films only attenuation was observed indicating that the excited-state absorption is higher than the stimulated emission inhibiting any laser action.

4.3 Poly-phenylene-bipyridine polymer (PPBpy)

Laser action was achieved for various luminescent polymers as already mentioned in introduction: poly-phenylenevinylenes (PPV) [Lem00], poly-phenylene-ethynylenes (PPE) [Hol97], ladder-type poly-*para*-phenylenes (PPP) [Lem00], polyfluorenes (PF) [Hel02], poly-phenylacethylenes (PPA) [McG00], poly-arylene-vinylenes (PAV) [Hol01], poly(dialkoxy-phenylene-vinylene)s [Hol01] (including MEH-PPV [Hol04a], M3EH-PPV [Hör01] and MEH-DOO-PPV [Hör01]), poly-thiophenes (PT) [Gra98], triphenylamine (TPA) based conjugated polymers [Hol01c], and triphenylamine dimer (TPD) based conjugated and non-conjugated polymers [Hol02]. Here a rigid backbone conjugated phenylene/bipyridine polymer, poly[2,2'-bipyridine-5,5'-diyl-(2,5-dihexyl-1,4-phenylene)] (abbreviated PPBpy) [Fra01] as a new class of luminescent polymers, is characterized spectroscopically and investigated for neat thin-film and organic-solution laser action.

The polymer is studied in 1,1,2,2-tetrachloroethane (TCE) and as a thin film on a glass substrate. Absorption cross-section spectra, stimulated emission cross-section spectra, fluorescence quantum distributions, fluorescence quantum yields, degrees of fluorescence polarisation, and fluorescence lifetimes are determined. The saturable absorption of the polymer at 347.15 nm (second harmonic of picosecond ruby laser) is measured and analysed. The amplification of spontaneous emission (travelling-wave lasing) in a PPBpy neat film and the low-Q lasing of PPBpy/TCE in a rectangular cell (cell windows act as low reflectivity resonator mirrors) are studied by transverse sample pumping. The distributed-feedback lasing of PPBpy spin-coated on corrugated gratings etched into a quartz glass is investigated.

The synthesis of rigid backbone conjugated phenylene/bipyridine polymer poly[2,2'-dipyridine-5,5'-diyl-(2,5-dihexyl-1,4-phenylene)] (abbreviated PPBpy) is described in [Fra01]. In

brief palladium catalyzed cross-coupling reaction (Suzuki reaction [Miy95]) of a dialkyl substituted benzene-diboronic acid with 5,5'-dibromo-2,2'-dipyridine was applied.

4.4.1 Absorption cross-section spectra

The transmission spectrum of PPBpy thin film (thickness ≈ 215 nm) on a fused silica substrate is shown in Fig. 4.35.

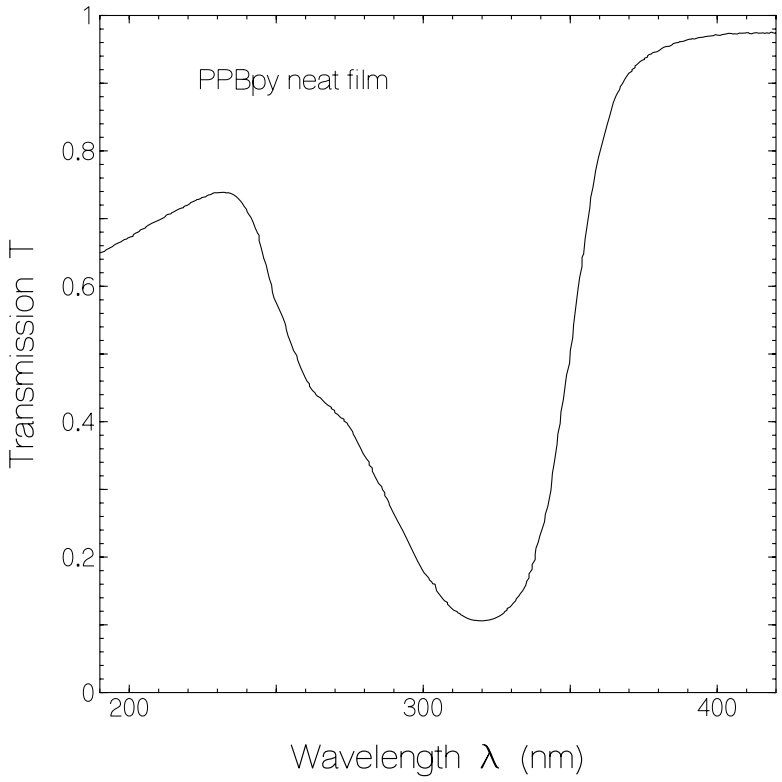

Fig. 4.35: Transmission spectrum of a PPBpy neat film (thickness d_f ≈ 215 nm) on a fused silica substrate.

The absorption cross-section spectra, $\sigma_a(\lambda)$, of PPBpy in TCE and of PPBpy neat film are displayed in Fig. 4.36. $\sigma_a(\lambda)$ of the neat film is calculated assuming the same S_0-S_1 absorption cross-section integral for the solution and the film (Eq. 3.3). The absorption cross-section spectrum of the solution is somewhat broader than that of the neat film and has a shoulder at 365 nm in the long-wavelength absorption tail.

The stimulated emission cross-section spectrum, $\sigma_{em}(\lambda)$, of the neat film is included in Fig. 4.36. It is calculated from the S_0-S_1 absorption spectrum and the fluorescence quantum distribution (see Fig. 4.37a) using the Strickler-Berg formula Eq. 4.2 and the Einstein relation Eq. 4.3. For the PPBpy neat film a Strickler-Berg radiative lifetime of $\tau_{rad,SB}$ = 1.19 ns is determined using λ_u =280 nm, $n_A \approx 1.85$, $n_F \approx 1.75$, (see distributed feedback laser analysis below).

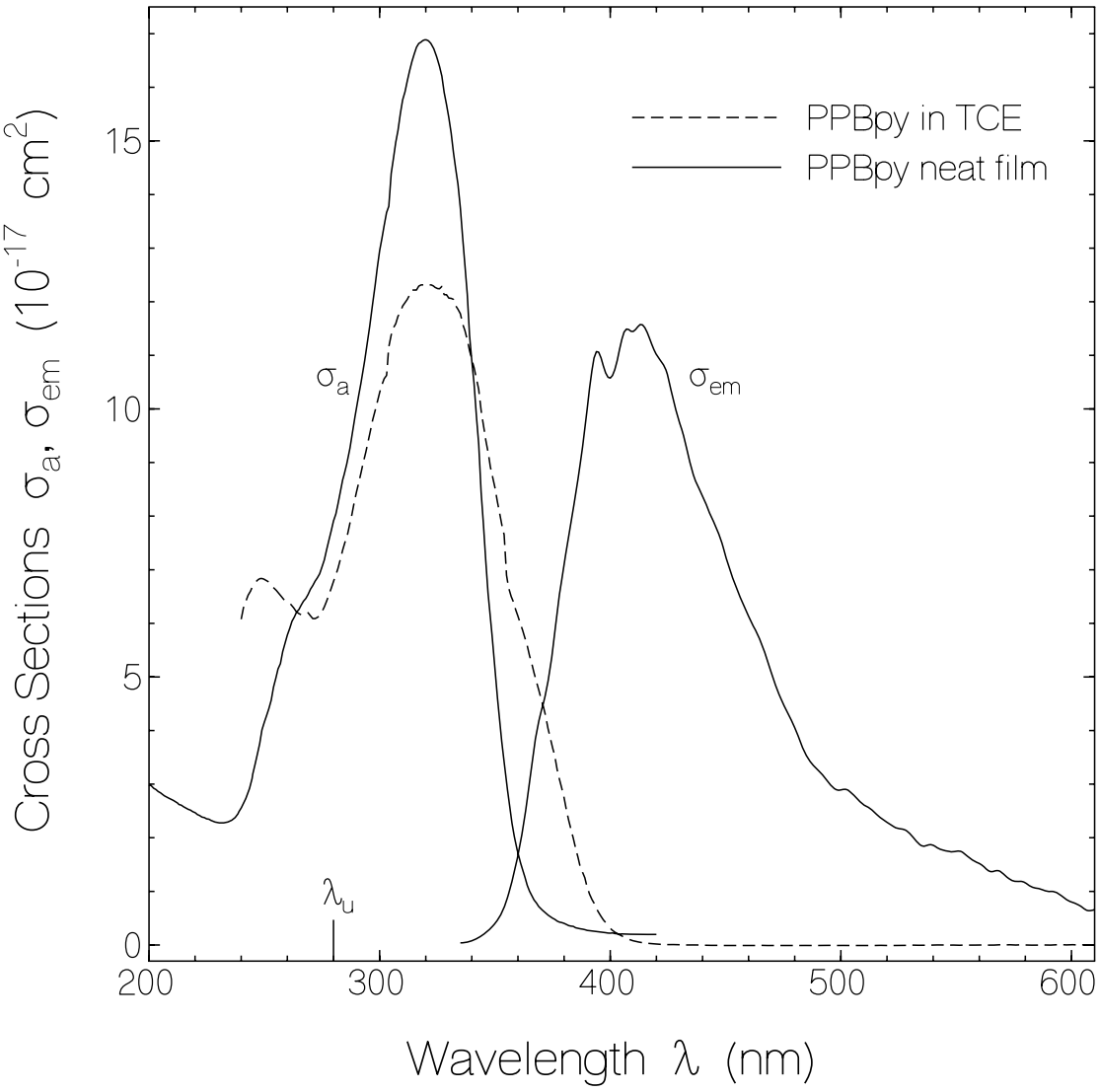

Fig. 4.36: Absorption cross-section, $\sigma_a(\lambda)$, and stimulated emission cross-section, $\sigma_{em}(\lambda)$, spectra of thin film (solid curves) and of 1,12,2-tetrachloroethane (TCE) solution (dashed curve, concentration 7×10^{-5} mol dm^{-3}) of PPBpy. Upper border, λ_u, of S_0-S_1 transition of film used for stimulated emission cross-section calculation is included.

4.4.2 Fluorescence behaviour

The fluorescence quantum distributions, $E_F(\lambda)$, of PPBpy in TCE and of PPBpy neat film are shown in Fig. 4.37a. The fluorescence quantum yield, ϕ_F, (Eq. 3.5), $\phi_F = \int E_F(\lambda) d\lambda$, of the solution is $\phi_F = 0.84 \pm 0.02$ and of the film is $\phi_F = 0.27 \pm 0.02$. The fluorescence in the solution is high. In the film the fluorescence quantum yield is reduced by self-quenching. The fluorescence peak of the neat film occurs at 393 nm. In the TCE solution there is a short-wavelength step at 380 nm and a broad emission with maximum at 460 nm. The emission around 380 nm is

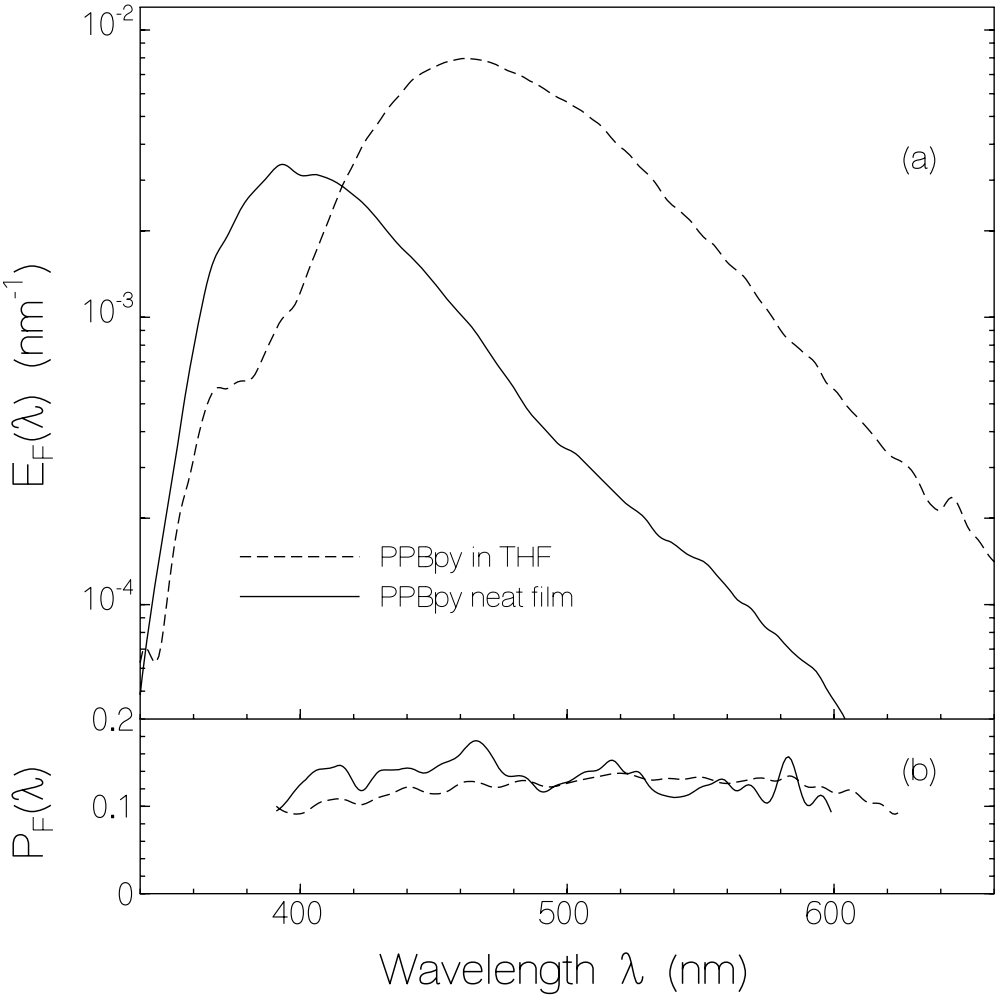

Fig. 4.37: (a) Fluorescence quantum distributions, $E_F(\lambda)$, and (b) degrees of fluorescence polarization, $P_F(\lambda)$, of PPBpy in TCE and as neat film.

attributed to single polymer emission, while the dominant broad structure-less emission in the blue to the yellow spectral region is thought to be due to emission from excited-state aggregates (excimers, aggregate excitons) [Val02, Ban06, And04].

The degrees of fluorescence polarisation, P_F, of PPBpy in TCE and of PPBpy neat film are shown in Fig. 4.37b. In the solution it is $P_F \approx 0.13$, and in the neat film it is $P_F \approx 0.14$.

The degree of fluorescence polarisation, P_F, is related to the reorientation time, τ_{or}, of the transition dipole moments by Eq. 4.4. For PPBpy in TCE it is $P_F \approx 0.13$ and $\tau_F = 1.51$ ns, giving $\tau_{or} \approx 376$ ps. The PPBpy thin film has a $P_F \approx 0.14$ and $\tau_F \approx 300$ ps giving $\tau_{or} \approx 97$ ps.

The temporal fluorescence signals of PPBpy neat film (thickness ≈ 215 nm) and of 1×10^{-4} molar PPBpy in TCE are shown in Fig. 4.38a and 4.38b, respectively. The dotted curves show the detection system response function (attenuated pump pulse directed to micro-channel-plate photomultiplier). In Fig. 4.38a convolutions of the experimental response function with single-exponential decays are shown. The curves are calculated according to Eq. 4.29.

A comparison of the experimental fluorescence curve with the theoretical convoluted single-exponential decay curves gives a fluorescence lifetime of $\tau_F = 300\pm50$ ps for the PPBpy neat film. In Fig. 4.38b the fluorescence decay of PPBpy in TCE is simulated by a two-component single-exponential regression fit according to $S_F(t) = S_{F,0}[x_1 \exp(-t/\tau_{F,1}) + x_2 \exp(-t/\tau_{F,2})]$, giving the fractions $x_1 = 0.87$ and $x_2 = 0.13$ with the fluorescence lifetimes $\tau_{F,1} = 1.71$ ns and $\tau_{F,2} = 137$ ps. An average fluorescence lifetime of $\tau_F \approx 1.51$ is obtained using the relation: $\tau_F = x_1\tau_{F,1} + x_2\tau_{F,2}$.

The radiative lifetime determined from the fluorescence lifetime, τ_F, and the fluorescence quantum yield, ϕ_F, is given by Eq. 4.5 The experimental results are τ_{rad}(solution) ≈ 1.80 ns and τ_{rad}(neat film) ≈ 1.11 ns. The radiative lifetime in the neat film is shorter than in the solution

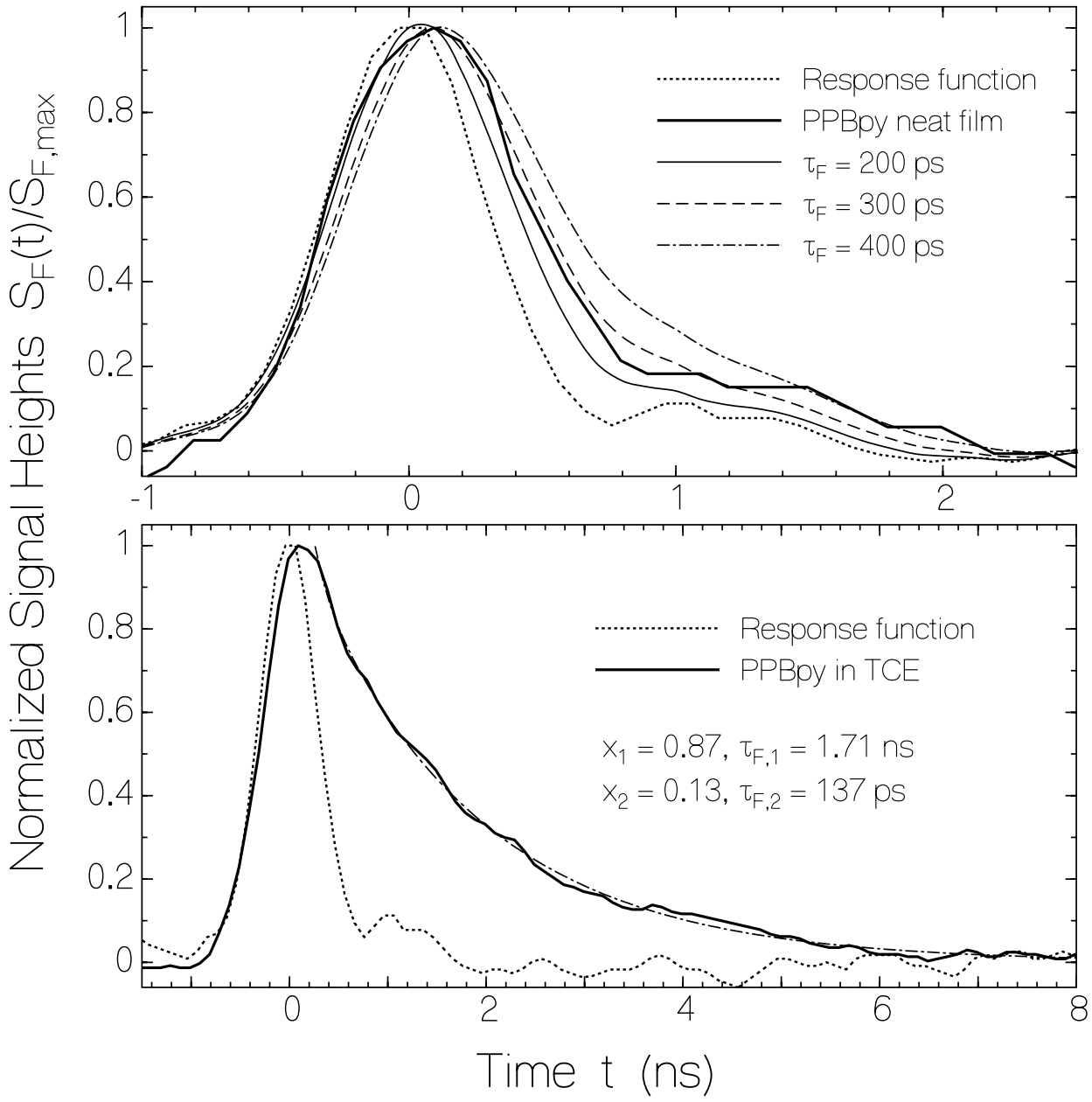

Fig. 4.38: Temporal fluorescence traces of PPBpy neat film (a) and of 1×10^{-4} molar PPBpy in TCE (b) measured with micro-channel-plate photomultiplier. Fluorescence traces are recorded at 428 nm (spectral width of applied interference filter was 3.4 nm). Dotted curves show the response function. The calculated curves in (a) are convolutions of single-exponential decays with response function. Calculated curve in (b) is a bi-exponential regression fit.

because of the higher refractive index of the neat film (see Eq. 4.2: $\tau_{rad} \propto n_A n_F^{-3}$). The calculated monomeric radiative lifetimes, $\tau_{rad,SB}$, determined by use of the Strickler-Berg formula (Eq. 4.2)

gives $\tau_{rad,SB}$(neat film) ≈ 1.19 ns. Within our experimental accuracy the determined neat film radiative lifetime, τ_{rad}, is found to be the same as the calculated repeat unit based radiative lifetime, $\tau_{rad,SB}$, indicating that the excited-state wavefunction is localized to a repeat unit [Hol01]. The average wavefunction delocalisation factor is $m_{del} = \tau_{rad,SB} / \tau_{rad} \approx 1$.

The fluorescence lifetime of PPBpy neat film is only 300 ps ($\phi_F \approx 0.27$). The fluorescence quenching is thought to be to due to inter-chain charge separation (polaron formation) [Hol02b, Fro97, Sil01]. For PPBpy in TCE a two-component fluorescence emission is observed both in the fluorescence spectrum (Fig. 4.37) and the fluorescence decay (Fig. 4.38b). The short-wavelength and short lifetime emission is thought to be due to single repeat unit emission. The long-wavelength and long lifetime emission is thought to be due to emission from excited-state aggregates (excimers, aggregate excitons) [And04, Ban06]. The quenching of the single repeat unit fluorescence is expected to be due to excitation transfer to the excited-state aggregates [Shi07].

4.4.3 Saturable absorption behaviour

The experimental energy transmission, T_E, of second harmonic picosecond ruby laser pulses (duration Δt_P = 35 ps, wavelength λ_P = 347.15 nm) through a 1 mm cell filled with PPBpy in TCE as a function of the input peak pulse intensity, I_{0P}, is shown by the circles in Fig. 4.39. The energy transmission remains practically remains unchanged over the displayed intensity range from 5×10^6 W cm^{-2} to 1×10^{10} W cm^{-2}. The slow-absorber saturation intensity is given by [Her67] (Eq. 2.2).

For PPBpy in TCE a value of $I_{P,sat.sl} = 1.8\times10^8$ W cm^{-2} is calculated ($\nu_P = c_0/\lambda_P$, c_0 is vacuum light velocity, λ_P = 347.15 nm, $\sigma_{a,P} = 9.2\times10^{-17}$ cm^2, Δt_P =35 ps). Since no change in transmission with excitation intensity is observed even beyond the saturation intensity, it is concluded that the

pump pulse excited-state absorption is approximately the same as the pump pulse ground-state absorption, i.e. $\sigma_{ex,P} \approx 9.2\times10^{-17}$ cm^2.

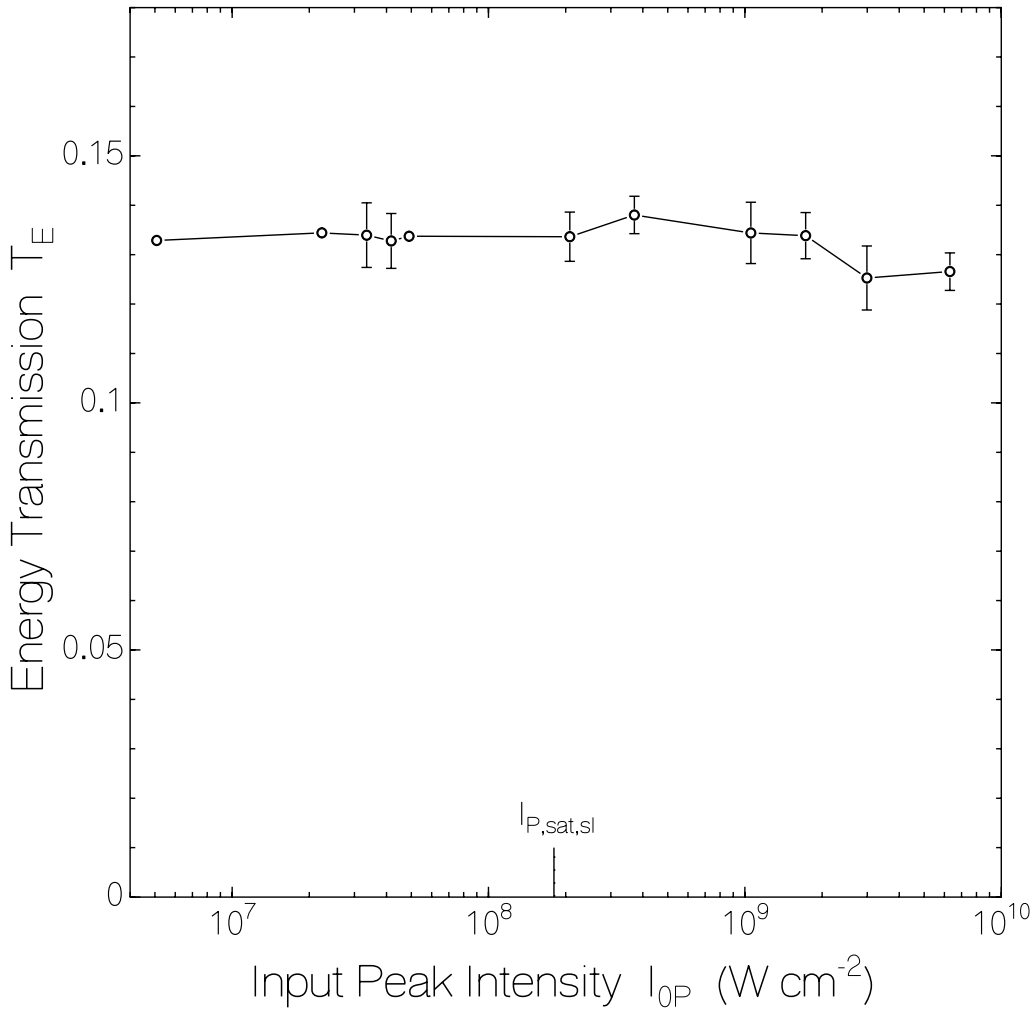

Fig. 4.39: Saturable absorption behaviour of PPBpy in TCE. Measured energy transmission versus input pump pulse peak intensity is shown. Pump laser pulses: second harmonic of picosecond ruby laser (wavelength 347.15 nm, duration 35 ps FWHM).

Table 4.5: Optical and spectroscopic parameters of polymer PPBpy

Parameter	PPBpy in TCE	PPBpy neat film	Comments
$\lambda_{a,max}$ (nm)	320	320	Fig. 4.36
$\lambda_{F,max}$ (nm)	380 and 461	394	Fig. 4.37
n_F	1.5084 [Hel62]	1.75	for film: DFB laser analysis
ϕ_F	0.86	0.27	Fig. 4.37a
P_F	0.13	0.14	Fig. 4.37b
τ_F (ns)	1.71 and 0.137	0.30	Fig. 4.38
τ_{rad} (ns)	1.76	1.11	Eq. 4.5
$\tau_{rad,SB}$ (ns)		1.19	Eq. 4.2
τ_{or} (ps)	376	97	Eq. 4.4

Abbreviations: $\lambda_{a,max}$: wavelength of peak absorption of first absorption band. $\lambda_{em,max}$: wavelength of peak stimulated emission cross-section. $\lambda_{F,max}$: wavelength of fluorescence maximum. n_F: average refractive index in fluorescence region. ϕ_F: fluorescence quantum yield. P_F: degree of fluorescence polarisation. τ_F: fluorescence lifetime. τ_{rad}: radiative lifetime. τ_{or}: transition dipole moment reorientation time.

4.4.4 Laser Performance

The transverse pumped lasing of PPBpy/TCE in a 1 cm × 1 mm dye-laser cell, the wave-guided travelling-wave lasing (amplification of spontaneous emission) of a neat thin film of PPBpy on a microscope carrier plate, and the distributed-feedback laser action of a neat thin film of PPBpy on corrugated Bragg gratings etched into a fused silica plate are studied.

4.4.4.1 Transverse pumped low-Q laser

A 1.1×10^{-3} molar solution of PPBpy in TCE (repeat unit number density $N_0 = 6.62\times10^{17}$ cm^{-3})

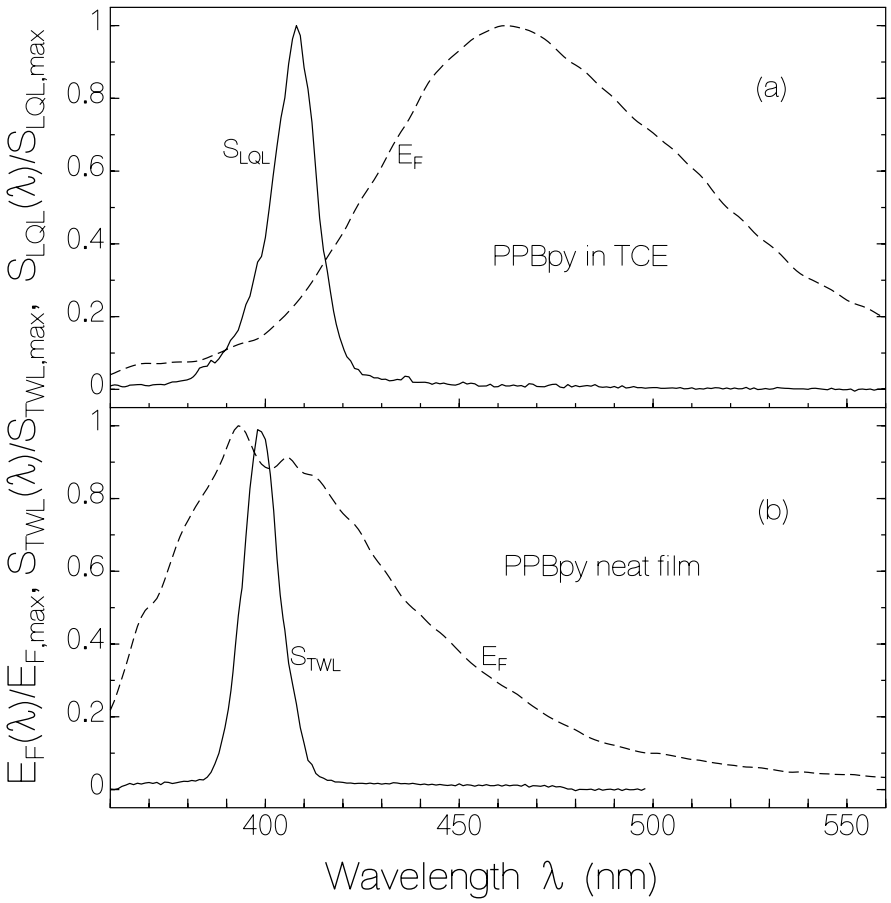

Fig. 4.40: Spectral shapes of (a): low-Q laser emission, $S_{LQL}(\lambda)/S_{LQL,max}$ of PPBpy in TCE (concentration 7.9×10^{-4} mol dm^{-3}, excitation energy density w_{0P} = 5 mJ cm^{-2}).
(b): Travelling-wave laser emission, $S_{TWL}(\lambda)/S_{TWL,max}$, of PPBpy neat film (thickness 950 nm, w_{0P} = 1.5 mJ cm^{-2}). For comparison the normalized fluorescence quantum distributions, $E_F(\lambda)/E_{F,max}$, are also displayed.

kept in a dye-laser cell of ℓ_s = 1 cm length and d = 1 mm length was transverse pumped with line-focused picosecond second-harmonic pulses of a ruby laser system (pump beam cross-section 14.5 mm × 0.245 mm). The cell itself formed the optical laser resonator (low-Q resonator): the end surfaces of the cell acted as mirrors (reflectance $R = (n-1)^2/(n+1)^2$ = 0.03616, n = 1.4696 is refractive index of cell glass at 406 nm).

In Fig. 4.40a a output spectrum of the low-Q laser, $S_{LQL}(\lambda)$, is shown. It belongs to an excitation pulse energy of w_{0P} = 5 mJ cm^{-2}. The emission maximum is at $\lambda_{LQL,max}$ = 406 nm. It is slightly red-shifted compared to the wavelength position of the repeat unit based peak fluorescence emission, but strongly blue-shifted compared to excimeric emission. The laser line-width is $\Delta\lambda_{LQL} \approx$ 13 nm (FWHM) at the applied excitation pulse energy. The occurrence of the laser emission at the single repeat unit short-wavelength excitation position indicates that the excimeric emission is formed after the monomeric excitation, and that the laser emission build-up time (roughly cell round-trip time $t_{tr} \approx$ 100 ps) is shorter than the excimer emission build-up time (given by fast fluorescence decay time $\tau_{F2} \approx$ 137 ps).

The dependences of the laser output energy, W_{LQL}, of the laser wavelength peak position, $\lambda_{LQL,max}$, and of the spectral halfwidth (FWHM), $\Delta\lambda_{LQL}$, on the peak input pump laser energy density, w_{0P}, are displayed in Fig. 4.41a, b, and c, respectively. In Fig. 4.41a, above a certain threshold pump pulse energy density of laser action, $w_{0P,th} \approx$ 1.4 mJ cm^{-2}, the emission rises steeply beyond the spontaneous emission and amplified spontaneous emission level due to low-Q laser oscillation action. In Fig. 4.41b it is seen, that the wavelength position of light emission below laser oscillator threshold is at about 452 nm, and above laser threshold is at about 407 nm. The laser emission occurs at the peak of effective repeat-unit based stimulated emission cross-

section, $\sigma_{em,eff}(\lambda) = \sigma_{em}(\lambda) - \sigma_{ex}(\lambda)$. In Fig. 4.41c it is seen that the spectral halfwidth, $\Delta\lambda_{TWL}$, of the light emission shrinks down from about 90 nm before laser action ($w_{0P} < w_{0P,th}$) to about 15 nm above laser threshold.

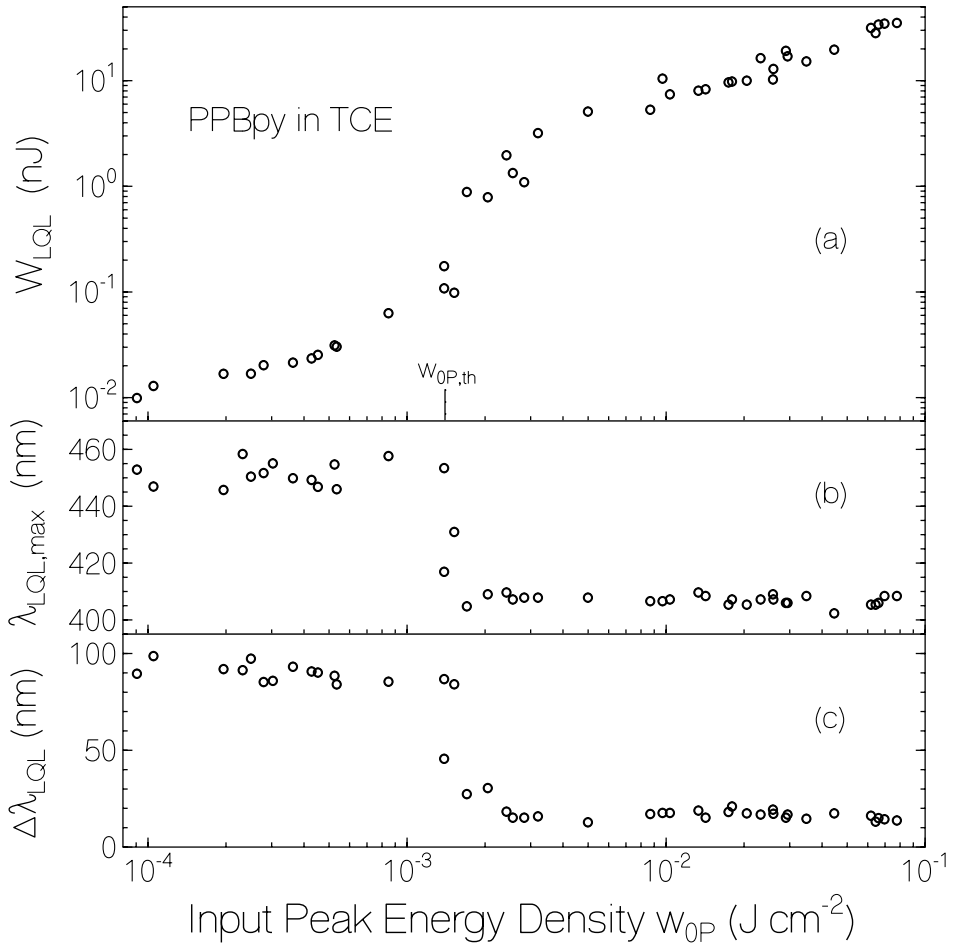

Fig. 4.41: Low-Q laser oscillator performance of PPBpy dissolved in TCE filled in a dye-laser fused silica cell (1 cm length, 1 mm thick) transverse pumped with line-focused (beam cross-section 14.5 mm × 0.245 mm) second harmonic pulses of a mode-locked ruby laser (pulse duration $\Delta t_P \approx 35$ ps, wavelength $\lambda_P = 347.15$ nm). Concentration $C_0 = 1.1\times10^{-3}$ mol dm^{-3}.
(a) Collected emission signal, W_{LQL}, versus input pump pulse energy density, w_{0P}. Full acceptance angle of fluorescence collection is $\Delta\theta = 0.82°$. Pump laser threshold energy density $w_{P,th} \approx 1.4$ mJ cm^{-2}.
(b) Peak wavelength of low-Q laser oscillator, $\lambda_{LQL,max}$, versus input pump pulse energy density, w_{0P}.
(c) Spectral line-width (FWHM) of low-Q laser oscillator, $\Delta\lambda_{LQL}$, versus input pump-pulse energy density, w_{0P}.

At laser oscillator threshold the light amplification $V = \exp(\sigma_{em,eff,L} N_{ex,0,th} \ell_s)$ compensates the reflection losses $L = R^{-1}$. The effective stimulated emission is given by $\sigma_{em,eff,L} = \sigma_{em,L} - \sigma_{ex,L}$, where $\sigma_{em,L}$ is the stimulated emission cross-section at the peak laser wavelength, and $\sigma_{ex,L}$ is the excited-state absorption cross-section at the peak laser wavelength. There occurs no laser action if $\sigma_{ex,L} \geq \sigma_{em,L}$.

Insertion of experimental values into Eq. 4.22 (R = 0.03616, $w_{0P,th} = 1.4\times10^{-3}$ J cm^{-2}, $w_{P,sat} = 6.2\times10^{-3}$ J cm^{-2}, $N_0 = 6.62\times10^{17}$ cm^{-3}, $\sigma_{a,P} = 9.2\times10^{-17}$ cm^2, ℓ_s = 1 cm) gives $\sigma_{em,eff,L} = 2.48\times10^{-17}$ cm^2.

4.4.4.2 Neat thin film wave-guided travelling-wave laser

The wave-guided travelling-wave laser action (wave-guided amplification of spontaneous emission) was studied using a thin film of PPBpy spin-coated from a TCE solution (concentration 20 mg/ml, speed 600 rpm, obtained film thickness ≈ 850 nm) onto a microscope carrier plate (optical glass similar to Schott type BK7) and cut in the film region for optimum edge emission.

In Fig. 4.40b an edge-emitted travelling-wave laser spectral shape is shown (solid line) for a pump pulse energy density of w_{0P} = 1.5 mJ cm^{-2}. For comparison the shape of the fluorescence quantum distribution is included in the figure.

The dependences of the collected laser output energy, W_{TWL}, of the laser wavelength peak position, $\lambda_{TWL,max}$, and of the spectral halfwidth (FWHM), $\Delta\lambda_{TWL}$, on the peak input pump laser energy density, w_{0P}, are displayed in Figs. 4.42a, b, and c, respectively.

In Fig. 4.42a, above a threshold pump pulse energy density, $w_{0P,th} \approx 1.3\times10^{-4}$ J cm^{-2}, the emission begins to rise beyond the spontaneous emission level due to stimulated emission (amplification of spontaneous emission). At high pump pulse energy density the output signal saturates to a maximum value, $W_{TWL,max} \approx 0.04$ nJ and $w_{P,g,sat} \approx 5.5\times10^{-4}$ J cm^{-2} is the pump pulse

energy density of gain saturation. The experimental behaviour is fitted by Eq. 4.23. The saturation is thought to be caused by exciton-exciton annihilation processes at high densities of excited molecules [Hol02b, Kep96].

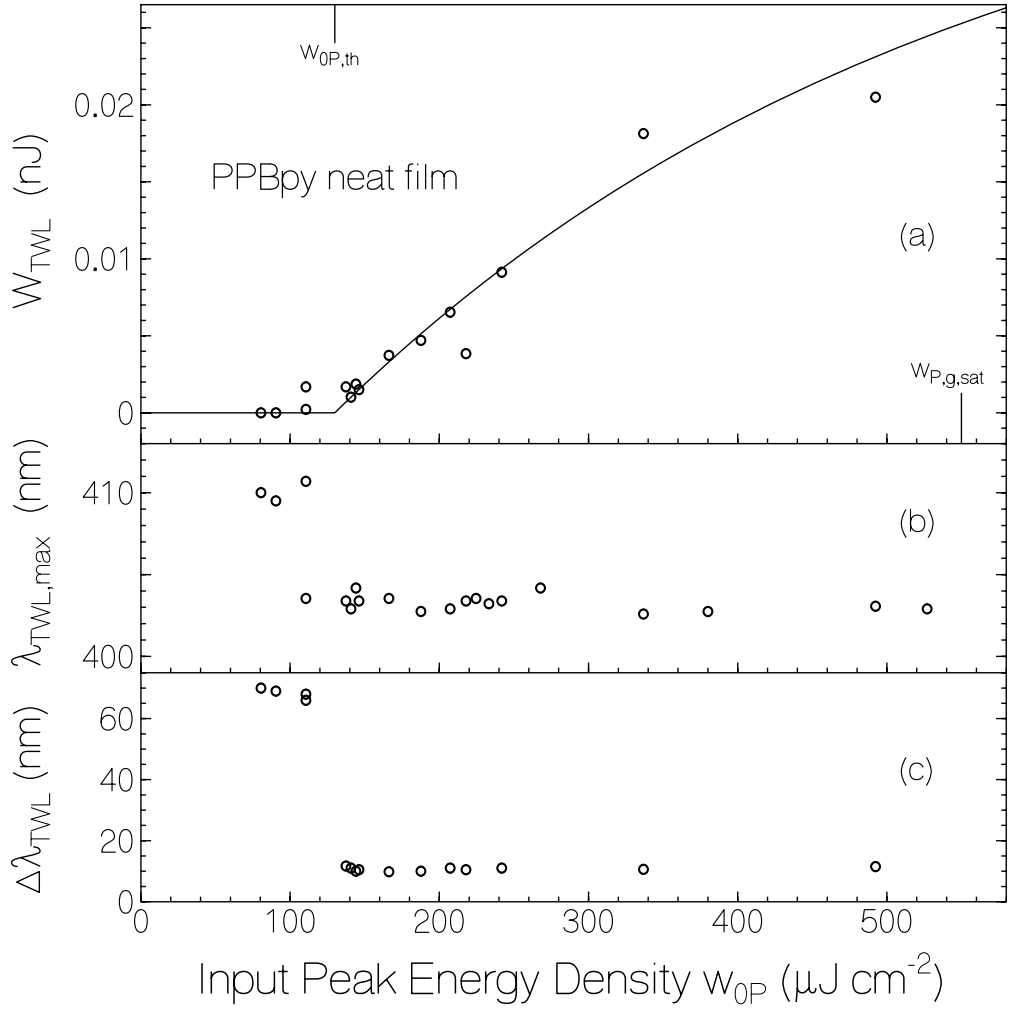

Fig. 4.42: Wave-guided travelling-wave laser performance of a PPBpy neat film on an optical glass substrate. Film thickness, d_f = 950 nm; pumped film area, 0.15 mm × 0.245 mm.
(a) Collected emission signal, W_{TWL}, versus input pump pulse energy density, w_{0P}. Full acceptance angle of fluorescence collection is $\Delta\theta$ = 0.3 rad. Curve is calculated by use of Eq. 4.23 with a pump laser threshold energy density $w_{P,th}$ = 130 μJ cm^{-2}, a pump pulse energy density of gain saturation $w_{P,g,sat}$ = 0.55 mJ cm^{-2}, and a maximum output energy $W_{TWL,max}$ = 0.04 nJ
(b) Peak wavelength of travelling-wave laser, $\lambda_{TWL,max}$, versus input pump pulse energy density, w_{0P}.
(c) Spectral linewidth (FWHM) of travelling-wave laser, $\Delta\lambda_{TWL}$, versus input pump pulse energy density, w_{0P}.

In Fig. 4.42b, the wavelength position of peak light emission, $\lambda_{TWL,max}$, blue-shifts from about 410 nm at low excitation energy density to 403 nm at high excitation energy density (efficient amplification of spontaneous emission at position of peak effective stimulated emission cross-section).

In Fig. 4.42c it is seen that the spectral halfwidth, $\Delta\lambda_{TWL}$, of the light emission shrinks around the laser threshold from a spontaneous emission line-width of $\Delta\lambda_F \approx 70$ nm to $\Delta\lambda_{TWL} \approx 11$ nm, and then remains nearly constant.

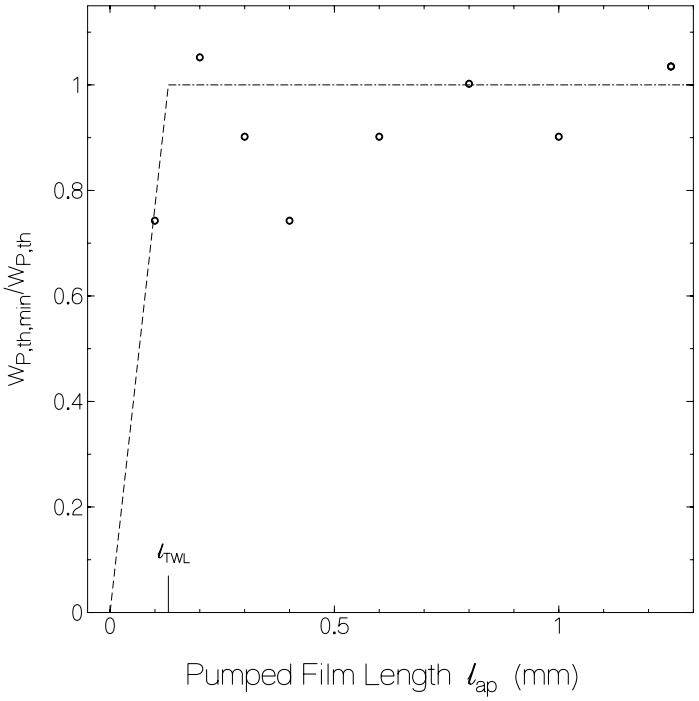

Fig. 4.43: Normalized inverse laser threshold pump pulse energy density, $w_{P,th,\min} / w_{P,th}$, versus exposed film length, ℓ_{ap}. The kink of the line gives the effective gain length, ℓ_{TWL}. Film thickness $d_f = 950$ nm.

In Fig. 4.43 the inverse ratio of the pump laser threshold energy density, $w_{P,th,min}/w_{P,th}$, versus the excited film length, ℓ_{ap}, is presented in order to determine approximately the effective length of light amplification, ℓ_{TWL}. The constant dashed line approximates the behaviour for pumped lengths longer than the effective gain length, and the dash-dotted line approximates the situation for pump lengths shorter than the effective gain length. From the crossing point of the lines one

obtains $\ell_{TWL} \approx 0.15$ mm. If the gain length is limited by ground-state tail absorption, $\alpha(\lambda_{TWL,max})$, at the peak laser wavelength, $\lambda_{TWL,max} \approx 403$ nm, then it is $\alpha(403\text{ nm}) \approx \ell_{TWL}^{-1} \approx 67$ cm^{-1} and the absorption cross-section is $\sigma_a(403\text{ nm}) = \alpha(403\text{ nm})/N_f \approx 1.1\times10^{-19}$ cm^2 (repeat unit number density of neat film $N_f \approx 6.2\times10^{20}$ cm^3).

A value of $\eta_{sl,ini} \approx 2.6\times10^{-4}$ is estimated using the Eq. 4.24. It should be noted that the true initial laser slope efficiency is larger since the emission angle at the film edge is larger than the acceptance angle of the collecting lens ($\Delta\theta = 0.3$ rad). It is also the effective gain length, ℓ_{TWL}, shorter than the pump laser width, d_w, indicating that amplified spontaneous emission occurs in all directions of the plane (light emitted into the film plane is dumped in the un-pumped film plane).

4.4.4.3 Distributed-feedback laser

Distributed-feedback laser studies have been carried out for a PPBpy neat thin film on corrugated gratings etched into a fused silica plate. Grating spacing of $\Lambda = 300$ nm, and 280 nm were used. The grating size was 1.5 mm × 0.5 mm (groove length 0.5 mm). The exposed grating area was 0.9×0.13 mm^2. The surface-emitted radiation was collected and detected. The laser wavelength, λ_{DFB}, is proportional to the grating spacing, and it increases with film thickness. TE modes (electrical field vector in film plane) and TM modes (electrical field vector perpendicular to film plane) are excited.

Some lasing results are shown in Fig. 4.44 and some physical and spectroscopic parameters of the DFB lasers are collected in Table 4.6. In Fig. 4.44 the DFB laser spectra (solid curves) are compared with travelling-wave laser spectra (the same dash-dotted curves in each sub-figure),

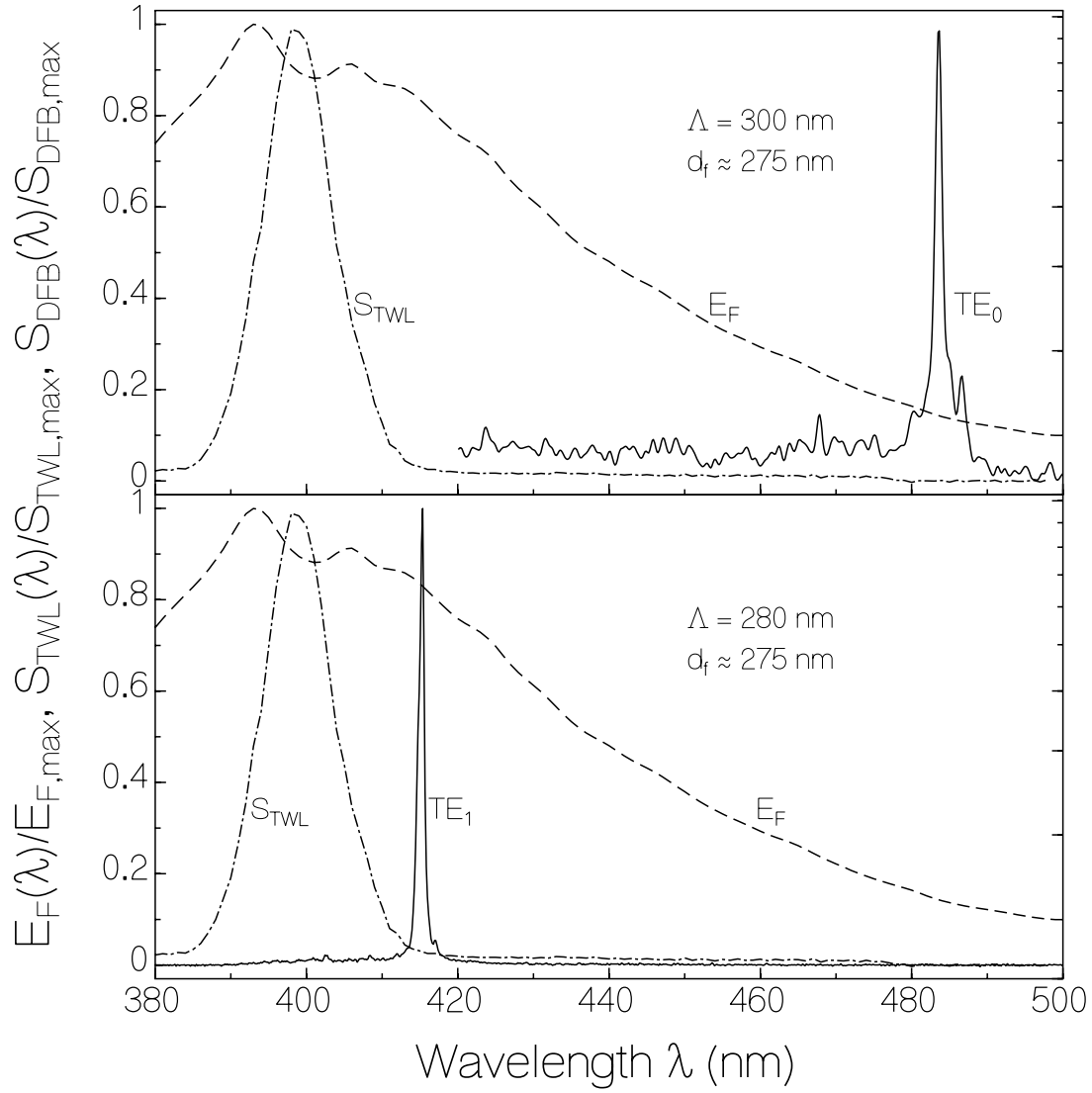

Fig. 4.44: Spectra of surface-emitting thin-film PPBpy distributed feedback lasers (solid curves, pumped area 0.9 mm × 0.13 mm, acceptance angle $\Delta\theta = 36°$). For comparison normalized edge-emitted wave-guided thin-film travelling-wave laser emission spectrum (from Fig. 4.41) and normalized fluorescence quantum distribution (from Fig. 4.37) are included. Several parameters are listed in Table 4.6.
(a) DFB laser A: Grating spacing $\Lambda = 300$ nm. Film thickness $d_f \approx 275$ nm. Applied pump pulse energy density $w_{0P} = 1.0$ mJ cm^{-2}.
(b) DFB laser B: $\Lambda = 280$ nm. $d_f \approx 275$ nm. $w_{0P} = 1.1$ mJ cm^{-2}.

and with the shapes of the fluorescence quantum distributions (the same dash curves in each sub-figure). The spin-coated film on the substrate was ≈ 275 nm thick (determined by distributed waveguide resonance condition, Eq. 4.27). The DFB laser spectra shown were measured with a

polarizer in s-direction in the detection path for TE mode emission detection. In Fig. 4.44a (grating spacing Λ = 300 nm) lasing occurred at λ_{DFB} = 483.7 nm (TE mode) with a spectral width of $\Delta\lambda_{DFB} \approx$ 1.3 nm. The applied pump pulse energy was $W_P \approx$ 1.2 μJ, and the collected DFB laser energy was $W_{DFB} \approx$ 0.03 nJ. In Fig. 4.44b (Λ = 280 nm) lasing occurred at λ_{DFB} = 415.36 nm with a spectral line-width of $\Delta\lambda_{DFB} \approx$ 0.9 nm. The pump pulse energy was $W_P \approx$ 1.3 μJ, and the collected DFB laser energy was $W_{DFB} \approx$ 0.5 nJ.

Depending on the grating spacing and the film thickness the DFB laser wavelength can be tuned across the main part of the fluorescence spectrum. The DFB laser action suppresses the travelling-wave laser action.

In a trial and error fit of Eq. 4.27 to the known $N = n_f \sin(\theta_\kappa)$, the parameters d_{eff} and θ_κ are determined and finally d_f and n_f are calculated. The obtained values are $d_f \approx$ 275 nm, n_f(483.7nm) ≈ 1.70, and n_f(415.4 nm) ≈ 1.75 (see above Table 4.5).

The transmission through the film at the pump laser wavelength λ_P = 347.15 nm outside the grating area was measured to be T_P = 0.33. Knowing the film thickness the absorption coefficient of the film was determined to be $\alpha_P = -\ln(T_P)/d_f \approx 4.0\times10^4$ cm^{-1}. The PPBpy repeat unit number density in the film is estimated to be $N_f = \alpha_P/\sigma_{a,P} \approx 6.2\times10^{20}$ cm^{-3} ($\sigma_{a,P} \approx 6.5\times10^{-17}$ cm^2, see Fig. 4.36). The mass density, ρ, of the PPBpy neat thin films is determined to be $\rho = (N_f/N_A)M \approx$ 0.41 g cm^{-3}, where N_A is the Avogadro constant and M = 398.6 g mol^{-1} is the molar mass of a repeat unit. The low density indicates a lot of free volume in the polymer solid state and a kinked structure of the conjugated polymer. This may explain the small measured degree of fluorescence polarisation and the chromophore localisation to single repeat unit (no coherent delocalisation of the excitation over several repeat units).

Table 4.6: Physical and spectroscopic parameters of PPBpy distributed feedback lasers.

Parameter	DFB laser A	DFB laser B
Λ (nm)	300	280
t (nm)	50	50
c (nm)	150	140
d_f (nm)	≈ 275	≈ 275
d_{eff} (nm)	≈ 300	≈ 300
M	1	1
λ_{DFB} (nm)	483.66	415.36
N	1.6122	1.4834
	TE_0	TE_1
κ	1	1
θ_κ (°)	71.71	57.89
n_f	1.7	1.75
d_{min} (nm)	79.13	58.80
θ_{crit} (°)	59.39	57.06
$\ell_{\parallel, exc}$ (mm)	0.9	0.9
$\ell_{\perp,exc}$ (mm)	0.13	0.13

Abbreviations: Λ: groove spacing. t: groove depth. c: groove width. d_f: film thickness. d_{eff}: effective film thickness in grating region. M: diffraction order. λ_{DFB}: distributed-feedback laser wavelength. N: effective refractive index. κ: guided mode number. θ_κ: propagation angle. n_f: refractive index of film. d_{min}: minimal film thickness for wave-guiding. θ_{crit}: critical angle for total internal reflection ($\theta_{crit} = \arcsin(n_s / n_f)$ with n_s refractive index of substrate). $\ell_{\parallel, exc}$: length of exposed grating area. $\ell_{\perp,exc}$: width of exposed grating area.

4.4.5 Conclusions

The high fluorescence efficiency of the luminescent polymer PPBpy in liquid solution ($\phi \approx 0.86$) was partly self-quenched in the solid state ($\phi \approx 0.27$). Dominant excimeric fluorescence emission was observed for the polymer in 1,1,2,2-tetrachloroethane (TCE) at the applied repeat unit concentration of 1.1×10^{-4} mol dm^{-3}. In the nonlinear transmission studies at 347.15 nm, it was found that the excited state absorption is approximately the same as the ground state absorption (no saturable absorption and no reverse saturable absorption). The effective stimulated emission cross-section of PPBpy in TCE at 403nm, determined by laser thresholds measurements turned out to be $\sigma_{em,eff,L} = 2.48\times10^{-17}$ cm^2, which allows good laser action. Wave-guided travelling-wave laser action of a transversely pumped neat film and distributed feed-back laser action of a transversely pumped neat film on corrugated gratings were achieved with low laser threshold.

The performed laser studies on PPBpy show that conjugated phenylene/bipyridine polymers form a further class of lasing luminescent polymers besides the poly-phenylenevinylenes [2,3], poly-phenylenes-ethynylenes [Hol97], poly-*para*-phenylens [Lem00], polyfluorenes [Hel02], poly-phenylacetylenes [McG00], poly-arylene-vinylenes [Hol01], poly(dialkoxy-phenylene-vinylene)s [Hol04], and triphenylamine as well as triphenylamine dimer based polymers [Hol01c].

5. Summary

In this work electroluminescent molecules were investigated by optical spectroscopy. Their lasing ability was studied in liquid solutions using a low–Q laser oscillator arrangement. In neat films wave-guided amplification of spontaneous emission was investigated. Some studies concerning the distributed feedback laser action of neat films on corrugated gratings were made.

The investigated materials were the triphenylamine molecule TPA, the triphenylamine starbust molecule m-MTDAB, the triphenylamine dimer TPB, the napthyl-diphenylamine dimer β-NPD, the oligomer dicarbazovinylene-MEH-benzene 2CzV-MEH-B, and the phenylene-bipyridine polymer PPBpy.

The molecule triphenylamine (TPA) in tetrahydrofuran (THF) and the starburst triphenylamine oligomer 1,3,5-tris(3-methylphenylphenylamino)benzene (m-MTDAB) in THF and as neat film were characterized. The fluorescence decay was studied by picosecond laser excitation and time-resolved signal detection. Reverse saturable absorption was observed in picosecond laser nonlinear transmission measurements (laser duration 35 ps, laser wavelength 347.15 nm). The lasing ability of the compounds was tested by picosecond laser transverse pumped amplification or attenuation of spontaneous emission. The excited-state absorption cross-section spectra of the samples in the fluorescence spectral regions were extracted from the amplification/attenuation of spontaneous emission. Weak amplification of spontaneous emission was observed for m-MTDAB in THF around the fluorescence maximum (370 to 405 nm). For TPA in THF and m-MTDAB neat film attenuation of spontaneous emission occurred over the whole fluorescence region (excited-state absorption stronger than stimulated emission).

The molecules N,N,N',N'-tetraphenylbenzidine (TPB, triphenylamine dimer TAD) and N,N'-bis(2-naphtalenyl)-N,N'-bis(phenylbenzidine) (β-NPB, naphtyl-diphenylamine dimer β-NPD) dissolved in tetrahydrofuran (THF) and as neat films were studied. The excited-state absorption at the pump laser wavelength was determined by saturable absorption measurement. Low-Q laser oscillation of TPB in THF was achieved by transverse pumping the solution in a cell. The excited-state absorption of TPB in THF at the laser wavelength was extracted from the laser threshold. In TPB neat films wave-guided travelling-wave lasing was achieved. No laser action was obtained for β-NPB because of very small S_1-S_0 stimulated emission strength, and the presence of the excited-state absorption in the fluorescence wavelength region.

The oligomeric molecule 1,4-bis(9-ethyl-3carbazovinylene)-2-methoxy-5-(2'-ethyl-hexyloxy)-benzene (abbreviated 2CzV-MEH-B) dissolved in tetrahydrofuran (THF) and as neat film was investigated upon its optical spectroscopic properties and its lasing properties. Again the excited-state absorption at the pump-laser wavelength was determined by saturable absorption measurements. Laser oscillation of the dye in THF in a rectangular cell was achieved by transverse pumping. From the emission behaviour around threshold the excited-state absorption cross-section spectrum in the laser active spectral region of the material was extracted. The wave-guided travelling-wave lasing behaviour of the emitter as neat film was studied by analysis of the amplification of the transverse pumped spontaneous emission. Surface emitting distributed-feedback lasing was achieved with a neat film on corrugated second-order periodic gratings.

The luminescent polymer, poly[2,2'-bipyridine-5,5'-diyl-(2,5-dihexyl-1,4-phenylene)] (abbreviated PPBpy) dissolved in tetrachloroethane (TCE) and as neat film was characterized optically by absorption, emission spectroscopy and saturable absorption measurements. Low-Q laser oscillation of the polymer in TCE was achieved and used to determine the effective

stimulated emission cross-section at the lasing wavelength. Travelling-wave lasing of a neat film of the polymer was achieved. Surface-emitting distributed-feedback lasing was obtained with a neat film on corrugated second-order periodic gratings.

The investigated electroluminescent molecules are applied in organic light emitting devices (OLEDs). The investigated polymer is a potential candidate for polymer light emitting devices. For their application in light emitting devices a high quantum yield of electroluminescence is sufficient. But for the application of the electroluminescent materials in laser devices it is indispensible that the stimulated emission cross-section is higher than the excited state absorption cross-section. Good OLED performance of an electroluminescent material is a precondition for good organic lasers, but in each case the effective stimulated emission cross-section (stimulated emission cross-section–excited state absorption cross-section) has to be determined to get information about its lasing ability as was done in this work.

The oligomeric emitter 2CzV-MEH-B, the triphenylamine dimer TPB, and the phenylene-bipyridine polymer PPBpy turned out to be good organic active media for laser action in the violet and blue spectral region.

References

[Abk86] Abkowitz M., D. M. Pai, Philos. Mag. B 53 (1986) 193.

[Amm95] Ammer F., A. Penzkofer, P. Weidner, Chem. Phys. 192 (1995) 325.

[And04] D'Andrade B.W., S.R. Forrest, Adv. Mater. 16 (2004) 1585.

[Bal01] Balzani V., Electron transfer in Chemistry, Wiley-VCH, Weinheim, 2001.

[Ban06] Bansal A. K., W. Holzer, A. Penzkofer, T. Tsuboi, Chem. Phys. 330 (2006) 118.

[Ban08a] Bansal A. K., W. Holzer, A. Penzkofer, E.B. Kley, "Spectroscopic and Lasing Characterization of Dicarbazovinylene-MEH-Benzene Dye as Thin Film and in Solution", accepted to be publish in Opt. Commun.

[Ban08b] Bansal A. K., A. Penzkofer, "Spectroscopic and Travelling-Wave Lasing Characterization of Tetraphenylbenzidine and di-Naphatalenyl-diphenylbenzidine" , accepted to be publish in Appl. Phys. B.

[Ban08c] Bansal A. K., A. Penzkofer, "Spectroscopic Characterization of Triphenyamine and Tris(3-Methylphenyl-Phenylamino)Benzene", submitted to Chem. Phys.

[Ban08d] Bansal A. K., W. Holzer, A. Penzkofer, H.-H. Horhold, E. Klemm, W. Frank, E. B. Kley, "Spectroscopic and Lasing Characterization of Luminescent Phenylene/Bipyridine Polymer", accepted to be publish in Synth. Metals.

[Bir63] Birks J. B., D. J. Dyson, Proc.R. Soc. London, Ser. A 275 (1963) 135.

[Bir70] Birks J.B., Photophysics of Aromatic Molecules, Wiley, London, p.51, 1970.

[Bla81] Blau W., A. Penzkofer, Opt. Commun. 36 (1981) 441.

[Bor80] Born M., E. Wolf, Principles of Optics, Electromagnetic Theory of Propagation, Intereference and Differection of Light, 6th edn., Pergamon, 1980.

[Bro78] Brosenberger P. M., W. Mey, A. Chowdry, J. Appl. Phys. 49 (1978) 273.

[Bur88] Burroughes J. H., C. A. Jones, and R. H. Friend, Nature 335 (1988) 137.

[Car98] Carroll J., J. Whiteway, D. Plumb, Distributed Feedback Semiconductor Lasers, SPIE Press Monograph Volume PM52 (The Institute of Electrical Engineers, London, 1998).

[Des90] Deshpande A.V., A. Beidoun, A. Penzkofer, G. Wagenblast, Chem. Phys. 142 (1990) 123.

[Dex53] Dexter D. L., J. Chem. Phys. 21 (1953) 836.

[Dör66] Dörr F., Angew. Chem. 78 (1966) 457.

[Dro98] Drotleff E., Diplomarbeit, Regensburg, 1998.

[Dua90] Duarte F.J. and L.W. Hillman (Eds.): Dye Laser Principles with Applications (Academic Press, Boston, 1990).

[Dua05] Duarte F.J., L.S. Liao, K.M. Vaeth, Opt. Lett. 30 (2005) 3072.

[Dua08] Duarte F. J., Appl. Phys. B 90 (2008) 101.

[Feo64] Feofilov P. P., The Physical Basis of Polarized Emission, Consultants Bureau, New York, 1964, p. 108.

[Fle86] Fleming G. R., Chemical Applications of Ultrafast Spectroscopy, Oxford University Press, New York, 1986.

[För51] Förster Th., Fluoreszenz organischer Verbindungen (Vandenhoeck und Ruprecht, Göttingen, Germany,1951).

[Fra01] Frank W., M. Wasgindt, T. Pautzsch, E. Klemm, Macromol. Chem. Phys. 202 (2001) 980.

[Fro97] Frolov S. V., M. Liess, P.A. Lane, W. Gellerman, Z. V. Vardeny, M. Ozaki, K. Yoshino, Phys. Rev. Lett. 78 (1997) 4285.

[Giu67] Giuliano, C.R. and L.D. Hess. IEEE J Quantum Electronics QE-3(8), (1967) 358.

[Gra85] Graf F., A. Penzkofer, Opt. Quantum Electron. 17 (1985) 53.

[Gra98] Granlund T., M. Theander, M. Berggren, M. Andersson, A. Ruseckas, V. Sundström, G. Björk, M. Granström, O. Inganäs, Chem. Phys. Lett. 288 (1998) 879.

[Gro99] Gross M., D. Müller, C. Bräuchle, K. Meerholz, Synth. Met. 102 (1999) 1147.

[Grö84] Grönninger G., A. Penzkofer, Opt. Quant. Electron. 16 (1984) 225.

[Hak04] Haken H. and H. C. Wolf, Molecular Physics and Elements of Quantum Chemistry (Springer, Berlin, 2004).

[Hal95] Halls J. J. M., C. A. Walsh, N. C. Greenham, E. A. Marseglia, R. H. Friend, S. C. Moratti, A. B. Holmes, Nature 376 (1995) 498.

[Hel62] Hellwege K. H., A. M. Hellwege (Editors), Landolt-Börnstein. Zahlenwerte und Funktionen aus Physik, Chemie, Astronomie, Geophysik und Technik. 6. Auflage. II. Band. Eigenschaften der Materie in ihren Aggregatzuständen. 8. Teil: Optische Konstanten. Springer Verlag, Berlin, 1962.

[Hel02] Heliotis G., D. D. C. Bradley, G. A. Turnbull, and I. D. W. Samuel, Appl. Phys. Lett. 81 (2002) 415.

[Her67] Hercher, M. Appl Opt. 6 (1967) 947.

[Hid97] Hide F., M.A. Díaz-García, B.J. Schwartz, and A.J. Heeger, Acc. Chem. Res. 30 (1997) 430.

[Hol97] Holzer W., A. Penzkofer, S.-H. Gong, A.P. Davey, and W.J. Blau, Opt. Quant. Electron. 29 (1997) 713.

[Hol99] Holzer W., M. Pichlmaier, A. Penzkofer, D. D. C. Bradley, W. J. Blau, Chem. Phys. 246 (1999) 445.

[Hol99a] Holzer W., M. Pichlmaier, E. Drotleff, A. Penzkofer, D.D.C. Bradley, W.J. Blau, Opt. Commun. 163 (1999) 24.

[Hol00] Holzer W., A. Penzkofer, H.-H. Hörhold, D. Raabe, and M. Helbig, Synth. Met. 113 (2000) 281.

[Hol00a] Holzer W., A. Penzkofer, R. Stockmann, H. Meysel, H. Liebegott and H. H. Hörhold, Synth. Metals. 125 (2000) 343.

[Hol00b] Holzer W., H. Gratz, T. Schmitt, A. Penzkofer, A. Costela, I. García-Moreno, R. Sastre, F. J. Duarte, Chem. Phys. 256 (2000) 125.

[Hol01] Holzer W., A. Penzkofer, T. Schmitt, A. Hartmann, C. Bader, H. Tillmann, D. Raabe, R. Stockmann, and H.-H. Hörhold, Opt. Quant. Electron. 33 (2001) 121.

[Hol01a] Holzer W., A. Penzkofer, R. Stockmann, H. Meysel, H. Liebegott, and H.-H. Hörhold, Synth. Metals 125 (2001) 343.

[Hol01b] Holzer W., A. Penzkofer, R. Stockmann, H. Meysel, H. Liebegott, and H.-H. Hörhold, Polymer 42 (2001) 3183.

[Hol01c] Holzer W., A. Penzkofer, H. Tillmann, E. Klemm, H.-H. Hörhold, Synth. Met. 124 (2001) 455.

[Hol02] Holzer W., A. Penzkofer, H. Tillmann, D. Raabe, H.-H. Hörhold, Opt. Mater. 19 (2002) 283.

[Hol02a] Holzer W., A. Penzkofer, T. Pertsch, N. Danz, A. Bräuer, E. B. Kley, H. Tillmann, C. Bader, H.-H. Hörhold, Appl. Phys. B 74 (2002) 333.

[Hol02b] Holzer W., A. Penzkofer, R. Stockmann, H. Meysel, H. Liebegott, H.-H. Hörhold, Synth. Met. 125 (2002) 343.

[Hol04] Holzer W., A. Penzkofer, A. Lux, H.-H. Hörhold, E. B. Kley, Synth. Met. 145 (2004) 119.

[Hol04a] Holzer W., A. Penzkofer, H. Tillmann, H.-H. Hörhold, Synth. Met. 140 (2004) 155.

[Hör01] Hörhold H.-H., H. Tillmann, C. Bader, R. Stockmann, J. Nowotny, E. Klemm, W. Holzer, A. Penzkofer, Synth. Met. 119 (2001) 199.

[Ish91] Ishikawa W., H. Inada, H. Nakano, Y. Shirota, Chem. Lett. (1991) 1731.

[Ish93] Ishikawa W., H. Inada, H. Nakano, Y. Shirota, et al., J. Phys. D : Appl. Phys. 26 (1993) B94.

[Jos98] Joshi M. P., J. Swiatkiewicz, F. Xu, P. N. Prasad, B. A. Reinhardt, R. Kannan, Opt. Lett. 23 (1998) 1742-1744.

[Kaf05] Kafafi Zakya (Ed.): Organic Electroluminescence (Taylor and Francis 2005).

[Kaw04] Kawamura Y., H. Yamaoto, K. Goushi, H. Sasabe, H. Yoshizaki, Appl. Phys. Lett. 84 (2004) 2724.

[Kep96] Kepler R.G., V.S. Valencia, S.J. Jacobs, J.J. McNamara, Synth. Met. 78 (1996) 227.

[Kog71] Kogelnik H. and C. V. Shank, Appl. Phys. Lett. 18 (1971) 152.

[Kog79] Kogelnik H., in: T. Tamir (Ed.), Integrated Optics, Topics in Applied Physics, Vol. 7, (Springer-Verlag, Berlin, 1979), pp. 13-81.

[Kol96] Kolb E. S., R. A. Gaudiana, P. G. Mehta, Macromolecules 29 (1996) 2359.

[Lak83] Lakowicz J.R., Principles of Fluorescence Spectroscopy, (Plenum, New York, 1983).

[Lem00] Lemmer U., A. Haugeneder, C. Kallinger, J. Feldmann, in: Semiconducting Polymers. Chemistry, Physics and Engineering, edited by G. Hadziioannou and P.F. van Hutten, Wiley-VCH, Weinheim, Germany, 2000, Chapter 10, p. 309-331.

[Liu00] Liu S., X. Jiang, H. Ma, M. S. Liu, A. K.-Y. Jen, Macromolecules 33 (2000) 3514.

[Mal05] Malliaras G. and R.H. Friend, Phys. Today 58 (2005) 53-58.

[McG00] McGehee, M. D.; Heeger, A. J. Adv Mater (Weinheim, Ger), 12 (2000) 1655.

[Mel61] Melhuish W. H., J. Phys. Chem. 65 (1961) 229.

[Miy95] Miyaura N., N. Suzuki, Chem. Rev. 95 (1995) 2457.

[Mor97] Morthier G., P. Vankwikelberge, Handbook of Distributed Feedback Laser Diodes (Artech House, Boston, 1997).

[Mos92] Moses D., Appl. Phys. Lett. 60 (1992) 3215.

[Nom04] Nomura M., Y. Shibasaki, M. Ueda, K. Tugita, M. Ichikawa, Y. Taniguchi, Macromolecules 37 (2004) 1204.

[Pen76] Penzkofer A., W. Falkenstein, W. Kaiser, Chem. Phys. Lett. 44 (1976) 82.

[Pen78] Penzkofer A., W. Falkenstein, Opt. Quantum Electron. 10 (1978) 399.

[Pen86] Penzkofer A. and Y. Lu, Chem. Phys. 103 (1986) 399.

[Pen87] Penzkofer, A. und W. Leupacher, J. Luminesc. 37 (1987) 61.

[Pen88] Penzkofer A., Appl. Phys. B 46 (1988) 43.

[Pen91] Penzkofer A., W. Bäumler, Opt. Quant. Electron. 23 (1991) 727.

[Pen92] Penzkofer A., W. Bäumler, in Lasers'91, edited by F. J. Duarte and D. G. Harris, STS Press, McLean, VA, 1992, p. 890.

[Pen98] Penzkofer A., E. Drotleff, W. Holzer, Opt. Commun. 158 (1998) 221.

[Pen01] Penzkofer A., W. Holzer, H.-H. Hörhold, H. Tillmann, D. Raabe, and M. Helbig, Proceedings of the International Conference on Lasers 2000 edited by V.J. Corcoran and T. A. Corcoran (STS Press, McLean, VA, 2001), pp. 523-529.

[Pen04] Penzkofer A., W. Holzer, H. Tillmann, H.-H. Hörhold, Opt. Commun. 229 (2004) 279.

[Pet71] Peterson O.G., J.P. Webb, W.C. McColgin, J.H. Eberly, J. Appl. Phys. 142 (1971) 1917.

[Phi03] Philip R., W. Holzer, A. Penzkofer, H. Tillmann, H.-H. Hörhold, Synth. Met., 132 (2003) 297.

[Pop99] Pope M., C. E. Swenberg, Electronic Processes in Organic Crystals, Oxford University Press, New York, 1999.

[Sal02] Salbeck J., M. Schörner, T. Fuhrmann, Thin Solid Films 417 (2002) 20.

[Sam07] Samuel I.D.W. and G.A. Turnbull, Chem. Rev. 107 (2007) 1272.

[Sar06] Saragi T.P.I., T. Fuhrmann-Lieker, J. Salbeck, Adv. Funct. Mater. 16 (2006) 966.

[Sat00] Sato Y., S. Ichinosawa, T. Fugono, Y. Murata, Synth. Met. 111-112 (2000) 25.

[Sha71] Shank C. V., J. E. Bjorkholm, and H. Kogelnik, Appl. Phys. Lett. 18 (1971) 395.

[Shi04] Shinar J. (Editor), Light emitting diodes. A Survey, Sprringer-Verlag, New York, 2004.

[Shi05] Shirota Y., J. Mater. Chem. 15 (2005) 75.

[Shi07] Shirdel J., A. Penzkofer, R. Procházka, Z. Shen, J. Daub, Chem. Phys. 336 (2007) 1.

[Sil01] Silva C., M. A. Stevens, D. M. Russell, S. Setayesh, K. Müllen, R. H. Friend, Synth. Met. 116 (2001) 9.

[Str62] Strickler S.J., R.A. Berg, J. Chem. Phys. 37 (1962) 814.

[Tan87] Tang C.W., S.A. VanSlyke, Appl. Phys. Lett. 51 (1987) 913.

[Tan89] Tang C. W., S. A. Van Slyke, C. H. Chen, J. Appl. Phys. 85 (1989) 3610.

[Tes96] Tessler N., G. J. Denton, and R. H. Friend, Nature 382 (1996) 695.

[Tes99] Tessler, N. Adv. Mater. (Weinheim, Ger) 11 (1999) 363.

[The66] Thermal Quarz-Schmelze. Datenblatt, Optical Products, 65201 Wiesbaden, Deutschland, 1996.

[The02] Thelakkat M., Mocromol. Mater. Eng. 287 (2002) 442.

[Tut93] Tutt L. W., T. F. Boggess, Prog. Quant. Electron. 17, 299-338 (1993).

[Wei93] Weidner P., A. Penzkofer, Opt. Quant. Electron. 25 (1993) 1.

[Val02] Valeur B., Molecular Fluorescence. Principles and Applications. (Wiley-VCH, Weinheim, 2002).

[Van96] Van Slyke S. A., C. H. Chen, C. W. Tang, Appl. Phys. Lett. 69 (1996) 2160.

[Yan95] Yan M., L. J. Rothberg, E. W. Kwock, and T. M. Miller, Phys. Rev. Lett. 75 (1995) 1992.

[Yu98] Yu G., J. Wang, J. McElvain, and A. J. Heeger, Adv. Mater. 10 (1998) 1431.

[Zav01] Zavelani-Rossi M., G. Lanzani, S. de Silvestri, M. Anni, G. Gigli, R. Cingolati, G. Barbarella, L. Favaretto, Appl. Phys. Lett. 79 (2001) 4082.

Acknowledgements

First of all I thank to God then I would like to express my extreme gratitude towards Prof. Dr. Alfons Penzkofer for creating the opportunity for me to pursue PhD in his research group in University of Regensburg. He is a very encouraging, motivating, understanding and invaluable supervisor. His zeal for excellence and perfection is highly admirable and has helped me to bring my research to this level of completion. I will be heartily obliged to him in my whole life.

I am heartily thankful to Dr. Wolfgang Holzer for his kindness, support, fruitful advices and some of the measurements which he has done in this work.

I would also like to acknowledge Prof. Dr. E. Klemm, Prof. Dr. H.-H. Hörhold and Dr. W. Frank, for synthesizing and providing polymer and Dr. E. B. Kley for providing the gratings, which have been used in this work.

I am especially thankful to the secretaries of our group, Mrs. Sigrid König and Mrs. Elisabeth Schaffer for their kindness and help in spite of their busy schedule.

I am thankful to Mrs. Anja Merkel for her excellent technical assistance in my experimental setups. I am grateful to Mr. Riedl and his colleagues in the electronic workshop who were always willing to help.

I am thankful to Prof. Tsuboi for his collaboration with our group. My special thanks for his kindness, support and helpful advices during his stay in Regensburg.

I am heartily thankful to Prof. Dr. J. Repp for his fruitful suggestions during my seminars.

I am also thankful to my colleagues and friends, Dr. Javid Shirdel, Dr. Peyman Zirak, Martin and Tony for their help, support and encouragement. Special thanks to Amit Tyagi, for his friendship and encouragement during my studies and for pointing out errors in my thesis. Also,

my former colleagues Dr. Thomas Susdorf, Dr. Sang-Hun Song and David DelAgua are gratefully acknowledged.

I am also thankful to Graduate College, GK640/2, "Sensory photo-receptors in natural and artificial systems" for providing fruitful seminars and summer school in Konstanz.

I also express my extreme gratitude to Prof. Arun Kumar, Dr. N. S. Mehla, and Prof. Vijendra Agarwal, for their meaningful guidance and encouragement throughout my academic carrier.

Special thanks to my friend Kumaran for his help during my stay in Regensburg and also for carefully reading this manuscript and providing useful suggestions concerning language and style.

I owe my thanks to all of my friends Patil, Prantik, Srinivas, Tapan, Chinna, Pavan and Shrikant for making mine life much easier during my stay in Regensburg and in facing the difficult situations.

This work would not have been possible without the ever present support and encouragement from my wife, Shikha Singhal. She has been extremely patient, understanding, and loving throughout my numerous research and thesis writing times.

Last and certainly not the least, I owe my special gratitude to my parents and in-laws, whose love and blessing are always with me. My heartily thanks to my elder brothers and my brother-in-laws, without their moral support my stay in Germany was not possible. My special thanks to my loving sister. Finally, I would like to dedicate this thesis to my mother.